University of Crete
Physics Department
Heraklion, Crete

TEMPERATURE MEASUREMENTS IN MATERIALS WITH DIFFERENT CONDUCTIVITIES UTILIZING MILD MICROWAVE HYPERTHERMIA TECHNIQUES: CORRELATION OF RESULTS WITH QUANTITATIVE MRI METHODOLOGIES

Gkasios D. Vasileios
ph4686@edu.physics.uoc.gr

February, 2022

Supervisors

Maris G. Thomas, from Medical Physics Department
Professor, School of Medicine, University of Crete

Kominis Iannis, from Physics Department
Associate Professor, Physics Department, University of Crete

Examination Committee

Maris G. Thomas,
Professor, School of Medicine, University of Crete

Kominis Iannis,
Associate Professor, Physics Department, University of Crete

Makris Konstantinos,
Assistant Professor, Physics Department, University of Crete

Abstract

Hyperthermia is a cancer treatment method that has been used for thousands of years. Hyperthermia is defined as the delivery of a desired and controlled form of heat to a disease site while protecting the surrounding healthy tissue from irreversible damage.

As cancer treatment, hyperthermia has sparked a lot of attention. In hyperthermia treatments, tumors are selectively heated to temperatures exceeding $40°C$*, while healthy tissues are maintained below critical temperatures. Hyperthermia is a non-invasive therapeutic option that has been shown to be quite effective in clinical treatment. However, the issue of temperature monitoring stifles its growth.*

Magnetic resonance imaging is one of the methods under investigation for noninvasive thermometry (MRI). Thermometric image parameters based upon magnetic resonance relaxation times, are taken into account. Relaxation times are temperature dependent. In comparison to invasive procedures, MRI-based temperature mapping techniques are safe and have been used to detect temperature changes in a number of applications.

Magnetic resonance imaging (MRI) is a versatile and powerful medical imaging technique that has been widely used in clinical practice. A major advantage of MRI over other imaging modalities, aside from its nonionizing radiation nature, is that it may produce superior and versatile soft tissue contrasts based on the intrinsic features of tissues. Three common contrast methods utilized in clinical applications are proton density–weighted contrast, $T1-$*weighted contrast, and* $T2-$*weighted contrast.*

During the experimental process we created hyperthermia states in four samples using microwave diathermy antenna. With the use of an MRI system we visualized and correlated the effects of hyperthermia.

The purpose of this work was twofold. The initial goal was to measure and quantify the $T2$ *parameter as a function of temperature in mild hyperthermia, in order to control the* $T2$ *index as a way of measuring temperature changes during the hyperthermia process. The* $T2$ *parameter was measured for four different samples. The first three had electrical properties -and more specifically electrical conductivity (EC)- that resembled various tissues at* $37°C$*. The first solution had conductivity which was resembling fat, the second had grey matter and the third a cerebrospinal fluid. The fourth solution was a colony of human melanoma cancer cells.*

Secondarily, conductivities of the four solutions were measured in a temperature range of $20°C$ *to* $45°C$ *after the process of heating, in order to quantify conductivity* C *versus temperature* T *as well as the conductivity dependence of different heating processes, such as microwave diathermy and heating induction.*

Περίληψη

Η Υπερθερμία αποτελεί μια μέθοδο για τη θεραπεία του καρκίνου η χρήση της οποίας έχει αναφερθεί εδώ και χιλιάδες χρόνια. Κλινικά η υπερθερμία ορίζεται ως η ανύψωση της θερμοκρασίας τοπικά σε εύρος $42°C$ ως $45°C$, σε μια περιοχή της νόσου ενώ ταυτόχρονα οι υγιείς ιστοί διατηρούνται κάτω από τις κρίσιμες θερμοκρασίες. Ετσι ο περιβάλλοντα υγιή ιστός προστατευεται από μη αναστρέψιμες βλάβες.

Η υπερθερμία έχει προκαλέσει μεγάλη προσοχή ,καθώς είναι μια μη επεμβατική θεραπευτική τεχνική που έχει αποδειχθεί αρκετά αποτελεσματική στην κλινική θεραπεία. Ωστόσο, το θέμα της παρακολούθησης της θερμοκρασίας καταστέλει την ανάπτυξή του.

Η μαγνητική τομογραφία είναι μία από τις υπό διερεύνηση μεθόδους για τη μη επεμβατική θερμομέτρηση (MRI). Οι χρόνοι μαγνητικής αποκατάστασης εξαρτώνται από την θερμοκρασία και μπορούν να ληφθούν υποψήν για τις θερμομετρικές παραμέτρους της εικόνας.

Σε σύγκριση με τις επεμβατικές διαδικασίες, οι τεχνικές χαρτογράφησης θερμοκρασίας που βασίζονται σε μαγνητική τομογραφία είναι ασφαλείς και έχουν χρησιμοποιηθεί για την ανίχνευση μεταβολών θερμοκρασίας σε πολλές εφαρμογές.

Η μαγνητική τομογραφία (MRI) είναι μια ευέλικτη και ισχυρή τεχνική ιατρικής απεικόνισης που χρησιμοποιηείτε ευρέως στην κλινική πράξη. Ένα σημαντικό πλεονέκτημα της μαγνητικής τομογραφίας σε σχέση με άλλες μεθόδους απεικόνισης, εκτός από το ότι χρησιμοποιεί μη ιονίζουσα ακτινοβολία, είναι ότι μπορεί να παράγει εικόνες υψηλής αντιθέσης μαλακών ιστών με βάση τα εγγενή χαρακτηριστικά των ιστών. Τρεις συνήθεις μέθοδοι σκιαγραφικής αντίθεσης που χρησιμοποιούνται σε κλινικές εφαρμογές είναι η αντίθεση με έμφαση στην πυκνότητα πρωτονίων, η αντίθεση με έμφαση στην παράμετρο $T1$ και η αντίθεση με έμφαση στην παράμετρο $T2$.

Κατά τη διάρκεια της πειραματικής διαδικασίας, κάνοντας χρήση κεραίας διαθερμίας μικροκυμάτων, δημιουργήσαμε καταστάσεις υπερθερμίας σε τέσσερα δείγματα, εκ των οποίων τα τρία (3) από αυτά ήταν διαλύματα Χλωριούχου Νατρίου ($NaCl$) που προσομοίαζαν ιστούς, ενώ το τελευταίο αποτελούσε καλλιέργεια καρκινικών κυττάρων μελανώματος. Με τη χρήση ενός συστήματος MRI απεικονίσαμε και συσχετίσαμε τα αποτελέσματα της υπερθερμίας που προκλήθηκαν.

Ο σκοπός αυτής της εργασίας ήταν διττός. Αρχικός στόχος ήταν η μέτρηση και ποσοτικοποίηση της παραμέτρου $T2$ συναρτήσει της θερμοκρασίας σε καταστάσεις ήπιας υπερθερμίας, με σκοπό τον έλεγχο του δείκτη $T2$ σαν μέσο μέτρησης μεταβολών της θερμοκρασίας, κατά τη διάρκεια μίας διαδικασίας υπερθερμίας. Η μέτρηση του δείκτη $T2$ πραγματοποιήθηκε για τέσσερα διαφορετικά δείγματα εκ των οποίων τα πρώτα τρία είχαν ηλεκτρικές ιδιότητες -και πιο συγκεκριμένα αγωγιμότητα- που προσομοίαζαν διάφορους ιστούς σε θερμοκρασία $37°C$. Το πρώτο διάλυμα είχε αγωγιμότητα η οποία προσομοίαζε το λίπος, το δεύτερο προσομοίαζε φαιά ουσία εγκεφάλου και το τρίτο εγκεφαλονωτιαίο υγρό. Το τέταρτο διάλυμα αποτελούσε καλλιέργεια καρκινικών κυττάρων μελανώματος.

Σε δεύτερο χρόνο, μετρήθηκε η αγωγιμότητα των τεσσάρων διαλυμάτων σε εύρος θερμοκρασιών από 20 έως 40 βαθμούς Κελσίου, με σκοπό την ποσοτικοποίηση της αγωγημότητας C συναρτήσει της θερμοκρασίας T καθώς και τη μελέτη συμπεριφοράς της αγωγιμότητας χρησιμοποιώντας διαφορετικές τεχνικές θέρμανσης (επαφή και διαθερμία μικροκυμάτων).

Acknowledgements

Throughout the writing of this dissertation I have received a great deal of support and assistance.

I would first like to thank my supervisors, Professor Thomas G. Maris and Associate Professor Kominis Iannis, whose expertise was invaluable in formulating the research questions and methodology. Your insightful feedback pushed me to sharpen my thinking and brought my work to a higher level. Thank you for your patience as well as the knowledge you shared with me throughout this project.

I would like to acknowledge my colleagues from my participation at Medical Physics Laboratory for their wonderful collaboration.

Furthermore, I would like to thank Spiros Karkavitsas for his assistance in enabling me to swiftly adapt in the laboratory. Spyros, your support was important to the success of this project.

I would also like to thank the members of my examination committee not only for their acceptance but also for their for their time and patience.

In addition, I would like to express my deepest gratitude to my family for their wise counsel and sympathetic ear. You are always there for me, and I appreciate it.

Finally, I could not have completed this dissertation without the support of my friends, who provided stimulating discussions as well as happy distractions to rest my mind outside of my work.

Abbreviations

C_{ref}	Reference Conductivity
c	Content
CsF	Cerobrospinal Fluid
DNA	Deoxyribonucleic Acid
EC	Electrical Conductivity
EFTE	Ethylene Tetrafluoroethylene
EM	Electromagnetic
ETL	Echo Train Length
F	Fat
F_c	Characteristic Frequency
FID	Free Induction Decay
FOV	Field Of View
FSE	Fast Spin Echo
GM	Grey Matter
GRE	Gradient Recalled Echo
HASTE	Half-Fourier Acquisition Single-shot Turbo spin Echo
IEEE	Institute of Electrical and Electronic Engineers
ISM	Industrial Scientific and Medical
MR	Magnetic Resonance
MRI	Magnetic Resonance Imaging
MTT	Microwave Theory Techniques
MW	Microwaves
NMR	Nuclear Magnetic Resonance
NMV	Net Magnetization Vector
OD	Outer Diameter
RF	Radiofrequency
SE	Spin Echo
SNR	Signal to Noise Ratio
SI	International System of Units
TC	Temperature Compensation
TE	Echo Time
TR	Repetition Time
TSE	Turbo Spin Echo
T1w	T1 Weighted
T2w	T2 Weighted
UV	Ultraviolet

Contents

List of Figures

1. Introduction to MRI

1.1 History of MRI

Nuclear magnetic resonance (NMR) images have been used since 1973, and the physics of magnetic resonance imaging (MRI) were originally defined in 1946. Felix Bloch[1] at Stanford University and Edward Purcell[2] at Harvard University separately described the NMR phenomena in 1946. In 1952, both were awarded the Nobel Prize in Physics for their achievements. Felix Bloch postulated that atomic nuclei have qualities that allow them to function like small magnets, laying the groundwork for MRI[3]. In 1946, he published his theory proposing that a charged particle rotating around its axis would have a magnetic field or magnetic dipole moment[1]. This idea was confirmed experimentally, and nuclear magnetic resonance spectrometers were introduced in the 1960s; nonetheless, magnetic resonance was not used clinically until the late 1970s. In 1974, Raymond Damadian claimed that malignant tissue's magnetic resonance characteristics varied from those of normal tissue[4], and it took almost 4 hours to scan. Around this time, the phrase "nuclear" was deleted to avoid scaring people away from this new type of imaging. With the use of breath-holding techniques, or "navigators", MRI went from imaging static objects to imaging moving things, including the heart, over time. This allowed for high-resolution anatomical heart imaging, which was followed by functional imaging and myocardial tissue characterization.

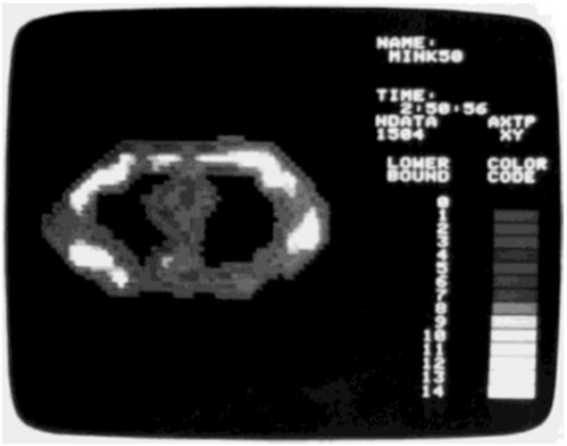

Figure 1.1.1: The first MRI image of the human body, obtained in 1977.[5]

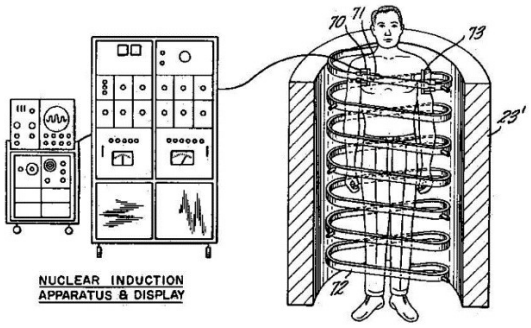

Figure 1.1.2: "Apparatus and method for detecting cancer in tissue" by Raymond Damadian. US patent 3789832 was issued on February 5, 1974, after being filed on March 17, 1972.[6]

1.2 Spin and the Nuclear Magnetic Resonance Phenomenon

Clinical MRI is a type of imaging that relies on the presence and properties of water (and, to a lesser extent, fat), which comprises up 70% to 90% of most tissues. During disease and injury, the characteristics and amount of water in tissue can change substantially, making MR an extremely sensitive diagnostic method. MR detects subtle changes in the nucleus' magnetism. This penetrates further than $X-$rays, which interact with the electron clouds or shells that orbit the nucleus. MR is an extremely effective modality. At its most advanced, MR can be used not only to view anatomy and pathology, but also to explore organ function, probe in vivo chemistry, and even visualize brain thought.[6]

The water molecule is comprised of two hydrogen atoms which will eventually produce the MRI signal. The hydrogen atom (Fig.1.2.1) is comprised of two parts: a negatively charged electron and a nucleus with a single positively charged proton.[7],[8]

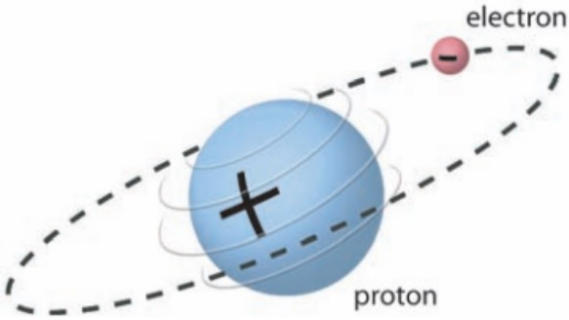

Figure 1.2.1: The hydrogen atom consists of an electron and the nucleus, which contains one proton.[7]

The MRI signal is created by this nucleus, hence the term "nuclear" is used in NMR. Given the fact that the proton has a positive charge and the electron has a negative charge, the hydrogen atom as a whole is electrically neutral. It's the proton that is important in this case. Aside from its positive charge, the proton has spin, which is a feature shared by nearly all basic particles. This indicates that the proton, like a spinning top, rotates around its axis. A proton with these characteristics has two significant qualities: The proton, as a rotating mass, possesses angular momentum and behaves like a spinning top that attempts to maintain the spatial orientation of its rotation axis. As a revolving mass with an electrical charge, the proton also has a magnetic moment, B, and behaves like a tiny magnet.[8],[9],[10]

In its most simple form, the nucleus/proton can be conceived as a tiny magnet (with a north and south pole like any magnet) that spins along its axis (Fig.1.2.2).[7]

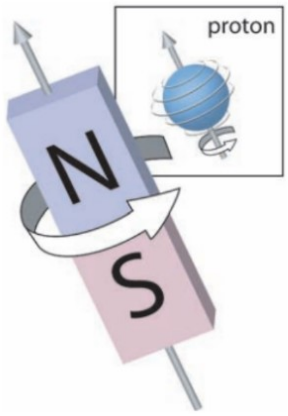

Figure 1.2.2: The proton behaves like a spinning magnet with a north and a south pole; hence is referred to as a spin.[7]

These tiny tissue magnets, known as spins, are ordinarily oriented randomly (Fig.1.2.3.a), but when brought close to a powerful magnet (i.e., within a strong external magnetic field), they align along with it (parallel) or in the opposite direction (anti-parallel) (Fig.1.2.3.b). The parallel orientation is marginally preferred over the anti-parallel orientation, resulting in a minor excess of spins along the parallel direction (approximately 1 in 1 million).[7]

These excess spins are the only ones that will eventually generate a signal (Fig.1.2.3.c) that can be converted into images. This makes MRI a relatively insensitive approach, and it is fortunate that there is plenty of water in the body to compensate for this cancellation between spins. By increasing the intensity of the external magnet, the little excess number of spins that produce signal can be increased.[7]

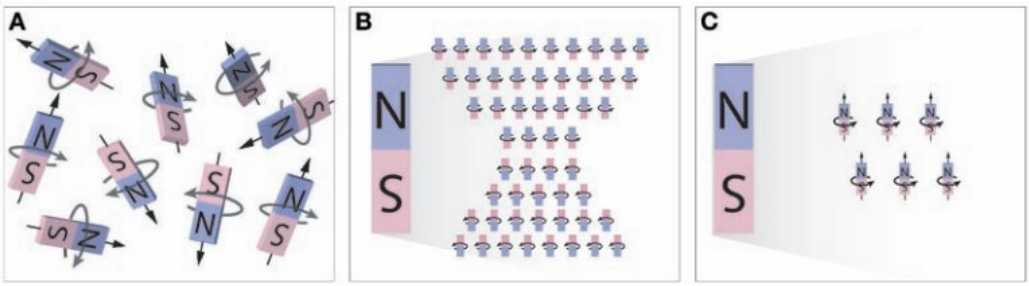

Figure 1.2.3: (a) In the absence of an external magnetic field, spins are oriented in random.[7] (b) When an external magnetic field B_0 is applied, the spins align parallel or anti-parallel to it.[7] (c) The spins that will produce measurable magnetic resonance signals are represented by the difference between parallel and antiparallel spins.[7]

In the following figures, each magnet is represented by a vector. Each magnet's north pole will correspond to the arrowhead, while the south pole will correspond to the arrow tail. Each vector's length will correspond to the strength of each magnet. As a result, Fig.1.2.3 can be redrawn as Fig.1.2.4. To distinguish these magnets, each spin is assigned with the letter μ, and $\vec{B_0}$ is used to describe the external magnetic field. The magnetic field strength of a typical clinical scanner is $B_0 = 1.5T$. In comparison, the magnetic field of the Earth is $0.00005T$.[7]

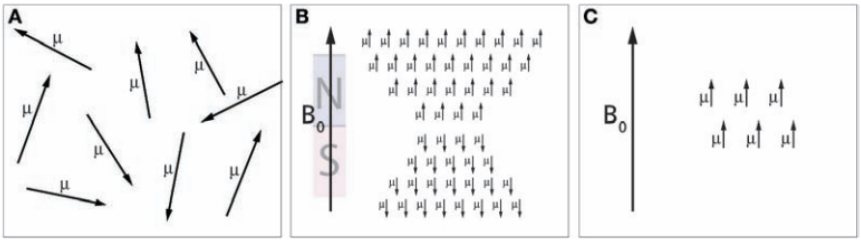

Figure 1.2.4: (a) Spins, represented by μ vectors, are randomly orientated in the absence of an external magnetic field.[7] (b) The external magnetic field is represented by a long vector B_0. The spins (represented by the short vectors μ) align parallel or anti-parallel to B_0.[7] (c) The difference between the parallel minus the anti-parallel vectors/spins will create a detectable magnetic resonance signal.[7]

When an external force (typically the earth's gravitational field G) acts on a spinning top and attempts to change the orientation of its rotational axis, the top wobbles, a process known as precession. Simultaneously, friction at the point of contact drains energy from the spinning top and slows its rotation. As a result, the axis becomes increasingly inclined, and the top eventually collapses.[8],[9],[10]

Returning back to hydrogen nuclei, when exposed to an external magnetic field, B_0, the magnetic moments, or spins, align with the field's direction like compass needles.[8]

Magnetic moments not only align with the field, but also precess like spinning tops. The nuclei precess at a characteristic speed proportional to the strength of the applied magnetic field, which is known as the Larmor frequency. The alignment of spins parallel to the magnetic field is a gradual process that, like spinning tops, is associated with energy dissipation. The Larmor frequency is a fundamental concept in MRI.[8]

In a further depth: The Larmor or precession frequency, ω_0, is the rate at which spins wobble when placed in a magnetic field. This frequency is proportional to the magnetic field strength, B_0, as shown by the Larmor Equation (Eq.1.2.1)[8],[11]:

$$\omega_0 = B_0 \cdot \gamma_0 \tag{1.2.1}$$

where

ω_0: is the Larmor frequency in Megahertz (MHz)
B_0: the strength of the magnetic field in Tesla (T)
γ_0: the gyromagnetic ratio, a constant specific to a particular nucleus

The gyromagnetic ratio of protons is $42.58 MHz/T$, resulting in a Larmor frequency of $63.9 MHz$ at $1.5T$, compared to only about 1kHz in the earth's magnetic field (FM radio transmitters operate at $88 MHz - 108 MHz$).

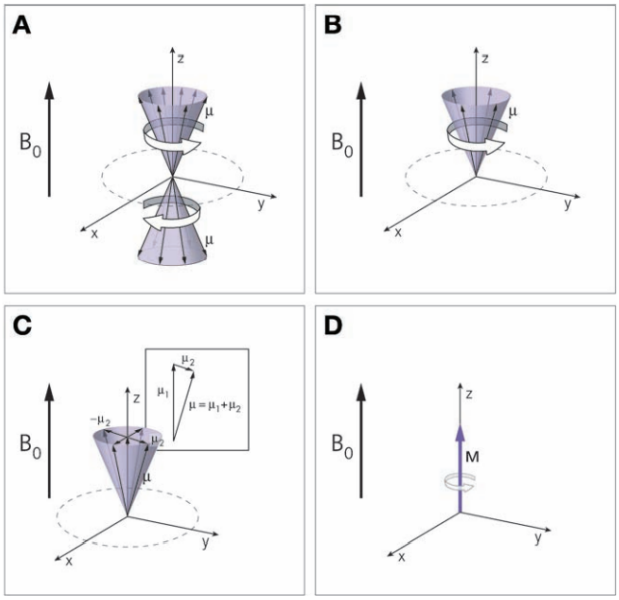

Figure 1.2.5: (a) The spins actually precess on the surface of a parallel and an anti-parallel cone.[7] (b) The excess spins precess on the surface of the parallel cone.[7] (c) Each spin μ has components along the $z-$axis on the base of the cone. The components lying on the base of the cone add up to zero.[7] (d) The components along the $z-$axis add constructively to form the main magnetization vector M.[7]

Because all the components at the base cancel out, only the components along the $z-$axis remain. These add constructively to generate the net magnetization vector M. (Fig.1.2.5.d). Rather than dealing with individual spins, the net magnetization vector M will be used.[7]

While the spin system relaxes and settles into a stable state, longitudinal magnetization M_z accumulates in the $z-$direction due to the addition of the magnetic vectors representing the individual magnetic moments. This occurs in the earth's magnetic field as well, but the resulting longitudinal magnetization is mild. An MR imager's magnetic field B_0 is $60,000$ times stronger, and the resulting longitudinal magnetization is accordingly greater. Because the MR signal is so weak, magnetization must be high enough to produce a signal.[8],[9],[10]

Spins tend to align parallel or anti-parallel to the magnetic field, with parallel alignment mildly preferred since it corresponds to spins in a more favorable energy state. As a result, a slightly larger fraction aligns parallel to the primary magnetic field under steady-state conditions. This little difference provides the quantifiable net magnetization M_z, which is represented by the net magnetization vector (NMV). Because the energy

difference between the two orientations is proportional to the strength of the external magnetic field, M_z increases with field strength.[8],[9],[10]

1.3 The Magnetic Resonance Signal

The magnetic resonance (MR) signal is generated by reducing the net magnetization vector M onto the transverse $xy-$plane, away from the $z-$axis. This is accomplished by using a secondary magnetic field B_1. This magnetic field B_1 is applied for a short amount of time, (approximately $1ms - 5ms$), which is why it is referred to as a pulse. B_1 is part of a radio frequency pulse (RF). The magnetic field B_1 differs from the main magnetic field B_0 as it is not static, but rotates with a frequency ω_1 perpendicular to the main magnetic field B_0. As a result, B_1 is rotating onto the laboratory frame of reference's $xy-$plane. In other words, B_1 needs to be in phase with the spins that precess at the Larmor frequency.[7]

$$\omega_1 = \omega_2 \tag{1.3.1}$$

The net magnetization M must precess around the newly introduced rotating magnetic field B_1 while continuing to precess around the static magnetic field B_0 at the same time. The outcome of two distinct precessions of M about the two magnetic fields is difficult to observe in this beehive trajectory. The revolving frame of reference is used to better visualize this motion. Things are viewed in this new frame of reference as though one is seated on the B_1 vector and rotating with it. As a result, B_1 seems to be stationary in the revolving frame of reference, and it is aligned with the $x-$axis. It's important to note that nothing actually changes; it's just the viewpoint on things that shifts. In the rotating frame of reference, any precession of M about B_0, which occurs at the same rotational speed since it is on-resonance, is similarly undetectable, because ω_0 is zero, it appears that B_0 is no longer present (see Eq.1.2.1). This is why B_0 is not included when the rotating frame of reference is sketched.

The only motion visible to in the rotating frame of reference is the precession about B_1. The first component of this precession is a rotation on the $zy-$plane, because the net magnetization M must precess around B_1 and M is perpendicular to B_1. The signal that B_1 generates can be detected if B_1 is removed when M crosses the transverse plane, that is, when M is on the $y-$axis. B_1 has caused M to rotate from the $z-$axis to the $y-$axis, resulting in a 90° rotation, thus, B_1 is known as a 90° RF pulse. The detection of signals is simpler to discern in the laboratory frame of reference where M precesses.

Considering that M is a revolving magnet, according to Faraday's Law, it can induce a voltage onto a loop of wire due to its rotation. The MR signal is this voltage, which we can be easily recorded. The signal that is captured at the loop of wire (i.e., antenna) has a sinusoidal waveform, as shown in Fig. 1.3.1, due to M's rotation at the Larmor frequency. This signal is known as the free-induction decay (FID); for the time being, the fact that it is fading with time, i.e., its magnitude (also known as amplitude) is diminishing with time will be disregarded.

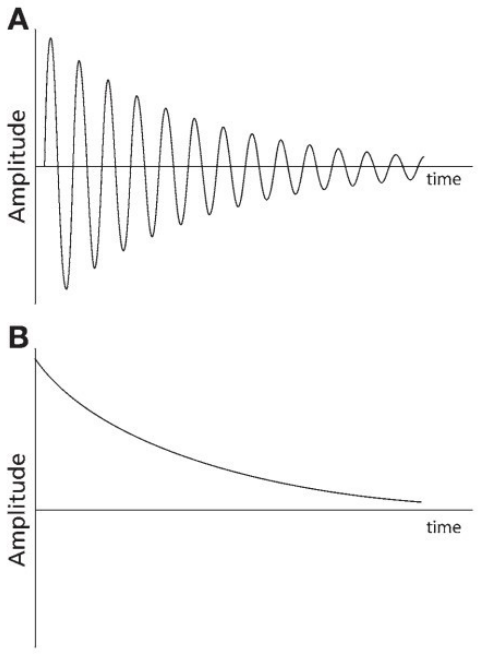

Figure 1.3.1: (a) The signal recorded within the laboratory frame of reference is the oscillating free induction decay.[7] (b) The signal recorded within the rotating frame of reference is the non-oscillating free induction decay.[7]

The signal in Fig.1.3.1.a is shown in the laboratory frame of reference (i.e., the antenna). The waveform would be as shown in Fig.1.3.1.b if the signal was observed in the rotating frame of reference, which is the equivalent of listening to radio station music through a radio's speaker rather than trying to listen to it by placing an antenna directly to one's ear. However, a radio receiver is required to observe in the rotating frame of reference. A radio receiver like this is included into the MRI scanner. Rather than being sent to a speaker, the signal is recorded in digital form in the computer's memory.

The one-pulse experiment is the series of events that results in a FID, and it is illustrated in a pulse sequence diagram (Fig.1.3.2). This is the simplest experiment, which entails simply turning on the 90° RF pulse for a short length of time, then shutting it off, followed by turning on the receiver to acquire the MR signal, then shutting it off.

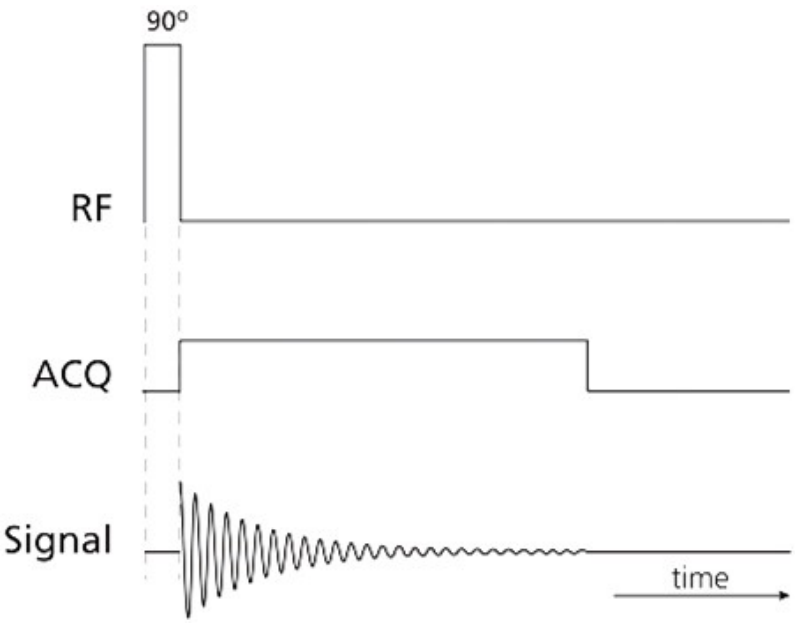

Figure 1.3.2: The one pulse experiment pulse sequence diagram.[7]

1.4 Relaxation and Relaxation Times

In terms of energy transfer, the MR measurement can be examined. The process by which protons release the energy absorbed from the RF pulse is known as relaxation. Relaxation is as important as energy absorption in magnetic resonance imaging, and it is the principal mechanism for image contrast. RF energy is absorbed by protons only when it is transmitted at the correct frequency in resonance absorption. The excess energy causes the equilibrium arrangement of spins parallel and anti-parallel to B to be disrupted. Following excitation, relaxation occurs and the protons release the extra energy and return to their original configuration via naturally occurring processes. Despite the fact that each proton absorbs energy, relaxation periods are assessed for a full sample and are statistical or average observations. $T1$ and $T2$ are the relaxation times that can be measured. Both times measure stimulated energy transfer by an excited proton, but the final disposition of the energy differs.[6],[12],[13],[14],[15]

1.4.1 $T1$ Relaxation

Following an excitation pulse, the relaxation time $T1$ is the time required for the $z-$component of M to return to 63% of its original value. The spin-lattice relaxation time, or longitudinal relaxation time, is another name for it. During equilibrium, M_0 is parallel to B_0, and that energy absorption causes M_0 to spin towards the transverse plane. $T1$ relaxation is the mechanism through which protons give up energy in order to revert to their original orientation. If a 90° pulse is administered to a sample, M_0 will spin and no longitudinal magnetization will be present after the pulse. As the protons lose their energy, a recovery of longitudinal magnetization will be detected over time (Fig.1.4.1).

This magnetization return follows an exponential growth process, with $T1$ characterizing the rate of growth:

$$M_z(t) = M_z(t = 0) \cdot (1 - e^{-t/T1}) \tag{1.4.1}$$

where
t: is the time following the RF pulse.

M will have restored to 95% of its pre-excitation pulse value, M_0, after three $T1$ time periods. The phrase spin-lattice refers to the fact that when a proton ("spin") is stimulated, its energy is transferred to its surroundings ("lattice") rather than to another spin. Spin excitation is no longer aided by the energy.[7],[16]

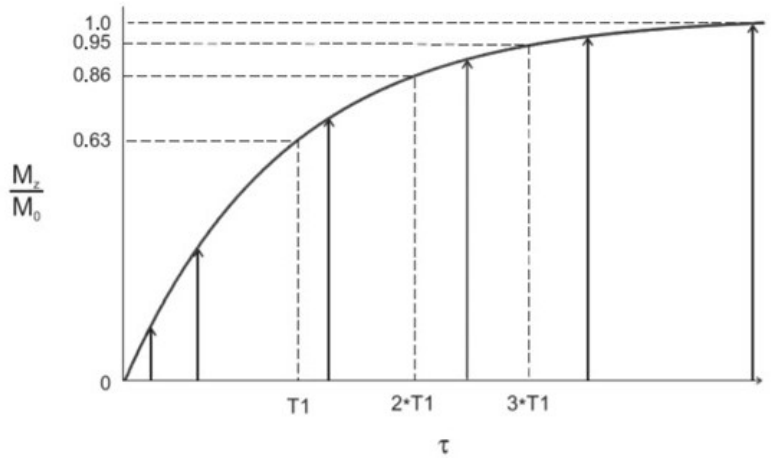

Figure 1.4.1: $T1$ relaxation curve. Following a 90° RF pulse, there is no longitudinal magnetization. A short time later, longitudinal magnetization will be observed as the protons release their energy through $T1$ relaxation. Gradually, as more protons release their energy, a larger fraction of M_z is reestablished. Eventually, M_0 will be restored completely. The change of M_z/M_0 with time t follows an exponential growth process, as described by Eq.1.4.1. The time constant for the process is $T1$, the spin-lattice relaxation time, and is the time when M_z has returned to 63% of its original value.[12]

1.4.2 $T2$ Relaxation and $T2^*$ Relaxation

$T2$ is the time required for the transverse component of M to decay to 37% of its initial value through irreversible processes. The spin-spin relaxation period, or transverse relaxation time, is another name for it.[8],[10] At equilibrium, M_0 is oriented only along the $z-$ (B_0) axis, with no component of M_0 in the xy plane. The coherence is totally longitudinal. The absorption of energy from a 90° RF pulse causes M_0 to spin completely into the xy plane, resulting in coherence in the transverse plane at the end of the pulse. this coherence fades with time, while the protons release their energy and re-position themselves along B_0. The FID is caused by the disappearance of coherence. As this coherence decreases, the value of M in the xy plane approaches zero. The process by which this transverse magnetization is lost is known as $T2$ or $T2^*$ relaxation. As the spins exchange energy and decrease

the amount of the transverse magnetization and the produced signal, this fluctuation causes a gradual, irreversible loss of phase coherence (Fig.1.4.2). $T2$ is the time when the transverse magnetization is 37% of its value immediately after the 90° pulse, and this irreversible process is the only cause of coherence loss. This transverse coherence elapses with time, only to reappear in the longitudinal direction as $T1$ relaxes. $T2$ dephasing time is always less than or equal to $T1$ dephasing time.

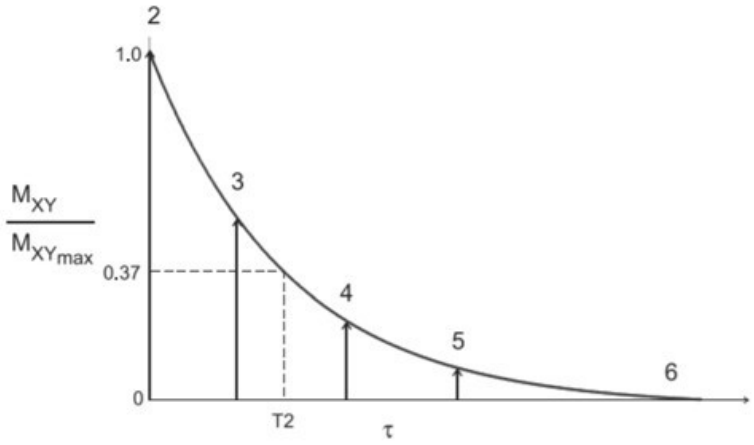

Figure 1.4.2: Plot of the relative M_{xy} component as a function of time. The change in $M_{xy}/M_{xy_{max}}$ with time t follows an exponential decay process, as described by Eq.1.4.2. The time constant for the process is T2, the spin-spin relaxation time, and is the time when M_{xy} has decayed to 37% of its original value.[12]

The occurrence of the human body induces local inhomogeneity. MRI scanners typically feature hardware that can be used to attempt to resolve these local inhomogeneities to some extent using a technique known as field shimming. This relaxation process that depends on spin-spin interactions, as well as additional B_0 field inhomogeneities, happens with the time constant $T2^*$ ($T2$-star).[7],[8] $T2^*$ relaxation is the term used to characterize the effects of $T2$ relaxation combined with the de-phasing caused by inhomogeneity in B_0. When detecting a free induction decay (FID) signal, $T2^*$ relaxation determines the actual rate of decay observed. $T2$ and $T2^*$ only happen when the net magnetization vector M is in the $xy-$transverse plane. These two relaxation processes do not occur when M is along the $z-$axis.[7]

The signal loss over time is dependent on $T2^*$ relaxation, and it follows an exponential decay[7]:

$$M_{xy}(t) = M_{xy}(t=0) \cdot e^{-t/T2^*} \tag{1.4.2}$$

According to Eq.1.4.2, the magnetization seen on the transverse plane at time zero ($M_{xy}(t=0)$) will fade exponentially with time t and a time constant $T2^*$.

When field in-homogeneities are neglected, relaxation proceeds more slowly, with a $T2$ time constant (rather than $T2^*$) determining the rate. This is similarly an exponential decay, but according to $T2$.[6],[7]

$$M_{xy}(t) = M_{xy}(t=0) \cdot e^{-t/T2} \tag{1.4.3}$$

1.5 MRI Sequences

In general, radio-frequency excitation, switching of spatial encoding gradients, relaxation duration, and signal measurements all follow an accurate and predetermined timing pattern known as the (MRI) sequence. A pulse sequence is the measurement technique used to obtain an MR image. It includes the hardware instructions (RF pulses, gradient pulses, and timings) required to capture data in the appropriate method. The pulse sequence actually run during the measurement, as implemented by most manufacturers, is specified by parameters directly selected by the operator (e.g., TR, FOV) and variables described in template files (e.g., relationships between RF pulses and slice selection gradients). This enables the operator to generate a high number of pulse sequences from a small set of template files.[12]

Depending on how the various types and variants reported in the last 40 years are recorded and classified, there could be dozens, hundreds, or maybe thousands of possible MRI sequences. In practice, MRI sequences are typically classed as either gradient recalled echo (GRE) or spin echo (SE).[15],[17] GRE sequences, in essence, use a radio-frequency excitation pulse, spatial encoding, and direct measurement of the stimulated magnetization. Spin echo sequences employ a second radio-frequency pulse, the so-called refocusing pulse, after stimulation and before measurement. It reverses or refocuses the effects of B_0 in-homogeneity and

susceptibility. Spin echo sequences are slower than GRE sequences, but being more robust in signal behavior.[12] The turbo or fast spin echo sequence, a faster spin echo version, produces more than one echo per excitation and is a clinical MRI workhorse.[15],[17]

1.5.1 MRI Sequence Parameters

The echo time (TE) and repetition time (TR) are two important MRI sequence parameters that can generally be modified by the user at the scanner. TE is the time elapsed between the excitation and the measurement of the signal in the transverse plane.[6],[13][14],[15],[17] This is significant because the longer the user-defined TE, the longer the tissue-specific $T2$ decay occurs. As a result, the acquired image has a higher $T2$ weighting. TR is the amount of time that elapses between repeated measurement cycles or excitations.[6],[13][14],[15],[17] If the defined TR is too short in comparison to the characteristic $T1$ relaxation duration of the examined tissues, the corresponding longitudinal magnetizations will not be able to fully recover before the next excitation, resulting in a $T1$ weighting of the magnetization. As a result, the reconstructed image is also $T1$ weighted.[18] The repetition time, TR, in a spin echo sequence is the period between successive excitation pulses for a given slice. The time between the excitation pulse and the echo maximum is known as the echo time, or TE.

In MRI, $T1$ and $T2$ weightings are dominant or strong signal weightings, allowing for excellent tissue distinction in images. The third fundamental MRI weighting, proton density weighting, is generally revealed in morphological acquisitions with both low $T1$ and low $T2$ weighting. The quantity of spins/protons in the tissue determines the weighting. In comparison to $T1$ and $T2$ weighing, proton density weighting is weak, especially in the brain.[18]

The exact sequence timing pattern determines the characteristic brightness of the different tissues in the reconstructed images due to proton density and $T1$ and $T2$ weighting.[18]

1.5.2 Spin Echo Sequences

A spin echo sequence is a widely known pulse sequence used in MR imaging. It is composed of RF pulses that are 90° and 180°. The excitation RF pulse is 90°, while the refocusing RF pulse is 180°, resulting in a spin echo. The 180° refocusing pulse is used to eliminate the constant static magnetic field distortions. However, because of random spin-spin interaction among the spins, the refocusing pulse cannot compensate for local and field inhomogeneities.[6] As previously stated, the repetition time or TR is the time interval between the application of a 90° pulse and the application of the next excitation pulse in a spin echo sequence. The time interval between the excitation pulse and the peak of the signal produced is known as echo time or TE.[19],[20] The extended scan time is the main disadvantage of the SE sequence.[20],[21]

1.5.3 HASTE: Half–Fourier Single Shot Turbo Spin Echo Sequence

On Siemens MRI scanners, HASTE is a turbo spin echo pulse sequence. Turbo spin echo (TSE) or fast spin echo (FSE) is a variant of multi-echo spin echo. The primary distinction between these two sequences is that in TSE, each echo is sampled with a separate phase encoding value, whereas in multi-echo spin echo, the same phase encoding gradient is applied to all echoes over the TR interval.[21]

As a result, numerous lines of $k-$space are sampled during each TR time. Because the time delay between two 180° pulses is fixed in TSE, the inter-echo spacing is always constant. The number of lines of $k-$space filled with data from the same number of spin echoes acquired at the same TR time is known as the Turbo Spin factor or Echo Train Length (ETL). When compared to a single spin echo sequence, this factor determines how many times the overall scan duration is reduced. The shorter the scan duration, the greater the value of this parameter.[6] HASTE might be classified as a TSE sequence with the highest turbo spin echo value (ETL).[6] There is, however, a significant difference between these two imaging approaches. TSE collects all of the lines in $k-$space and completes the image reconstruction by using numerous excitation pulses. HASTE, on the other hand, employs the so-called one-

shot approach, in which the complete $k-$space is acquired in a single TR interval.[21] HASTE reconstructs the whole image using only one initial excitation pulse followed by the requisite number of echoes.[21]

As a result, HASTE can be thought of as a single-shot TSE sequence. This sequence uses a technique known as half-Fourier $k-$space acquisition. This approach takes advantage of the fact that $k-$space has Hermitian or conjugate symmetry.[21] As a result, only around half of the $k-$space data must be gathered during TR[20] while, using $k-$space conjugate symmetry, the rest of the space can be calculated. As a result, HASTE combines TSE with a partial Fourier method. Thus, the HASTE imaging technology produces images with high spatial resolution in less than one second each slice. The relatively low signal to noise ratio or SNR[21] of the HASTE sequence, due to its long TE values, is one of the sequence's significant drawbacks in clinical practice.

1.5.3.1 Image contrast in HASTE sequence

After each TR interval, all k space in HASTE is filled with data, and the following 90° pulse will excite a different slice. As a result, TR is infinite by definition, and images with $T1$ contrast cannot be acquired in a single shot. Because the majority of lines in the middle of $k-$space is filled with data received from echoes with long TE, HASTE pictures are often predominantly $T2W$.[21],[22]

1.6 Gradient Echo Sequences

Gradient echo sequences are a type of imaging technique in which the protons are not refocused using a 180° pulse. Only gradient reversal is used to generate the echo signal. Proton dephasing is caused by the use of imaging gradients. This dephasing is reversed by applying a second gradient pulse of the same time and magnitude but opposite polarity, resulting in a gradient echo. To create the echo signal, all gradient echo sequences require gradient reversal pulses in at least two directions-the slice selection and readout directions. In most cases, excitation angles of less than 90° are used. In gradient echo sequences, the absence of the 180° RF pulse has resulted in severe Pulse Sequences.[18] Because the signal decay is influenced by the static sources of proton dephasing-B_0 inhomogeneity and magnetic susceptibility differences-the TE dictates the amount of $T2^*$ weighting in a gradient echo image rather than just $T2$ weighting as in a spin echo image. As a result, the total signal level in gradient echo images will be lower than that of spin echo images acquired with similar acquisition parameters. Gradient echo sequences' image quality is also more sensitive to metal implants and the anatomy under inquiry. Furthermore, depending on the chosen TE, fat and water protons inside a voxel contribute variable quantities of signal, a process known as phase cycling.[18]

2. Microwaves and Hyperthermia

2.1 Introduction to Microwaves

Microwaves are part of the electromagnetic (EM) spectrum, which includes radio waves and gamma ($\gamma-$)rays (Fig.2.1.1). The electromagnetic spectrum can be expressed in terms of frequency (measured in Hertz), wavelength, and energy. Shorter waves with a higher energy value, such as UV, are classified as ionizing because they create enough energy to produce ions at the molecular level, causing DNA and protein damage. While longer waves, such as visible light, are categorized as non-ionizing, they can still induce thermal damage; however, this damage is not caused by ions. Microwaves are a form of electromagnetic radiation with free-space wavelengths ranging from $1m$ to $1mm$ and frequencies ranging from $300MHz$ to $300GHz$.[23]

The most frequent microwave frequency is around $2.45GHz$, which is within the Industrial Scientific and Medical (ISM) radio band and is reserved for such uses.[24] Microwave energy has been successfully used in medicine in recent years to cure diseases such as cancer and microbial infections through ablation therapy. There is growing interest in employing microwave frequencies other than $2.45GHz$ to treat diseases; nevertheless, there is still a lack of understanding of the mechanisms by which microwaves generate biological changes in organisms. In this study, we evaluate current literature on the uses of microwave energy over a range of frequencies in order to demonstrate state-of-the-art microwave improvements in the medical profession.[25],[26]

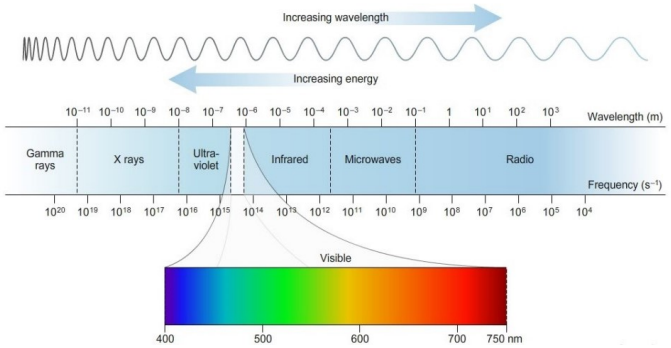

Figure 2.1.1: Electromagnetic spectrum. A depiction of the range of frequencies and wavelengths in the electromagnetic spectrum and the sub-ranges, as the wavelength increases the energy of the wave decreases.[24]

2.2 Electromagnetic Fields

An electromagnetic field is composed of both a magnetic and an electric field, which are formed by positively or negatively charged particles (Fig.2.2.1).[23] An electric field is created when particles obtain a charge, either positive or negative, by electron transfer. When electrically charged particles begin to travel, they generate an electric current, which generates a magnetic field around the electric current.

A magnetic field can be induced even if the electric field is not moving; if the charge of the electric field fluctuates, a fluctuating magnetic field will be induced. Because of their linked nature, the fields can sustain each other if the correct balance is established, and once sustained, an electromagnetic field releases directional electromagnetic waves when the fields fluctuate.[27] The principles of attraction govern both magnetic and electric fields, stating that opposite charges always attract while 'same' charges repel. The attraction or repulsion intensity is inversely proportional to the distance between the charges. Chemical bonding between atoms via charged electrons and protons is one of the best instances of these principles; these interactions may be mathematically explained using Coulomb's equation.[28]

Magnetic fields are created by the presence of two charges that create field lines, and the points at which these lines meet are referred to as poles, such as the Earth's North and South poles, and such magnetic charges can only exist as dipoles, not monopoles. Maxwell's equations, for example, confirm the electromagnetism model and define how fluctuating electric and magnetic fields (Fig.2.2.1) propagate at a constant speed.[29] Electromagnetic fields can behave as both waves and particles at the same time; the waves flow outwards from their source and can flow through a medium or a vacuum. The wave travels at the speed of light in a vacuum; similarly, the air in our atmosphere is thin enough not to effect wave propagation; but, while traveling through medium, the refractory index of the media will alter wave movement.

Other factors affect propagation in media such as water; the high permittivity and electrical conductivity of water considerably enhance the angle of refraction.[30],[31]

Another thing to consider is the microwave's capacity to interact with polar molecules; water molecules are polar; therefore, the microwave interacts with it as it goes through it as a medium. When exposed to microwaves, polar molecules rotate in an attempt to align with the waves' fluctuating charges; the rotation generates heat and is the basis of microwave heating.[32]

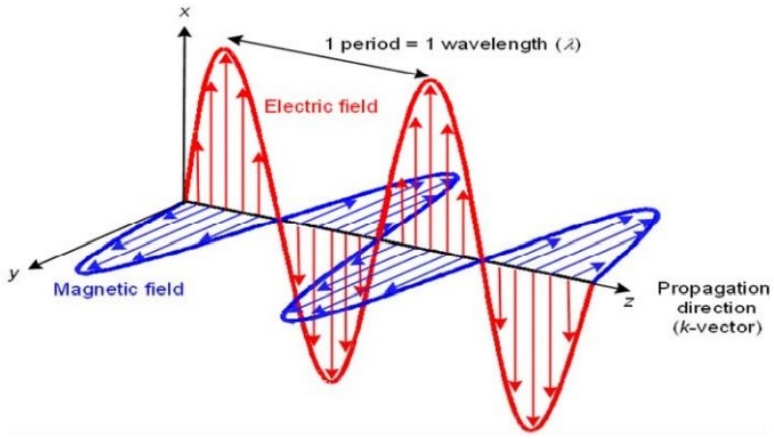

Figure 2.2.1: Electromagnetic wave diagram. Showing the direction of the wave, the direction and oscillation of the electric field and the direction and oscillation of the magnetic field. Each runs perpendicular to another; direction travelling along the $x-$axis, electric along the $y-$axis and magnetic along the $z-$axis.[33]

2.3 Microwave Dielectric Heating

The principles of microwave chemistry rely on the efficient heating of materials by microwave dielectric heating effects.[34] Microwave dielectric heating is based on a certain material's ability to absorb microwave energy and convert it to heat (for example, a solvent or reagent).

Microwaves are electromagnetic waves that have both a magnetic and an electric field component (Fig.2.2.1). For most practical reasons linked to microwave synthesis, the electric component of the electromagnetic field is more important for wave–material interactions, however magnetic field interactions (e.g., with transition metal oxides) can be important in some cases.[35]

The electric component of an electromagnetic field generates heat via two mechanisms: dipolar polarization and ionic conduction. The dipolar polarization mechanism (Fig.2.3.1.a) describes the interaction of the electric field component with the matrix. When irradiated with microwaves, a substance must possess a dipole moment in order to generate heat. When microwave frequencies are applied to the sample, the dipoles align in the applied electric field. The dipole field attempts to realign itself with the alternating electric field as the field oscillates, and energy in the form of heat is released as a result of molecular friction and dielectric loss. The quantity of heat produced by this process is proportional to the matrix's capacity to align itself with the frequency of the applied field.

No heating occurs if the dipole does not have enough time to realign with the applied field (high frequency irradiation) or reorients too rapidly (low frequency irradiation). The assigned frequency of $2.45GHz$, which is used in all commercial systems, lies between these two values and allows the molecule dipole time to align in the field but does not allow it to accurately follow the alternating field. While a result, as the dipole reorients to align itself with the electric field, the field is already shifting, resulting in a phase discrepancy between the field's orientation and that of the dipole. Because of the phase difference, energy is lost from the dipole due to molecule friction and collisions, resulting in dielectric heating. To summarize, field energy is delivered to the medium, and electrical energy is turned into kinetic or thermal energy, and then into heat.

It should be noted that the interaction between microwave radiation and the polar solvent, which happens when the frequency of the radiation is close to the frequency of the rotating relaxation process, is not a quantum mechanical resonance phenomenon. Transitions between quantized rotational bands are not involved, and energy transfer is the outcome of a collective phenomenon involving the bulk rather than a feature of a single molecule.[34]

Frictional forces between polar molecules, whose rotational velocity has been increased by the coupling with microwave irradiation, generate

heat. It's also worth noting that microwave irradiation can't heat gases since the distance between revolving molecules is huge. Similarly, because the water dipoles are restricted in a crystal lattice and cannot move as freely as they may in the liquid state, ice is -almost- microwave transparent.

The ionic conduction mechanism (Fig.2.3.1.b)[34] is the second primary heating mechanism. When dissolved charged particles in a sample (typically ions) swing back and forth under the influence of the microwave field, they collide with their nearby molecules or atoms, which is known as ionic conduction. These impacts generate heat by causing agitation or motion. As a result, if two samples having equal volumes of distilled water and tap water are heated by microwave irradiation at a constant radiation strength, the tap water sample will heat up more quickly due to its ionic content. When considering the heating behavior of ionic liquids in a microwave environment, such ionic conduction phenomena are especially essential. In terms of heat-generating capacity, the conductivity principle has a far stronger effect than the dipolar rotation mechanism.

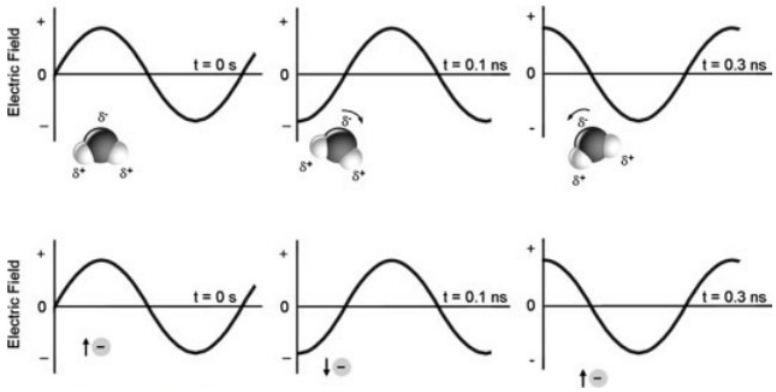

Figure 2.3.1: (a) Dipolar polarization mechanism. Dipolar molecules try to align with an oscillating electric field. (b) Ionic conduction mechanism. Ions in solution will move in the electric field.[34]

Microwave irradiation can create a flow of electrons on the surface of strongly conducting or semiconducting materials such as metals, resulting in a similar heating mechanism. This flux of electrons has the potential to heat the material via ohmic resistance heating mechanisms. This is crucial in the context of organic synthesis for heating strongly microwave absorbing materials such as thin metal sheets (Pd, Au), graph-

ite supports, or so-called passive heating elements built of silicon carbide.

2.4 Prospective Applications of Microwaves in Medicine

One promising technology is a method of applying radio frequency using microwaves (with frequencies ranging from $300MHz$ to $300GHz$) to for diagnostic and therapeutic clinical applications. Hollman proposed the use of microwaves for medicinal reasons between 1938 and 1939, predicting that electromagnetic (EM) waves may generate deep tissue heating without significant skin heating.[36]

In 1939, Hemingway and Stenstrom from the United States offered a similar work that reviewed high-frequency waves (short wavelength). They concentrated on a microwave-based method of applying heat for therapeutic applications in medicine.[37] However, due to a lack of microwave sources and clinical trial restrictions, the microwave frequency was limited to $100MHz$. The possibility of employing microwaves for diagnostic and therapeutic purposes developed quickly in the early 1980s.[38],[39],[40],[41]

Because of the rapid growth of semiconductor technology and diverse signal processing methods, there is a growing interest in the study and development of medical applications based on microwave techniques. Microwave medical applications can be classified into three broad categories based on how microwaves are used:

1. Microwaves can be used for patient therapy (e.g., hyperthermia and diathermy). It can be utilized for either thermal or non-thermal effects.
2. Microwaves can be used to diagnose diseases and generate tomographic images by using permittivity or attenuation data.
3. Microwaves can be utilized as a data telemetry tool.

2.5 Hyperthermia

2.5.1 History of Hyperthermia

W. Bush published the first study on hyperthermia in 1886.[42]According to Bush, a sarcoma on a 43-year-old woman's face was treated when she experienced fever induced by erysipelas. In 1898, in Sweden F. Westermark attempted to circulate high-temperature water for the treatment of an inoperable uterine cervix cancer, and the results were positive.[43] Applied research was conducted alongside with basic research in the early twentieth century. However, because the heating method and temperature-measuring technology, had not progressed sufficiently at the time, the positive clinical use of hyperthermia treatment was not implemented.

As a result, radiotherapy, surgery, chemotherapy, predominated in cancer therapy. In such circumstances, Westermark reported a selective antitumor effect for a tumor treated at 40–45°C. Westra, Overgaard, and others[44],[45] later supported hyperthermia's effect. The interest in hyperthermia increased, especially when Crile[46] and Ben-Hur[47] reported an improved effect when hyperthermia and radiotherapy were combined, and research grew quickly. Hyperthermia research began in the 1970s at a hyperthermia institute.

In 1975, the American Cancer Society conducted a symposium in Washington, and the activity has continued since then. The application of microwaves to cancer treatment was the focus of a session of the IEEE's Microwave Theory and Techniques (MTT) Society's International Microwave Symposium in 1977, and a special issue of the MTT Transactions was published the following year.[48] In 1981, a hyperthermia organization was formed in the United States, and in 1983, the European Hyperthermia Institute was founded in Europe. Hyperthermia research began in Japan in 1978, with the forming of the Japanese Society of Hyperthermia Oncology in 1984.

Recently, multidisciplinary therapy, in which hyperthermia is used in conjunction with radiotherapy, chemotherapy, surgical therapies, immunotherapy, and other treatments, has gained growing attention.

2.5.2 Microwave Hyperthermia

Microwave hyperthermia is a field that is closely related to microwave thermographic imaging. This is a method of reducing or eliminating carcinomas by heating them with radiofrequency or microwave electromagnetic waves. During heating, temperatures should be kept between 42 and 45 degrees Celsius. Normal tissues may be irreversibly damaged above these temperatures; below these temperatures, heating may stimulate tumor growth. Microwave thermogaphy offers a lot of potential as a new tool for monitoring temperatures in the field. It is not yet widely used for this purpose because adequate temperature resolution with depth has not yet been attained, and microwave thermography and hyperthermia applicators have not yet been merged. The development of microwave thermography for this application is critical because it would eliminate a number of issues associated with present intrusive temperature monitoring technologies. (Patient discomfort, selection of optimal probe position and correct positioning, and limited information about tissue temperatures away from probes)

Wave absorption and penetration are affected by tissue composition and surfaces. Because dosimetry is dependent on tissue dielectric characteristics, it is extremely difficult to quantify. Tumors are known to be selectively sensitive to heat treatment at microwave frequencies, but estimates of the heating dosages (temperature and duration) required to eradicate tumors and the amount to which normal tissues are spared or destroyed by the microwave field are needed. Thus, biophysical data such as high frequency relative permittivity and electrical conductivity are required to develop and forecast the range and safety of a microwave hyperthermia therapy system. It is critical to determine values and ranges for normal and diseased tissues.[49],[50],[51],[52] One of the operating frequencies of microwave hyperthermia equipment is $2.45GHz$.

2.6 Dielectric Characteristics of Tissues

The study of the dielectric characteristics of tissues falls under the purview of both basic and applied science. Theoretical issues and key findings in this field have been extensively addressed (Schwan, 1957)[53], Foster and Schwan[54], Pething 1984[55], Pething and Kell 1987[56], Foster and Schwan 1989[57] as well as Stuchly and Stuchly 1980[58]. Foster and Schwan remark on the historical context offered by more than a century of interest in the electrical characteristics of tissues, and they examine the fundamental principles of dielectric phenomena in biological materials and their interpretation in terms of cellular interactions. Pethig and Kell cover similar terrain, providing an overview of hypotheses developed to explain dielectric properties in terms of underlying molecular processes. All publications share a more or less thorough tabulation of dielectric properties of tissues chosen to illustrate the authors' theoretical discussions.

Later, Geddes and Baker (1967)[59] summarized early reports on tissue specific resistance; Stuchly and Stuchly (1980)[58] tabulated the dielectric properties of tissues in the frequency range $10kHz$ to $10GHz$; and Duck (1990)[60] expanded the survey by including more recent data.

Understanding the interaction of radio and microwave radiation with biological systems necessitates background knowledge of some of the laws that describe the properties of radio and microwave radiation. Radio and microwave radiation's physical processes are governed by four laws known as Maxwell's equations. These equations are mathematical expressions of experimental observations. All macroscopic electromagnetic phenomena can be deduced with mathematical vigor and exactness from these four electromagnetic principles or laws.

This chapter explains the principles of radio and microwave radiation in order to encourage abasie comprehension. Rather of attempting to provide a concise explanation of all that radio and microwave radiation includes, the features of radio and microwave radiation that are most relevant to biological interactions are highlighted. If the reader seaking a full physical description of radio and microwave radiation, he or she should consult any widely available texts devoted solely to these topics.

(Adams, 1969[61]; Gandhi, 1981[62]; Kraus and Carver, 1973[63]; Jordan and Balmain, 1968[64]; Collin, 1966[65]; Collin and Zucker, 1969[66]; Ramo et al., 1965[67]; Harvey, 1963[68].

2.7 Interactions with biological tissues

The effects of the interaction of RF and microwave radiation with biological tissues rely upon three parameters:

1. The frequency and the form of Electromagnetic waves that propagate into the living system.
2. Specific to their electromagnetic properties, the type of interaction of waves with tissues.
3. The secondary effects that could be induced by the primary interaction.

The term "interaction" emphasizes the fact that the final outcomes are not only influenced by the field's action but also by the living system's reaction.

EM field theory's physical laws can be used to study and explain the observed phenomena. This applies to the nonionizing part of EM radiation, with which we are presently focused (RF and microwaves). Consequently, accurate knowledge of the various tissue electrical properties is crucial for biological applications of EM radiation. Some of the first researchers into the electrical characteristics of biological tissues made significant contributions to our understanding of how microwave and radiofrequency fields interact with biological tissues. Schwan's work[53] should be studied for original reviews of tissue electrical properties.

Considering biological tissues contain $75\% - 80\%$ water, the dielectric and conductivity properties of biological materials in the microwave frequency range are substantially determined by the relaxation properties of biological membranes and tissue water.

2.8 Fundamentals of Wave Propagation

Radio and microwave radiation are composed of electric and magnetic fields that change with time and position, and propagate through free space at the speed of light, $(2.998 \times 108)rn/sec$. The fluctuation in this speed in the material medium through which the wave propagates is determined by the medium's permittivity and permeability.

Maxwell's equations govern the propagation, scattering, and transmission of radio and microwave radiation. Actually, these equations describe all electromagnetic phenomena in continuous media that are static in relation to the coordinate system used. They are valid for linear or nonlinear, isotrope or anisotrope, homogeneous or nonhomogeneous medium in the frequency range from zero to microwave frequencies, including numerous optical phenomena. Maxwell's equations[69] are microscopic laws that define the relationship between time-averaged electric and magnetic fields and space.[70]

They are applied to regions or volumes with dimensions greater than atomic dimensions. The observation time intervals are assumed to be long enough to allow for the averaging of atomic fluctuations.

Maxwell equations are illustrated below:

Gauss's Law for electric fields:

$$\nabla \cdot \epsilon_0 \vec{E} = \rho_v \tag{2.8.1}$$

Gauss's Law for magnetic fields:

$$\nabla \cdot \vec{B} = 0 \tag{2.8.2}$$

Faraday's Law of induction:

$$\nabla \times \vec{E} = -\frac{\partial \vec{B}}{\partial t} \tag{2.8.3}$$

Ampere's circuital Law:

$$\nabla \times \frac{\vec{B}}{\mu_0} = \vec{J} + \frac{\partial \epsilon_0 \vec{E}}{\partial t} \tag{2.8.4}$$

In these equations $\mu_0 = 4\pi \cdot 10^{-7} Henry/m$ and $\epsilon_0 = 8.854 \cdot 10^{-12} Faraday/m$ are the permeability and permittivity of free space, respectively (Lorraine and Corson, 1970)[71]

When an electric or magnetic field is applied to a material, it exerts forces on the constituent charged particles, causing them to move or rearrange. This changes the properties of wave propagation by modifying the impressed fields. The interaction of EM waves with tissues can be described by the following three basic mechanisms:

1. Displacement or drift of conduction (free) electrons and ions in tissue as a result of the force exerted by EM fields
2. Polarization of atoms and molecules to produce dipole moments
3. Orientation of existing dipoles in the direction of the applied electric field.

As a result of (1) there will be a conduction current $\vec{I} = \sigma \cdot \vec{E}_m$, where $\vec{E_m}$ is the electric field inside the material and is the material's conductivity. The other two mechanisms are related to the material's bound (not free) existing charges. Polarization, for instance, is related to the displacement of the bonded negative electron cloud from the equilibrium position relative to the positive nucleus (Fig.2.8.1). Orientational polarization occurs in materials with permanent electric dipoles that are randomly oriented in the absence of an external field but experience an orientation towards the applied electric field vector by a factor depending on the strength of E. A common example of a material that exhibits this behavior is water.

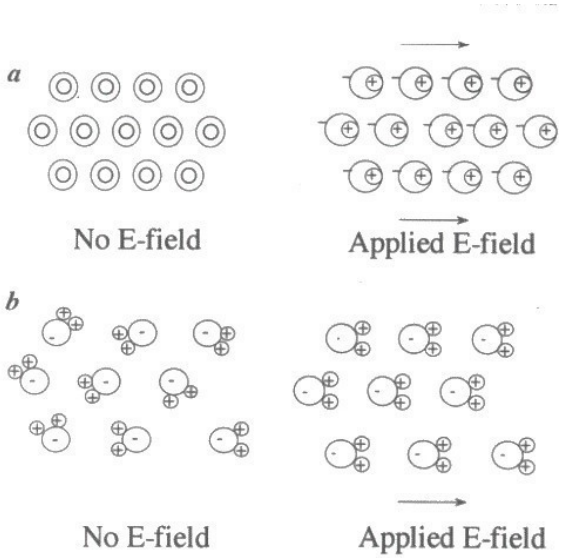

Figure 2.8.1: Electric polarization effects in sample models of (a) non-polar material and (b) polar substance, e.g. H_2O.[72]

As polarization currents emerge from the displacement of the charges in the time-varying field, there will be an additional polarization charge inside the material as a result of these polarization effects. These generated charges and currents are new sources of electric and magnetic fields, and Maxwell's equations should be modified accordingly.

Eq.2.8.1 -Gauss's law for the electric field- for example is modified to Eq.2.8.5:

$$\nabla \cdot \epsilon_0 \vec{E} = \rho_v + \rho_\rho \tag{2.8.5}$$

which now incorporates the excess bound charge, ρ_ρ, generated by the polarization process. Similarly, Ampere's law (Eq.2.8.4), should incorporate a polarization current term $\vec{J}_\rho$.

$$\nabla \times \frac{\vec{B}}{\mu_0} = \vec{J} + \frac{\partial \epsilon_0 \vec{E}}{\partial t} + \vec{J}_\rho \tag{2.8.6}$$

All of the aforementioned interaction processes, as well as the corresponding modifications in Maxwell's equations, can, however, be described by a property of the material known as complex permittivity ϵ^*.

In more detail:

Human tissues have frequency-dependent dielectric properties. This is explained by the various polarization mechanisms induced by E-fields in human tissues. Dielectric dispersion is the term used to describe a significant change in dielectric characteristics over a frequency range, by convection. A tissue's dielectric spectrum is defined by three primary relaxation regions, , and at low, medium, and high frequencies, (Schwan, 1957)[53], as illustrated in Fig.2.8.2, as well as various smaller dispersions such as δ, the frequently reported dispersion. (Their origins and characteristics have been extensively documented (for example, Grant (1981) and elsewhere)[73]. The $\alpha-$dispersion is most common below a few kHz, $\beta-$dispersion occurs in the frequency range of tens of kHz to tens of MHz, and $\gamma-$dispersion in the microwave frequency range. The $\gamma-$dispersion, which results mostly from polarization due to water molecule reorientation, has been extensively investigated and has numerous uses in various fields (Thuery, 1991;[74] Nelson, 1991;[75] Metaxas and Meredith, 1983[76]). The low-frequency dielectric behavior of tissues is dominated by heterogeneous structure and composition, as well as ionic activity within the tissues. The interfacial polarization (Maxwell-Wagner effect) of biological membrane systems is well recognized to cause $\beta-$dispersion. This was discovered primarily through the study of blood tissues (erythrocyte suspensions) in the early twentieth century (Hober, 1910[77]; Fricke and Curtis, 1935[78]; Schwan, 1957[53]. Dielectric studies of biological or other electrolyte systems below a few kHz have proven challenging, owing to strong electrode polarization at these frequencies. Partly as a result of this, the mechanism of biological tissue a dispersion remains unclear.

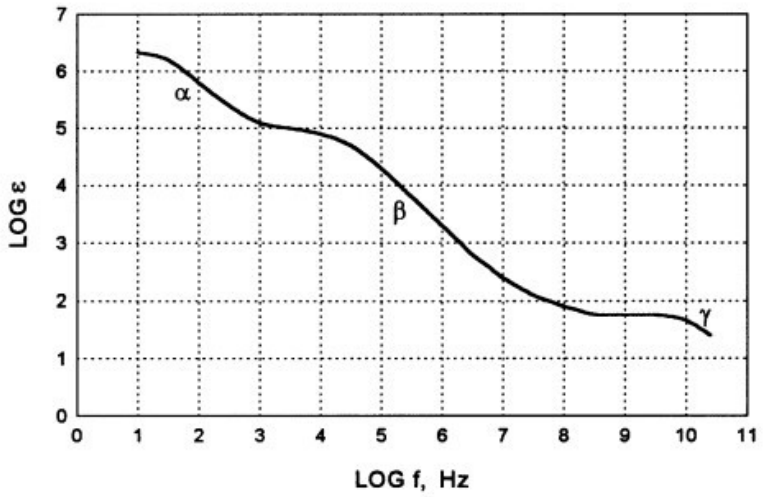

Figure 2.8.2: Typical frequency dependance of biological tissues. A measurements of muscular tissue (Schwan, 1957).[53],[39]

Each of these relaxation regions is, in its most simple form, the manifestation of a polarization mechanism characterized by a single time constant τ, which, to a first order approximation, yields to expression (Eq.2.8.7) for the complex relative permittivity (ϵ') as a function of angular frequency (ω). This frequency-dependent behavior commonly refers to the dielectric relaxation response of human tissues and can be expressed by the following Debye equation (1929)[79]:

$$\epsilon^* = \epsilon_\infty + \frac{\epsilon_0 - \epsilon_\infty}{1 + j\omega\tau} \tag{2.8.7}$$

where

$$\epsilon^* = \epsilon_0 \cdot \epsilon_r \tag{2.8.8}$$

is the complex permittivity of the medium, ϵ_r is the relative permittivity, defined as the ratio of the electric displacement in a medium to that which would be produced in free space by the same field.

The most important relaxation process at microwave frequencies is orientational polarization, in which molecules or molecular groups rotate; this is dependent upon the molecules' internal structures and molecular arrangement. When the polar molecules are very large, the frequency of the field is high, or the viscosity of the medium is high the molecules do not rotate rapidly enough to achieve equilibrium with the field. The polarization then acquires an out of phase of the field component, resulting in energy thermal dissipation. The absorption qualities of the medium are described by this ohmic or loss current (Smythe, 1955; Von Hippel, 1954)[80],[81]. In order to represent this type of lossy material, a complex representation of the dielectric constant is required.

So, the relative permittivity ϵ_r can be expressed in terms of real (ϵ') and imaginary (ϵ'') components:

$$\epsilon_r = \epsilon' - j\epsilon'' \tag{2.8.9}$$

The real component ϵ' accounts for the additional polarization of bound changes, while ϵ'' represents the conduction of free charges, and is related to the conductivity by:

$$\sigma = \omega\epsilon_0\epsilon'' \tag{2.8.10}$$

where $\omega = 2\pi f$ is the angular frequency of the applied field.

The ϵ_0 and ϵ_∞ at Eq.2.8.10 refers to the dielectric constant at low and high frequencies. τ is the relaxation time, which is the required time for a stimulated dipole to return to its original state.

The real and imaginary parts of ϵ may be written as:

$$\epsilon' = \epsilon_\infty + \frac{\epsilon_0 - \epsilon_\infty}{1 + (\omega\tau)^2} \tag{2.8.11}$$

$$\epsilon'' = \frac{(\omega\tau)\epsilon_0 - \epsilon_\infty}{1 + (\omega\tau)^2} \tag{2.8.12}$$

Instead of relaxation time τ , these equations are frequently stated in terms of a characteristic frequency f_C. The equation that connects them is:

$$f_C = (2\pi\tau)^{-1} \tag{2.8.13}$$

Equations (Eq.2.8.11, Eq.2.8.12) for water at $20°C$ are shown in Fig.2.8.3

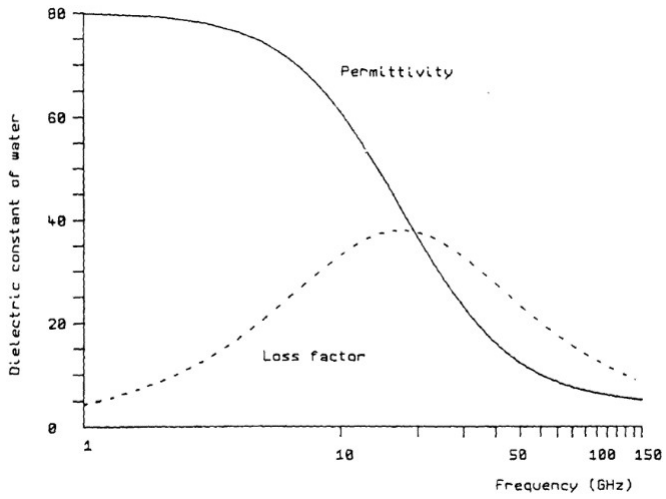

Figure 2.8.3: Debye dispersion of water at $20°C$.[39]

Hurt (1985)[82] modeled the dielectric spectrum of muscle as the sum of five Debye dispersions plus a conductivity term in which σ_i is static ionic conductivity and ϵ_0 is free space permittivity:

$$\epsilon^* = \epsilon_\infty + \sum_{n=1}^{5} \frac{\Delta\epsilon_n}{1 + j(\omega\tau)^2} + \frac{\sigma_i}{j\omega\epsilon_0} \tag{2.8.14}$$

However, due to the complexity of biological material's structure and composition, each dispersion region may be widened by several contributions. The term relaxation time is only considered a first-order component in the Debye equation, and it is insufficient to predict dispersion across a wide frequency range. In real material, which could be a mixture of several different substances, a solution, or materials that have a nonlinear relaxation process, a distribution of relaxation times is expected. To account for the multiple time constants of different polarization mechanisms, higher-order equations in terms of several relaxation durations must be considered.

To enable this, Cole and Cole modified the Debye equation in such a way that the Cole-Cole equation[83] provides multiple dispersion terms based on numerous reported experimental data from various tissues.[83],[84],[85] The introduction of a distribution parameter could empirically account for the broadening of the dispersion, providing an alternative to the Debye equation known as the Cole–Cole equation.

The Cole-Cole equation is given below:

$$\epsilon^* = \epsilon_\infty + \frac{\epsilon_0 - \epsilon_\infty}{1 + (j\omega\tau)^{1-\alpha}}, \quad 0 \leq \alpha \leq 1 \tag{2.8.15}$$

where the distribution parameter, α, is a measure of the broadening of the dispersion. As a result, the spectrum of a tissue can be better represented in terms of multiple Cole–Cole dispersion.

$$\epsilon^* = \epsilon_\infty + \sum_n \frac{\epsilon_0 - \epsilon_\infty}{1 + j(\omega\tau)^{1-\alpha}} + \frac{\sigma_i}{j\omega\epsilon_0} \tag{2.8.16}$$

This may be used to predict the dielectric behavior across the specified frequency range using a set of parameters suited for each tissue.

Eq.2.8.16 can also be separated into real and imaginary parts. The Cole-Cole equation describes a symmetrical distribution of relaxation times, characterized by α. The Cole-Cole model is reduced to the Debye model when $\alpha = 0$.

2.9 Conductivity

The ϵ'' factor is related to the conductivity σ by the following Eq.(2.9.1):

$$\sigma = \omega \cdot \epsilon_0 \cdot \epsilon'' \tag{2.9.1}$$

where σ is the total conductivity of the material, which may include a contribution from frequency-independent ionic conductivity σ_i, depending on the type of the sample, i. In this expression, ϵ_0 represents the permittivity of free space and ω the field's angular frequency. The SI unit of conductivity is *Siemens* per *meter* (S/m), which assumes that ϵ_0 is given in farads per metre (F/m) and ω is in *radians* per *second* in the preceding expression. As a function of frequency, the dielectric characteristics are determined as ϵ' and ϵ'' values, or as ϵ' and σ values, as a function of frequency.

2.10 Permittivity of Water

It is known that water is by far the most abundant component in animals, and accounts for over 60% of total body mass in humans. For instance, it constitutes 93% of blood, about 80% of skeletal muscle, slightly less than 9% of fat, and roughly 70% of white matter (Altman and Dittner, 1964[86]; Schepps and Foster, 1980[87]. Water's fluid nature allows dissolved electrolytes and suspended compounds to diffuse to various areas of the cell or tissue. Roughly 62% of total body water is in the intracellular area, and about 38% is in the extracellular region (Guyton, 1969)[88].

Consequently, one might expect water to have a significant impact on biological materials' permittivity properties (i.e., dielectric constant and conductivity). Hence, we can consider water's dielectric characteristics as a function of frequency and temperature.

Water's permittivity exhibits a characteristic dispersion at microwave frequencies (Eisenberg and Kauzmann, 1969[89]; Franks, 1972[90]; Hasted,

1973[91]; Hasted and EI Sabeh, 1953[92]). The frequency dependence of the dielectric constant and conductivity of water at $37°C$ is shown in Fig.2.10.1.

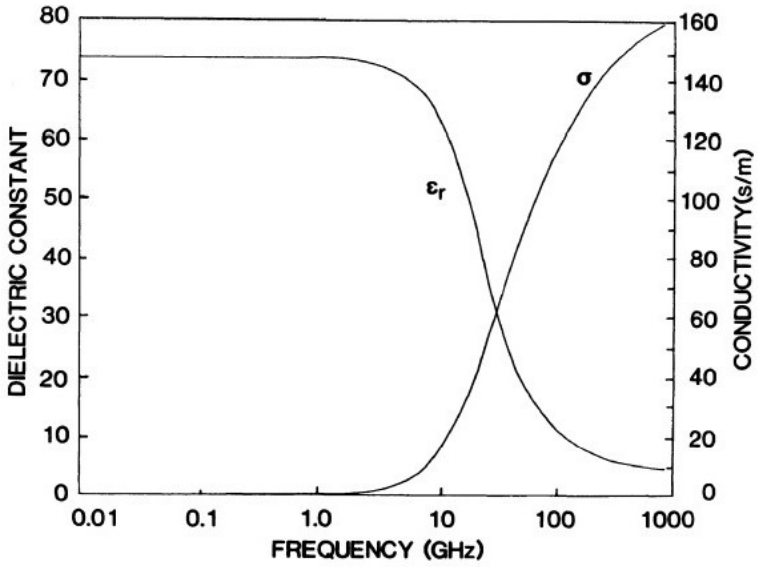

Figure 2.10.1: Dielectric constant and conductivity of free water at $37°C$.[39]

From Fig.2.10.1 it can be observed that at $37°C$, water has a relaxation frequency of around $32GHz$. From dc to $1.0GHz$, the dielectric constant and conductivity remain frequency invariant. Water begins to scatter at frequencies exceeding $3GHz$ to $5GHz$. At $35GHz$, the dielectric constant drops from 74 to around 28 before reaching a lower bound of 4.5. For frequencies up to and beyond the microwave region, on the other hand, conductivity grows almost monotonically. Water's dielectric behavior is characterized by a single relaxation process regulated by the rotation of individual water molecules as dipoles in a viscous fluid between dc and microwave frequencies[39].

2.11 Dielectric Properties of Biological Materials

According to their water content, biological materials can be classified into three major types. The first group includes fluids containing electrolytes, macromolecules, and other biological components, such as blood, vitreous humor, and cerebrospinal fluid, that has a high-water content (90% or more). Skin, muscle, brain, and internal organs make up the second, which has a modest water content (less than 80%). The final group consists of tissues that have a low water content (about 40%), such as bone, fat, and tendon (Lin, 1978)[93].

The determined dielectric constants and conductivities of tissue materials as a function of frequency and temperature will be summarized in this section. This section will also cover the dielectric constants and conductivities of a variety of different tissue materials.

Tissues are made up of cells that are encased in thin membranes and contain an intracellular fluid that comprises of different salt ions, polar protein molecules, and polar water molecules. Although some of the constituents are different, the extracellular fluid has similar amounts of ions and polar molecules. When an electric current I approaches a biological cell, as shown in Fig.2.11.1.a, it separates into two parts: one will bypass the cell by way of its surrounding fluid, as indicated by the elements R_0 and C_0 in the circuit, and the other penetrates the cell membrane, as indicated by the capacitors Q and the cell interior resistance R in the circuit.

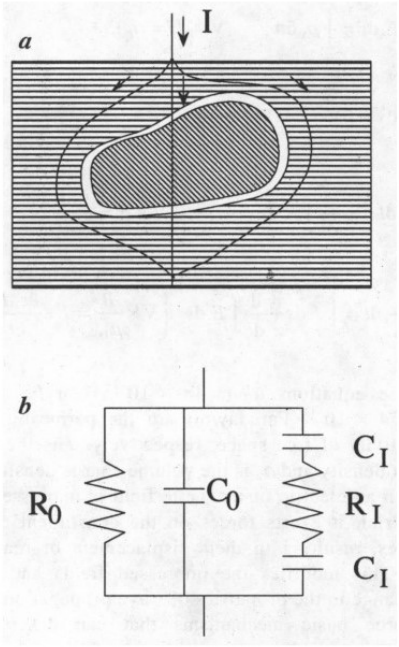

Figure 2.11.1: (a) Diagrammatic representation of a cell (b) equivalent circuit representing the electrical properties of biological cells R_0 and C_0 are the resistance and capacitance of the fluid surrounding the cell, while C_1 and R_1 are the cell membrane capacitance and resistance of the fluid inside the cell respectively[72].

A simplified equivalent circuit corresponding to the electrical behavior of tissues with high water content is shown in Fig.2.11.1b. The membrane of the cell has a high capacitance per unit area of approximately $1\mu F/cm^2$, and a resistance per unit area of more than $100\omega/cm^2$.

The capacitors' reactance ($l/\omega C_1$, where ω is the angular frequency of the EM wave) varies with frequency, causing the ratio of the two currents entering and bypassing the cell to be frequency dependent. The capacitive reactance of the cell membrane is so low at frequencies above $100Hz$ that it is considered to be shorted out. As a result, as long as one applies EM frequencies greater than $1kHz$, one can short circuit the membrane's high reactance and therefore heat the cytoplasm inside the cell.

At low frequencies, the cell membrane's capacitance works as an insulator, allowing current to flow exclusively in the extracellular media, which explains the tissue's low conductivity.

Factor σ increases as frequency increases, while ϵ' decreases with frequency. The capacitive reactance of the membranes reduces as the frequency rises, resulting in an increase in tissue conductivity. This can also be obtained from the Eq.2.9.1.

When the frequency of the EM field is compared to the time it takes to charge the cell membrane, the drop in ϵ' becomes apparent. As the frequency rises, there isn't enough time in each cycle for the cell membranes to fully charge. As a result of this, the total charge per cycle and membrane capacitance decreases with frequency. This is reflected in a drop in ϵ'.

Fat, bone, and muscle have a low electrolyte concentration. Due to this, the values σ and ϵ' for these and for other "dry" tissues are an order of magnitude lower than those for high-water-content tissues. Differential power absorption in different tissues is caused by these variances in σ and ϵ'.

Skin and muscle have nearly identical dielectric constants and conductivities (Cook, 1951)[94], with values in the range of blood and brain, reflecting their intermediate water content. It is worth noting that with increasing frequency, the dielectric constants decrease and the conductivities increase.

In a brief, the dielectric constants for tissues with increased water content are practically constant for frequencies between $100MHz$ and $10GHz$ because microwave frequencies are located between the two main dispersion regions ($\beta-$ and $\gamma-$ dispersions). The intracellular fluid can participate in current conduction because cell membranes have a high capacitance and become short-circuited for frequencies exceeding the $\gamma-$dispersion. As the frequency rises even higher, both current flow and membrane capacitance approach a plateau, causing the $\gamma-$dispersion, (which is caused by the polar characteristics of water).

The data presented above for $37°C$ can be summarized by sums of power series and Debye equations (Schepps and Foster, 1980)[95]:

$$\epsilon_r = 4 + 1.71^{-1.13} + \frac{\epsilon_s^m - 4}{1 + \left(\frac{f}{25}\right)^2} \tag{2.11.1}$$

$$\sigma = 1.35 f^{0.35} \sigma_{0.1} + 0.0222 f^2 \cdot \frac{\epsilon_s^m - 4}{1 + \left(\frac{f}{25}\right)^2} \tag{2.11.2}$$

In the equations above f is the frequency (GHz), and σ is the conductivity (mS/cm). The parameters ϵ and σ are reported in Fig.2.11.2 for many tissues.[39] These equations are used to estimate the dielectric characteristics of other soft tissues having more than 60% water by volume, and they apply to the whole frequency range covered in this Thesis.

	Volume fraction of water	Extrapolated microwave permittivity, ϵ_s^m	Conductivity at 1 GHz, $\sigma_{0.1}$ (mS/cm)	Extrapolated microwave conductivity, σ_s^m (mS/cm)
Brain				
Gray matter	0.84	44	7.0	11.3
White matter	0.74	34	4.8	7.5
Skeletal muscle	0.80	47	7.0	24.0
Liver	0.80	43	6.7	23.0
Fat	0.09	10	0.5	1.0

[a] Modified from Schepps and Foster (1980).

Figure 2.11.2: Microwave dielectric parameters for Eq.2.11.1,2.11.2 at $37°C$[39].

The electrical properties of bone, fatty tissue, and other low-water-content tissues have not been thoroughly studied. The exact process underlying their dielectric behavior is unknown, and measurements of dielectric constant and conductivity show considerable variability. This is due to the difficulties of manipulating fatty tissues in vitro without altering their fat and water content. Generally as mentioned above, tissues with low water content have a dielectric constant and conductivity

that is an order of magnitude lower than tissues with higher water content.

The Fig.2.11.3 lists the dielectric constants and conductivities for several additional tissues with substantial water content. Due to its significance in biological experiments involving microwave radiation, values for normal saline solution are also included. With increasing frequency above $1000MHz$, the conductivity rises and the dielectric constant decreases.

Frequency (MHz)	Wavelength in air (m)	Blood serum		Vitreous humor[b]		0.9% saline	
		ε_r	σ	ε_r	σ	ε_r	σ
100	3.0	73.3[c]	1.17[c]	70	1.6	78	1.67
200	1.5	69.3[c]	1.11[c]	70	1.6	78	1.68
400	0.75	68.5[c]	1.23[c]	70	1.6	74[d]	1.72[d]
500	0.60	68.7[c]	1.38[c]	70	1.6	78	1.72
700	0.43			70	1.6	77[d]	1.85[d]
1,000	0.30	69[c]	1.85[e]	70	1.6	77	1.88
2,500	0.12	71[g]	1.55[g]	70	2.7		
3,000	0.10	70[f]	3.76[f]	70	3.2		
5,000	0.06			69	5.4		
10,000	0.03	57.5[f]	12.6[f]	62	15.3	66[e]	11.1[c]
24.000	0.012	45[f]	38.0[f]	40	46.0		

[a] Values of the dielectric constant ε_r and conductivity σ are for 37°C and are adapted from Schwan (1957), unless otherwise indicated.
[b] Schwan (1958).
[c] Zore *et al.* (1967), 23°C.
[d] Schwan and Li (1953).
[e] Presman (1970).
[f] England (1950).
[g] Cook (1951), 2.36 GHz.

Figure 2.11.3: Relative dielectric constants and conductivities (S/m) for selected tissues with high water content[39].

Fig.2.11.4 shows the dielectric characteristics of several tissues with intermediate water content. It's worth noting that the dielectric constants and conductivities are reduced by around 30% to 40% compared to high-water-content tissues. For example, a number of 50 represents the dose to all of the tissues indicated at $1000MHz$, while a value of $1.0S/m$ represents all tissues with intermediate water content. The table shows that a vast number of tissue materials still need to have their electrical characteristics determined[39].

Although the dielectric constants and conductivities in this section were generated from tissues from a variety of species, there is very little variation in the measured values for each tissue type. Fatty tissue, which has a low dielectric constant and conductivity as well as a low electrolyte content, is an exception. Depending on the animal species, the water content of fatty tissues can range from a few percent to over 40%. (Schwan, 1958)[95]. Because water has such a high dielectric constant and conductivity, the electrical characteristics of fatty materials vary greatly depending on the amount of water present.

Frequency (MHz)	Wavelength in air (m)	Eye lens[b]		Heart muscle		Kidney		Liver		Lung	
		ε_r	σ	ε_r	σ	ε_r	σ	ε_r	σ	ε_r	σ
10	30.0	100[c]	0.38[c]			220[d]	0.88[g]	143[d]	0.88[d]		0.67[e]
25	12.0	65[c]	0.4[c]			200	1.0[d]	137	0.51		
50	6.00	60[c]	0.4[c]			126	0.9	91	0.55		0.54[d]
100	3.00	48	0.4			90	1.0	78	0.59		0.71
200	1.50	40	0.4	61	0.96	62	1.11	53	0.79	35	0.63
400	0.75	34	0.4	54	1.09	54	1.18	48	0.86	35	0.71
500	0.60	33	0.4					47	0.88		
700	0.43	32	0.5	53	1.17	52	1.31	47	0.93	34	0.77
1,000	0.3	31	0.5	53[f]	1.19[f]	53[e]	1.23[e]	46	0.98	35[e]	0.73[e]
2,500	0.12	30	1.1			51[g]	2.28[g]				
3,000	0.10	30	1.3			49[g]	2.71[g]	43	2.02		
5,000	0.06	29	3.0			46[g]	5.43[g]				
8,500	0.04	28	6.7			39[g]	9.22[g]	36	6.28		
10,000	0.03	27	8.0			36[g]	11.60[g]	36[e]	6.67[e]		

[a] Values of the dielectric constant ε_r and conductivity σ are for 37°C and are adapted from Schwan (1957), unless otherwise indicated.
[b] Schwan (1958).
[c] Pauly and Schwan (1964).
[d] Schwan (1965), 20–23°C.
[e] Schwan (1963).
[f] Schwan and Li (1953).
[g] Burdette *et al.* (1980).

Figure 2.11.4: Relative dielectric constants and conductivities (S/m) for representative tissues with intermediate water content[39].

3. Materials

3.1 Electrical Conductivity Measurements

A conductivity meter named HI-2030 Edge® Hybrid Multiparameter EC Meter[96] (Fig.3.1.3), was used to measure the Sodium Chloride ($NaCl$) solutions' electrical conductivities. The HI-763100[97] potentiometric probe with a built-in temperature sensor (Fig.3.1.4), serves as the digital conductivity electrode. With this probe, we were able to do away with the necessity for an external temperature meter. The electrode probe is also a ring type with a tetrapolar configuration.

The use of a four-electrode setup in the potentiometric approach for determining electrical conductivity, offers significant experimental benefits. The four-ring electrode arrangement is more stable than two-pole amperometric probes, and the effects of electrode polarization are reduced. As a result, a far larger conductivity range may be measured than a two-electrode sensor, especially for liquid solutions.

The probe was calibrated with the HI-7030 manufacturer conductivity reference solution[98], with a value of $12,880 \mu S/cm$ at 25 degrees Celsius, before the conductivity measurements.

The following figure is providing the most important specifications of the equipment we used during the experimental procedure.

EC Range	Up to $500 mS/cm$ (absolute conductivity) *
Resolution	$0.01 \mu S/cm, 0.1 \mu S/cm, 1 \mu S/cm, 0.1 mS/cm$
Accuracy (@ $25°C$)	$\pm 1\%$ of reading (± 0.05 $\mu S/cm$) or 1 digit)
Temperature Compensation (TC) T. Coef. ($\%/°C$)	Yes, No TC (Absolute conductivity) 0.0 to 6.0% / $°C$
Temperature Reference in Celsius Degrees	$20°C$ or $25°C$
Cell Factor	Cell factor 0.01 to $9.999 cm^{-1}$ **

Figure 3.1.1: HI-2030 Edge® Hybrid Multiparameter EC Meter[39].

Body Material	PEI
Type	4 Ring
Insulator	Glass
Electrodes	Platinum
Range	0 to 200mS/cm
Temperature Sensor	Yes

Figure 3.1.2: HI-2030 Edge® Digital EC Platinum 4 Ring Electrode[39].

*The salt solutions' absolute electrical conductivities were measured. As a result, no TC was chosen.
**During conductivity measurements, the sensor's cell factor was $1cm^{-1}$.

The instruments that were used are depicted in the figures below:

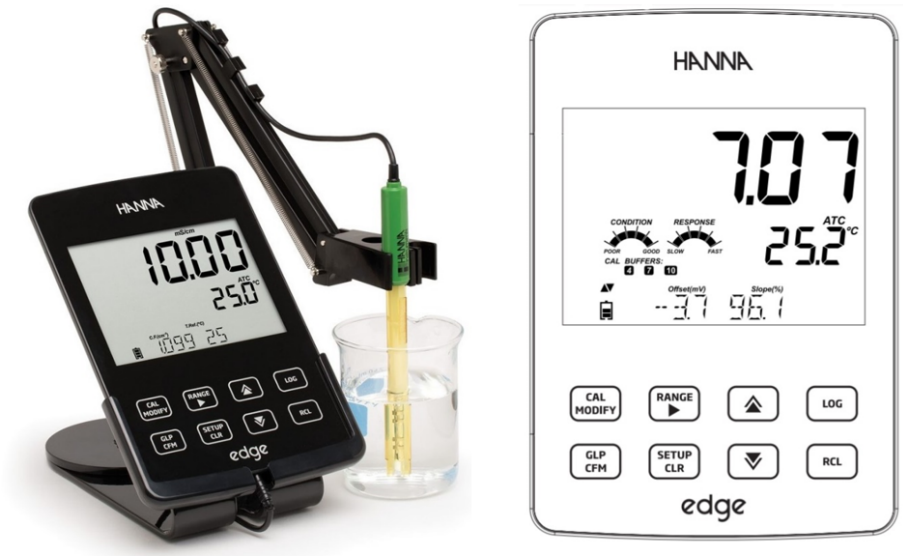

Figure 3.1.3: HI-2030 Edge® Hybrid Multiparameter EC Meter[96].

Figure 3.1.4: HI-2030 Edge® Digital EC Platinum 4 Ring Electrode[97].

3.2 Mass Measurement

A weighing system named KERN ARS 220-4[99] was used to measure the mass of the solute. It is a weighing tool featuring a high-quality single-cell weighing system for analytical balances.

Figure 3.2.1: KERN ARS 220-4 weighing system.[99]

Important specifications can be found in the Fig.3.2.2 below:

Readout (d)	$0.1mg$
Weighing Range (Max)	$220g$
Minimum Load	–
Verification Value	–
Verification Categories	–
Repeatability	$0.1mg$
Linearity	$\pm 0.2mg$
Recommended adjusting Weight, Not Included (class)	$200g$ $(E2)$
Minimum Piece Weight in Count Mode	$0.1mg$
Reference Quantity when Counting Parts	$1-999$
Weighing Plate, Stainless Steel $[mm]$	Ø 80
Dimensions of Housing $(W \times D \times H)$ $[mm]$	$210 \times 340 \times 345$
Dimensions of glass windshield $[mm]$	205 x 205 x 260 weighing space: 180 x 200 x 240
Net weight $[kg]$	5.9
Weight Units	$mg, g, GN, dwt, ozt, oz, lb, ct, C.M.$ $tLH, tLM, tLT, mo, Tola$
Permissible ambient conditions	$15°C$ to $25°C$
Stabilization time	3 *seconds*
Air Humidity	*Max.* 80% relative (non condensing)

Figure 3.2.2: KERN ARS 220-4 specifications.[99]

3.3 Stirring and Heating

In order to accomplish both stirring and heating of the solutions, stirring device named "ARE Hot Plate Stirrer"[100] manufactured by Velp® Scientifica, was used. The temperature (up to $370°C$) of the hot plate stirrer may be adjusted by rotating the left knob, while the stirring speed can be controlled by twisting the right one (up to $1500rpm$). The top plate is made of aluminum alloy, which ensures temperature uniformity and optimal heat transfer throughout the entire surface.

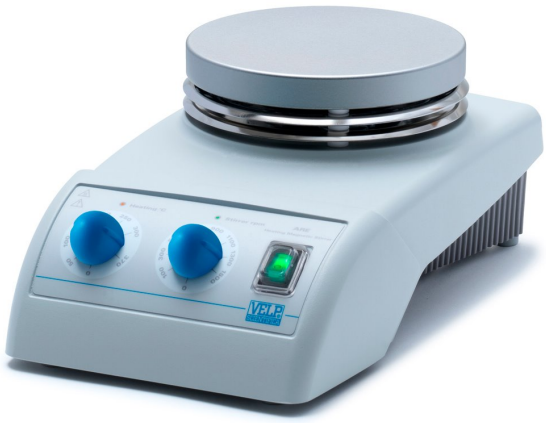

Figure 3.3.1: ARE Hot Plate Stirrer, Velp® Scientifica.[100]

Specifications about "ARE Hot Plate Stirrer" can be found in the Fig.3.3.2 below:

Construction Material	Epoxy Painted Aluminum Structure
Heating Plate Diameter	$135mm$
Power	$630W$
Dimensions (WXHXD)	$165 \times 115 \times 280\ mm$
Temperature Regulation	From Room Temp. to $370°C$
Stirring System	High – Power Driving Magnet Type "PCM" operated by a Mono-phase Motor for continuous operation
Heating Plate	Aluminum Alloy coated with Special Protection
Protection Rating CEI EN 60529	IP 42
Weight	$2.6kg$ $(5.7lb)$
Electronic Speed Control	Up to 1500 rpm
Stirring Volume	Up to 15 $Liters$
Counter – Reaction	Constant Speed

Figure 3.3.2: ARE Hot Plate Stirrer specifications.[100]

3.4 MRI System: Siemens Magnetom Sonata 1.5T

The following figures provide important Siemens Magnetom Sonata 1.5T[101] specifications.

Model	Magnetom Sonata
Magnet	Superconducting
Power Needed	
Line Voltage, VAC	380/400/420/440/480
KVa (Power Needed)	80
A/c, btu/hr (Power Needed)	10.6 kW peak
Clinical Use (Power Needed)	Whole body
Cooling Method (X-Ray Tube)	Single cryogen, 2-stage refrigeration
Cryogen Use, L/hr	
Liquid Helium (Cryogen Use, L/hr)	0.075
Magnet Weight, kg (Cryogen Use, L/hr)	4.050; 5.500 in operation
Dimensions (HXWXD), cm (Cryogen Use, L/hr)	$235 \times 215 \times 160$
Radial/Axial, m (5-Gauss Fringe Field)	2.5/4
Spectroscopy (Gradient Subsystem)	SVS or CSI optional

Figure 3.4.1: Siemens Magnetom Sonata 1.5T[101] specifications, 1.

IMAGING	
Pulse Sequences (IMAGING)	GRE, IR, FIR, STIR, TrueIR/FISP, FSE, FLAIR, MT, SS-FSE, MT-SE, MTC, MSE, EPI, 3-D: DESS/CISS/ PSIF, GMR, fat/water sat/exc, others
Repetition Time, msec (IMAGING)	1.5 @ 256×256
Echo Time, msec (IMAGING)	0.58 @ 256×256
Inversion Time, msec (IMAGING)	22
Slice Thickness, mm (GANTRY)	$0.1 - 200.0$ (2-D), $0.05 - 20.0$ (3-D)
Fov, cm (IMAGING)	$0.5 - 40.0$
Fov Offsets (IMAGING)	± 20
Scan Orientations (IMAGING)	Orthogonal (x, y, z); oblique second compound
Measuring Matrix (IMAGING)	64×64 to 1024×1024
Display Matrix (IMAGE DISPLAY)	1024×1024 full screen
Resolution, mm (PERFORMANCE)	0.01 in plane

Figure 3.4.2: Siemens Magnetom Sonata 1.5T[101] specifications, 2.

GRADIENT SUBSYSTEM	
Strength, mt/m (Gradient Subsystem)	45
Rise Time (Gradient Subsystem)	200 μsec
Slow Rate	200 T/m/sec
Memory Size, mb (Gradient Subsystem)	72 GB HD, 2 GB RAM
Array Processor (External Beam)	Dual Pentium IV
Memory Size, mb (Gradient Subsystem)	5×18 GB, 1GB RAMa
Storage media/size (Gradient Subsystem)	CD-ROM
Image Storage Capacity (Gradient Subsystem)	Approx. 5,000
Respiratory Gating (Display)	Yes
Imaging Models	
Single (Eyepiece)	Yes
Multislice (Imaging Modes)	Yes
Volume Study (Imaging Modes)	Yes
Additional (Alarms, high/low)	Multiangle, multioblique

Figure 3.4.3: Siemens Magnetom Sonata 1.5T[101] specifications, 3.

Shimming (Cryogen Use, L/hr)	Passive, active; 1st order; opt 2nd order
Body Coil (Diameter, *cm*)	60
Head Coil (Diameter, *cm*)	26 ID, Open Sides
Cardiac Gating	
Ecg/Peripheral (CARDIAC GATING)	Yes/Yes
Options	Whole-body integrated panoramic array, applications packages: advanced cardiac, diff/perf, pMRI
Bore Features (Diameter, *cm*)	Lights, Ventilation, Nurse Call, Intercom

Figure 3.4.4: Siemens Magnetom Sonata 1.5T[101] specifications, 4.

Reconstruction time	
Single Slice [*sec*]	0.056@ full 256 x 256
Multislice, [*sec*]	0.056/slice @ full 256 x 256
Volume, [*sec*]	0.056/slice @ full 256 x 256
DICOM 3.0 COMPATIBLE (Power Needed, VAC)	Yes
Angiography	Yes
Echo Planar Imaging (Cardiac Gating)	Optional package
Electromagnetic Field Strength (5-Gauss Fringe Field)	1.5 T
Configuration	Compact, open sides
Other Attributes (Interference compensation)	3-D shim; IPP/ panoramic table; 3-D MIP/MPR/SSD; remote diagnostics; Syngo/MRease; dynamic analysis;
FDA Clearance (Interference compensation)	Yes
CE Mark (MDD) (Interference compensation)	Yes
Marketing Region (Interference compensation)	Worldwide

Figure 3.4.5: Siemens Magnetom Sonata 1.5T[101] specifications, 5.

Figure 3.4.6: The Siemens Magnetom Sonata 1.5T MRI[101] Scanner.

3.5 Temperature Measurement

To perform real-time temperature measurements of the solutions during heating, a fiber optic thermometry system (m3300 Biomedical Lab Kit Fluoroptic thermometer)[102] was used. A m3300 biomedical lab kit device, a Fluoroptic probe and a fiber optic extension cable compose the whole system. The different components of the Fluoroptic system are displayed and described separately below.

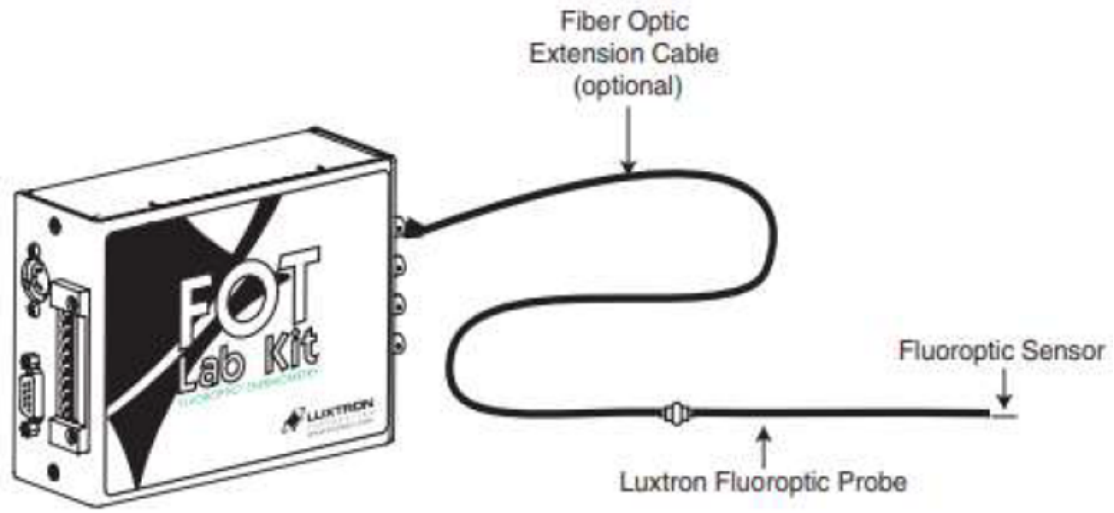

Figure 3.5.1: Fluoroptic Thermometry system: It consists of an m3300 Biomedical Lab Kit, fiber-optic extension Cables and Fluoroptic Temperature Probe.[102]

The m3300 Biomedical Lab Kit, is a four-channel fluoroptic thermometer that is entirely enclosed in steel. Over a temperature range of approximately $0°C$ to $120°C$, the instrument has an accuracy better than $0.2°C$. The instrument, also, includes 0 to $10Volt$ analog outputs for each measurement channel and uses an $RS-232$ serial interface, connected to PC, commanding input and output data.

TrueTemp software, which is compatible with Windows, was used to access the user interface. This device, in particular, is a Luxtron instrument data capture, display, and analysis software that allows the user to monitor up to four temperature probes. Important specifications of this component are given in the following figure:

Channels	4
Measurement Range	$0°C$ to $120°C$
Electrical Interference	Immune to MR, EMI, RF and microwave
Accuracy	$\pm 0.2°C$ within $\pm 20°C$ of Calibration Point $\pm 0.5°C$ within $\pm 50°C$ of Calibration Point
Standard Default Calibration	1% of full scale
Repeatability	$\pm 0.5°C$ RMS at 8 samples per measurement
Analog Output Resolution	$0.01°C$
Measurement Rate	$1Hz$ to $4Hz$ per active channel
Output Format	Selectable; $°C, K$ and $°F$
Self-Diagnostic	Self-Diagnosis and Probe Errors available on $RS-232$
Input Power	Universal power supply (Input $85-264$ VAC, $49Hz-63Hz$)
Serial Output	RS-232 serial interface at 9600 bps
Analog Output	$0-10$ VDC
Dimensions	$184mm \times 144mm \times 51mm$
Storage Temperature	$-55°C$ to $+75°C$
Operating Environment	$10°C$ to $40°C$

Figure 3.5.2: m3300 Biomedical Lab Kit Fluoroptic thermometer specifications.[102]

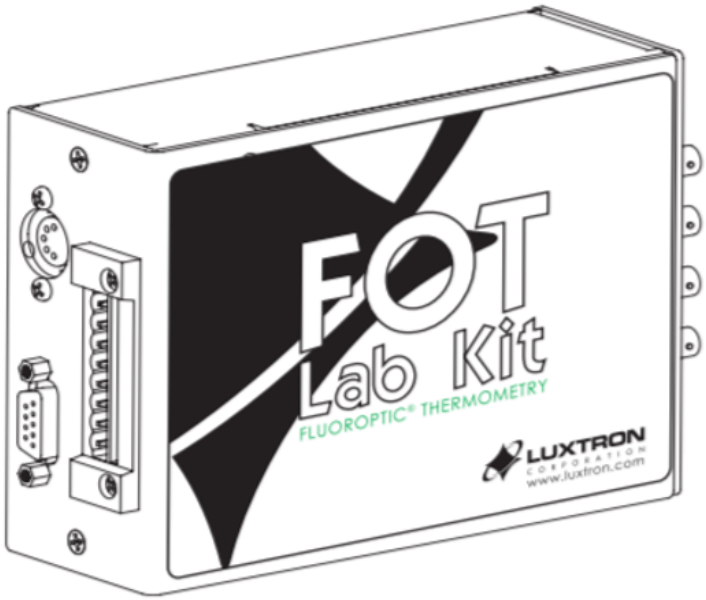

Figure 3.5.3: m3300 Biomedical Lab Kit instrument.[102]

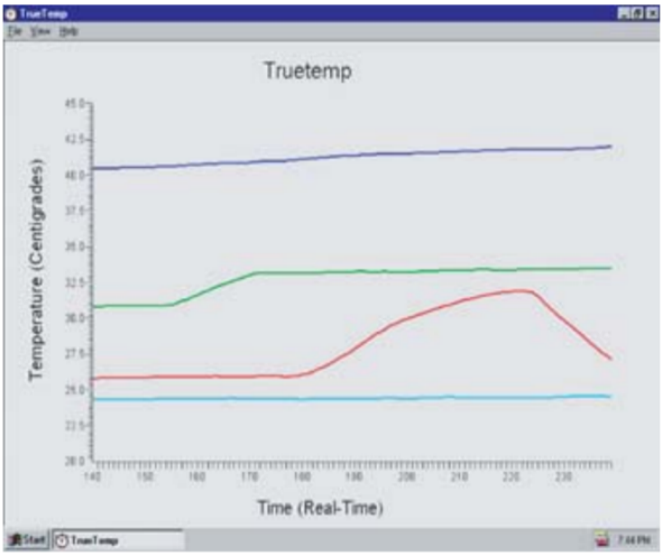

Figure 3.5.4: Luxtron TrueTemp data acquisition and graphing software.[103]

The Fluoroptic Temperature Probe (STB) is entirely composed of non-metallic materials, with a temperature-sensitive and phosphorescent sensor material in the tip. As a result, these probes are electrically non-conductive and immune to EMI and RF interference. Induction heat loss is also minimized due to the low thermal conductivity and narrow geometrical cross section of the probe. The probe tip has a diameter of $0.5mm$, and the probe's outer diameter (OD) is similarly $0.5mm$. As a result, the probes are considered minimally invasive. They're also covered in a Tefzel ethylene - tetrafluoroethylene (EFTE) fluoropolymer jacket, which allows them to be used in RF conditions.

The following Fig.3.5.5 presents the most important requirements for this component.

Tip Diameter	$0.5mm$
Jacket Diameter	$0.5mm$
Jacket Material	*Tefzel* (USP Class VI)
Temperature Range	$0°C$ to $120°C$
Response Time	0.25 seconds

Figure 3.5.5: The Fluoroptic Temperature Probe specifications.[102]

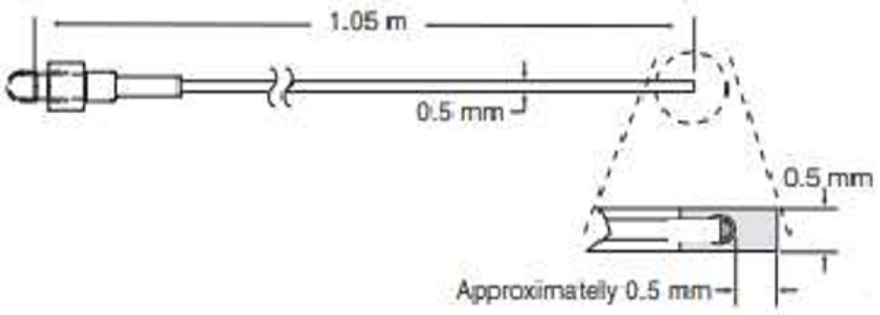

Figure 3.5.6: Standard STB Fiber optic Probe. Its length is approximately $1m$ and its diameter, Jacket diameter, is $0.5mm$.[102]

The temperature is calculated using the fluorescence of the phosphor compounds attached to the probe's end. The device emits an excitation light pulse through the fiber optic connection, which excites and fluoresces the phosphor layer. The exponentially decaying signal returns to the instrument via the same fiber optic cable after excitation. The instrument's DPS-based electronics detect and measure the fluorescence signal's decay time, shown by the symbol τ. The temperature of the sensor determines the fluorescence decay time. The instrument's electronics calculate the decay time by using multi-point digital integration of the curve. As a result, the analogue signal decays and is translated to a digital value that is directly tied to a temperature value. Subsequently, this figure is transformed to the temperature that has been calibrated.

A plot of the fluorescence intensity over time is given below:

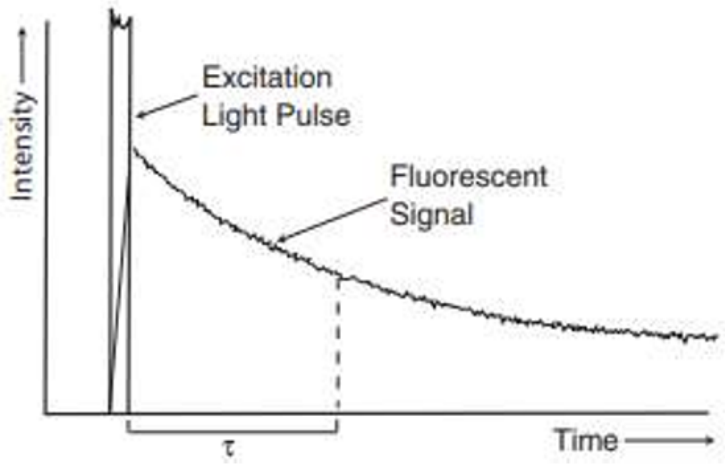

Figure 3.5.7: Fluorescence decaying signal.[103]

The dependence of the curve shape on temperature is depicted in the following plot:

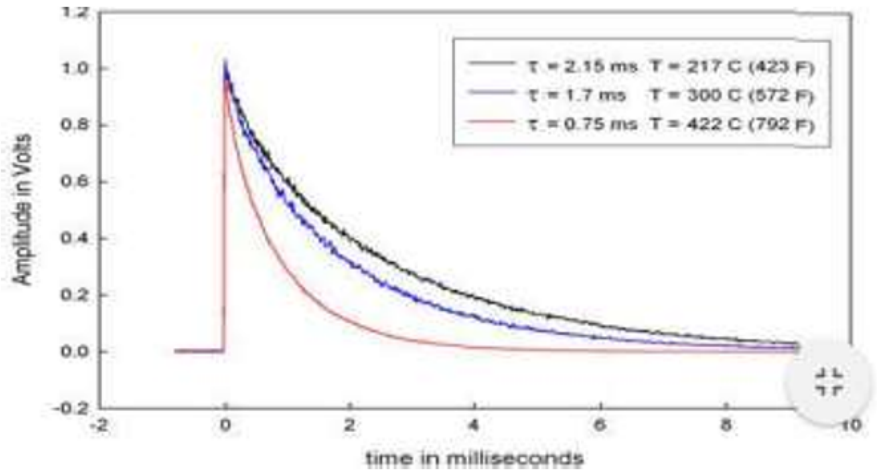

Figure 3.5.8: The decay time, τ or the shape of the curve varies with the temperature of the sensor. As temperature increases the value of τ decreases.[103]

3.6 Microwave Diathermy Machine

The device named "Fisiowave"[104] was used to increase the temperature of the solutions. Fisiowave is a high-quality microwave therapy equipment designed and manufactured by fisioline®. It is equipped with a Powerful Self-Protecting Generator (Magnetron), with pulsed and continuous emission, to achieve a peak power of $1600Watt$ and a mean power of $250Watt$.

Fisiowave's increased Peak Power provides for the administration of significant energy in depth, allowing for speedy and efficient treatments while ensuring the safety of both the patient and the operator. Fisiowave is equipped with a variety of safety measures that intervene in the case of power failure or other problem.

It considered a very functional instrument thanks to its simple set up and parameter adjustments, which are shown on a wide backlit graphic display, as well as the ease with which various antennas can be connected. A cutting-edge microcontroller manages and monitors all parameters.

Figure 3.6.1: Fisiowave, from fisioline®.[104]

Technical features and accessories are shown below:

Model	Fisiowave
Commercial Classification	Radar Therapy Equipment
Technical Classification	Class I / type B electro-medical equipment
Medical Device Class	IIb (Dir. 93/42/EEC, modified by the Dir. 2007/47/EC)
Continuous and Pulsed Emission	From 10% to 90%
Emission Frequency	$2450MHz$
Linear adjustable Power	From $0W$ to $250W$
Peak Power	$1600W$
Management with Microprocessor	
50 Pre-Memorized Therapy Protocols	
50 User Protocols	
Detachable Antenna Cable	
Automatic Temperature Control	Magnetron with Stop Emission for Overheating
Backlit Graphic Display	240×128 pixel
Timer	Adjustable from 1 to $30min$
Power Supply Voltage	230V (115V upon request)
Absorbed Power	$600VA$
Line Frequency	$(50-60)Hz$
Dimensions	$320 \times 430 \times 980$ mm
Weight	$38kg$

Figure 3.6.2: Fisiowave technical features.[104]

Standard Accessories	Optional Accessories
Circular Radiant Antenna $17cm$	Rectangular Radiant Antenna
Mechanical Arm of Support	Three-Dimensional Radiant Antenna
Antenna Cable	Protective Goggles
Test Lamp	-

Figure 3.6.3: Fisiowave accessories.[104]

4. Methods

4.1 Sodium Chloride $NaCl$ Solutions

The first purpose of this research was to measure the conductivity of $NaCl$ solutions, as a function of temperature, resembling tissues such as Fat (F), Gray Matter (GM) and Cerebrospinal Fluid (CsF).

There are few measurements of the conductivity of cerebrospinal fluid (CsF) (Crile et al., 1922[105]; Radvan Ziemnowicz et al., 1964[106]). Baumann and colleagues (1997)[107] reported a value of $1.79 S/m$ at $37°C$, which is constant in the range $10 Hz$ to $10 kHz$.

Regarding Grey Matter, most measurements yielded values between $0.161 s/m$ and $0.450 S/m$ in the frequency range of $1 - 10 kHz$ (Crile et al., 1922[105]; Freygang and Landau, 1955[108]; Ranck, 1963[109]; Van Harreveld et al., 1963[110]; Robillard and Poussart, 1977[111]). More recently, Logothetis and coworkers, 2007[112], reported an average value of $0.404 S/m$, which is practically frequency independent in the range $1 Hz$ to $10 kHz$.

It is known that Fat has a low conductivity, ranging from $0.026 S/m$ to $0.046 S/m$, with an average value of $0.036 S/m$ (Schwan and Kay, 1956[113]; Rush et al., 1963[114]; Smith and Foster, 1985[115]; Geddes and Baker, 1989[116]; Rigaud et al., 1994[117]; Gabriel et al., 1996[118]).

The following procedure was used to determine the content (in $NaCl$) of the aforementioned solutions:

Thirteen (13) $NaCl$ solutions, each with a different content (c) in mg per mL were prepared, and their conductivity (C) was measured at 37 ($°C$) degrees Celsius (Fig.4.1.1). For each solution, the amount of $NaCl$ solute (in $milligrams$) was measured using the precision weighing device, KERN ARS $220 - 4$[99] (see: 3.2 *"Mass Measurement"*). A $150 mL$ test tube was used to measure the $100 mL$ of Ultra-Pure water, which poured into each solution.

After the $100mL$ water measurements, each solute was added to the Ultra-Pure water, which acted as a solvent, then mixed until totally homogenized. The stirring process took roughly 15 minutes depending on the solution and each content of $NaCl$.

Stirring machine was also a heating device, because of its heating properties. When the solution became homogeneous, subsequently heated until it slightly surpassed $40°C$. After this process, solution was removed from the stirrer and set on the lab-bench's base (see photo with base) in order to measure the conductivity (C) at $37°C$, using the EC-meter device[96].

The conductivity measurements for each solution at $37°C$ degrees Celsius are listed in the figure beneath (Fig.4.1.1).

Number of Solution	**Concentrations**	**Conductivity**
#	$(c \pm 0.1) mgr/mL$	$(C \pm 0.01) mS/cm$
0	0.0	0.00
1	100.0	2.56
2	150.0	3.65
3	170.1	4.11
4	250.0	5.95
5	350.0	7.56
6	500.0	11.32
7	600.0	14.04
8	700.0	15.92
9	800.0	18.57
10	900.0	20.70
11	3151.4	61.70
12	10934.6	171.40

Figure 4.1.1: Thirteen $NaCl$ solutions with different contents.

The $c(C) - C$ curve was plotted after the use of data above, as well as the polynomial fit:

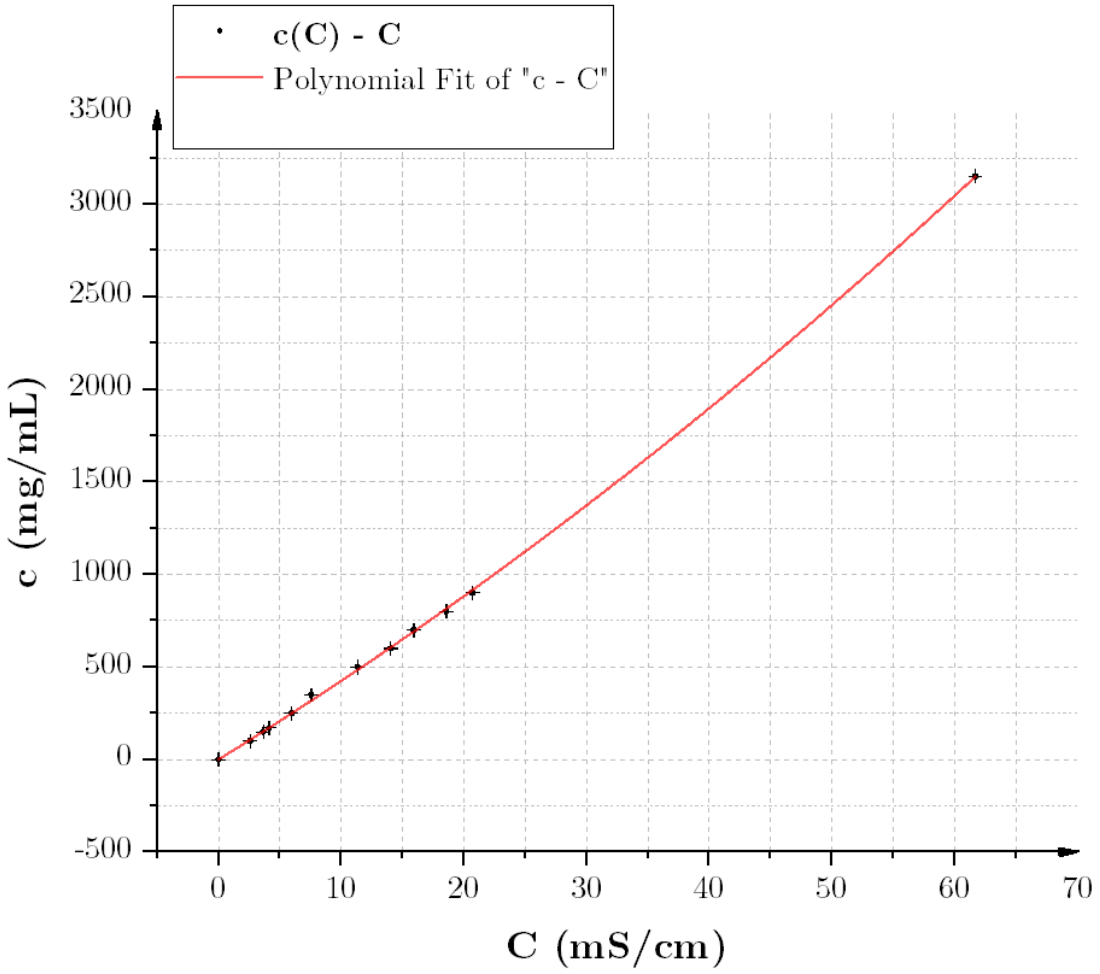

Figure 4.1.2: Polynomial Fit of $c(C) - C$.

$$c(C) = (0.1664 \pm 0.0093) \cdot C^2 + (40.781 \pm 0.495) \cdot C \qquad (4.1.1)$$

where c factor represents the content of solution and C is the conductivity.

$NaCl$ milligrams of CsF, Fat and Gray Matter simulated solutions, were calculated using the fitting equation (Eq.4.1.1) as well as the conductivity values mentioned previously in this section. In other words, reference conductivity value (C_{ref}) for each tissue was inserted in fitting equation (Eq.4.1.1), so the $NaCl$ content of each solution was estimated.

The contents of the three solutions (F, GM, CsF), as well as their measured conductivities, are listed in the figure below (Fig.4.1.3) and set at $37°C$:

Reference Temperature at $(\mathbf{37.0 \pm 0.1})°\boldsymbol{C}$		
Name of Solution	**Concentrations**	**Conductivity**
Label	$(\boldsymbol{c \pm 0.1})mgr/mL$	$(\boldsymbol{C \pm 0.01})mS/cm$
Fat	16.0	0.44
Gray Matter	167.6	4.04
Cerebrospinal Fluid	778.3	17.92

Figure 4.1.3: Contents and conductivities of each solution at $37°C$.

4.2 MRI Experiment

The three (3) solutions which were made in the laboratory, as mentioned before and a sample of Ultra - Pure water were placed in small tubes of $10ml$ each, and were placed in a base as shown in the figure below (Fig.4.2.1):

Figure 4.2.1: Placement of solutions.

The base was specially designed for the purpose of the experiment made by Teflon. Polytetrafluoroethylene (PTFE) is a synthetic fluoropolymer of tetrafluoroethylene that has numerous applications. The commonly known brand name of PTFE-based compositions is Teflon. Teflon has outstanding dielectric properties that remain stable with frequency and temperature. Some of its characteristics include: Great thermal and electrical insulation properties, low coefficient of friction and chemical resistant.

PTFE' s melting point is around $327°C$, and pure PTFE is almost totally chemically inert, highly insoluble in most solvents or chemicals, and thermally stable enough to be used between $-200°C$ and $+260°C$ without degrading.

The ending of each tube had a special recess so that the 4 fluoroptic channels could be placed inside the solutions in order to perform real time temperature measurements. This tap was a three - way stop tap with a lure lock which provided stability of fluoroptic thermometers during the experimental process.

Afterwards, the base with the four solutions was placed on the calibration plate and inside the head coil of the magnetic system.

Figure 4.2.2: Placement of the solutions inside the head coil.

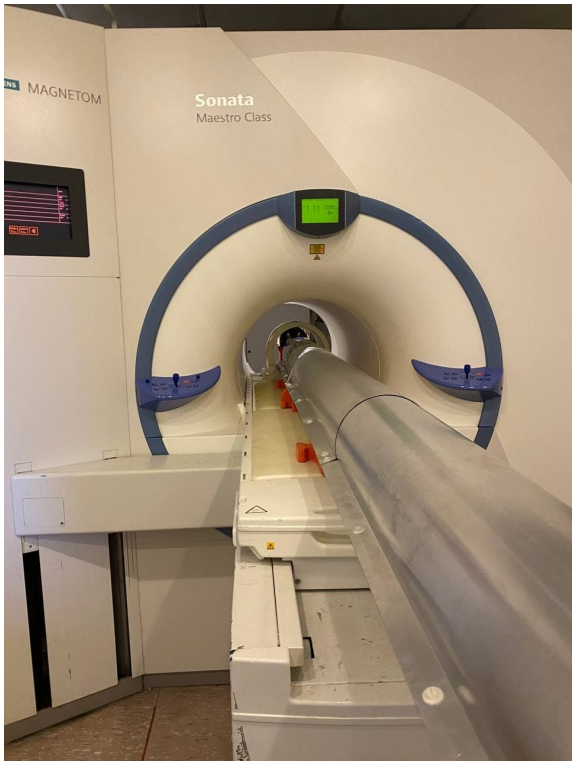

Figure 4.2.3: Waveguide placement.

The tube that was used as a waveguide was made of aluminum and stainless steel with a diameter of $18cm$. During the very first experiment a tube that was manufactured entirely by aluminum was used and it was considered to be unsuitable because of the absorption of aluminum by RF. As an outcome of this absorption the system automatically increased the power resulting in excessive noise. Stainless steel was chosen as it is a reflective material. As a result, the waveguide was chosen to be made by two different materials due to the reflectivity of stainless steel and the absorption that aluminum presented.

As a Hyperthermia system, a Microwave Diathermy device named Fisiowave was used (see 3.6). The diathermy antenna was placed in the recess of the waveguide and sent microwave pulses of 2.45GHz.

The diathermy machine was operating in continuous wave mode , sending a total of $100 - 200Watt$ with a duration of 10 minutes, each time, in order to increase the temperature of solutions until to achieve microwave hyperthermia temperatures of at least $40°C$.

Using the HASTE Sequence images were obtained after each process of heating. Throughout the experiment the temperature of the solutions was monitored real time utilizing TrueTemp software. (see section tade).

After the heating process, the conductivity of the solutions was measured using HI-2030 Edge (see section tade) from approximately $45 - 20$ degrees Celsius with natural cooling procedures.

The experimental set up is shown in the figures below:

Figure 4.2.4: Experimental design.

Figure 4.2.5: Waveguide and diathermy machine placement.

Figure 4.2.6: Diathermy machine.

Figure 4.2.7: Electrical Conductivity (EC) measurements.

Apart from the three solutions that resemble tissues, melanoma cells were also heated and measured. A375[119] is a human melanoma cell line initiated through explant culture of a solid tumor from a 54-year-old female. The cells are adherent with an epithelial morphology. Cells were maintained in complete DMEM, ie DMEM (High Glucose w/ L-Glutamine w/ Sodium Pyruvate, Cat.No L0104, Biosera, UK) supplemented with 10% (vol/vol) Fetal Bovine Serum (FBS), penicillin ($100\mu g/mL$) and streptomycin ($100\mu g/mL$). For this experiment, 26×10^6 cells were used. Exactly the same procedure was followed for heating melanoma cells, as shown in the figures below:

Figure 4.2.8: Placement of melanoma inside the head coil.

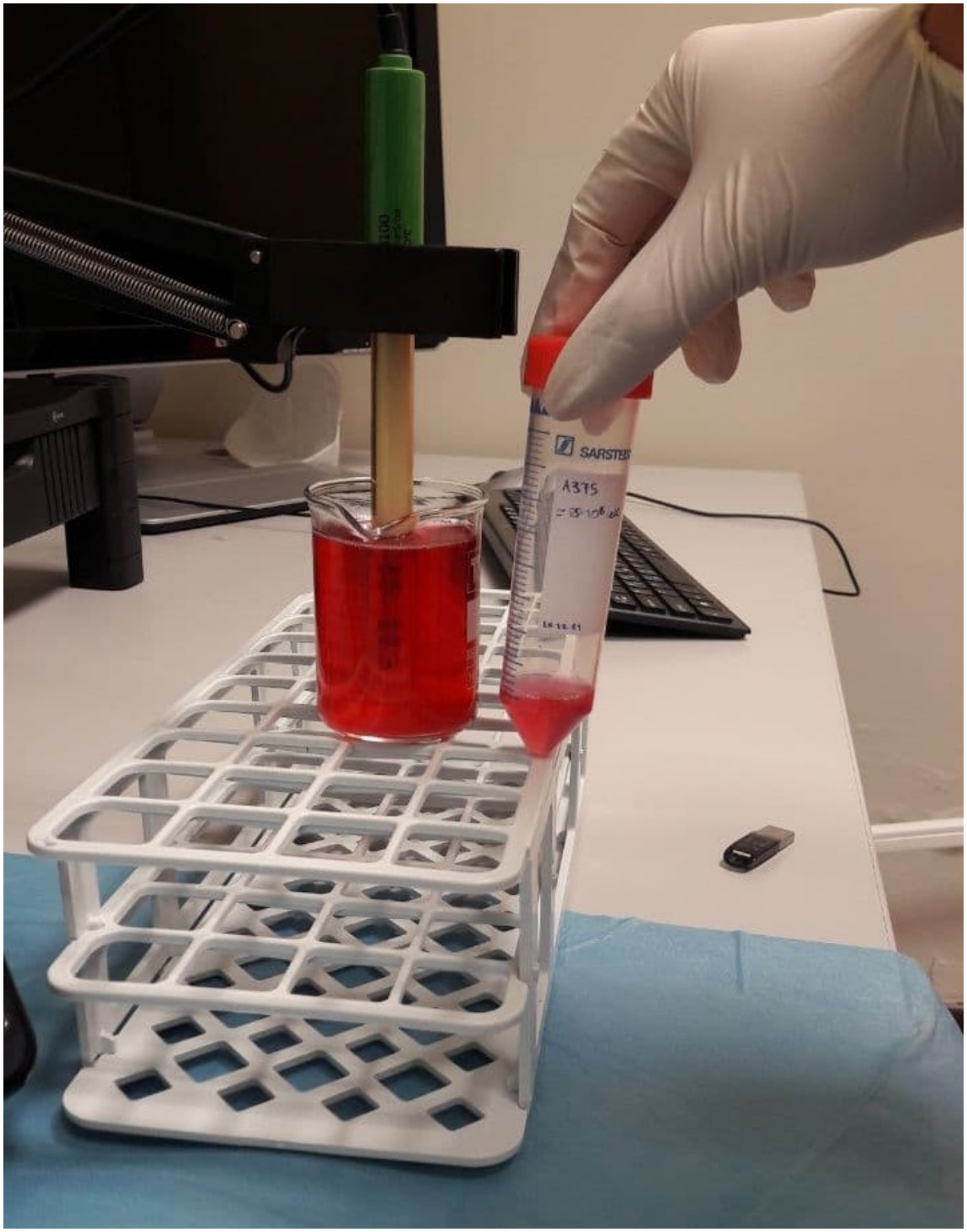

Figure 4.2.9: Electrical conductivity measurement of melanoma.

A specific research RIS/PACS platform "Evorad RIS/PACS system" was used to transfer MRI images for each temperature produced from HASTE sequences to a separate workstation through a Local Area Network (LAN). T2 color maps were calculated using advanced image post-processing methods with the assistance of an in-house image post-processing program "TESLA qMRI utilities – X" built for this purpose by Georgios Kalaitzakis and Thomas G. Maris.

A circular Region of Interest (ROI) was manually selected on each sample, and the average signal intensities inside that ROI were used to produce a single T2 value.

The standard deviation of a ROI measures the dispersion of T2 values inside that ROI around the mean. Each ROI has a unique number that correlates to a sample phantom. There were a total of five (5) ROIs. For image processing and ROI calculations, the EVORAD workstation was employed. For graphical representation of T2 values, color maps based on the "NIH" were employed.

For T2 measurements, the acceptable pixel value segmentation levels were set from 1,500ms to 3,500ms.

MedCalc[120] (Mariakerke, Belgium) software was used to handle and interpret MR parameter measurement data in order to design "$T2-T$" and "$C-T$" plots of each solution. Data was evaluated using the Kolmogorov–Smirnov method.

The "$T_i - t$", where $i = 1, 2, 3, 4$ the number of thermometers, plots of each sample were designed using plot designing program "Origin Pro[121]".

5. Results

5.1 Imaging

The T2 and T2 color parametric maps obtained from previously referenced methods. In the axial projection of the image, the first sample (starting from left) is the solution that resembles the conductivity of Cerebrospinal Fluid. The second tube resembles the conductivity of Grey Matter and the third resembles Fat. The fourth tube is filled with Ultra-Pure water.

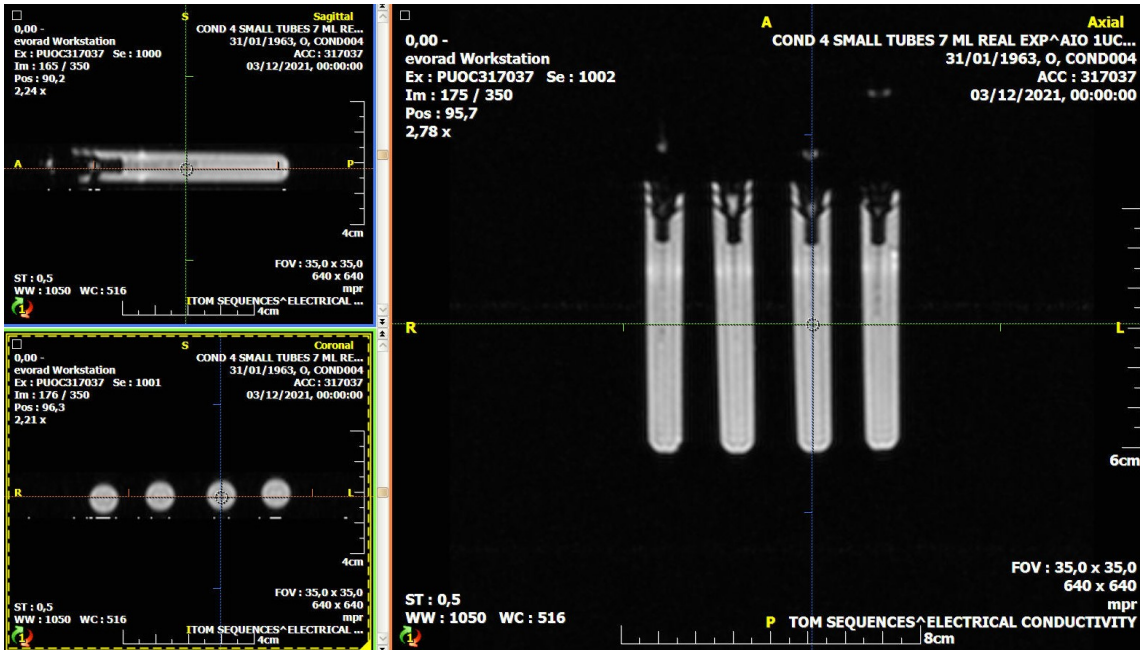

Figure 5.1.1: Saggital, Axial and Coronal MR images of four tubes containing the aforementioned solutions.

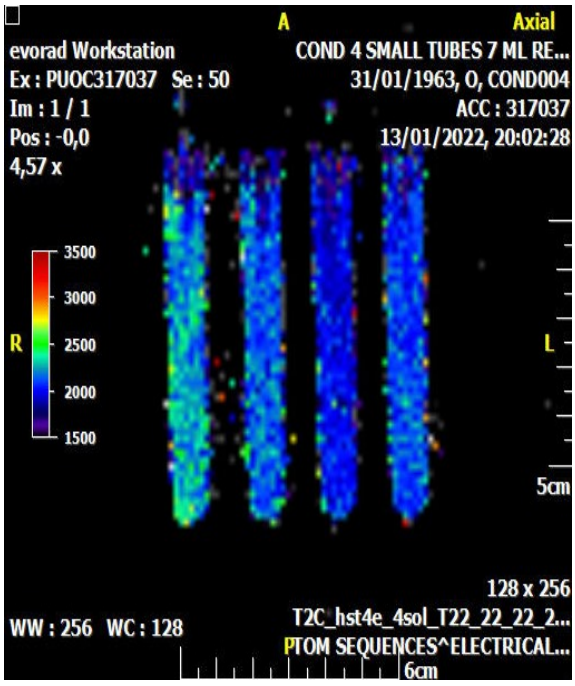

Figure 5.1.2: The $T2$ color parametric map at 22, 22, 22, 23 degrees Celsius for each solution that is resembling CsF, GM, Fat and Ultra-Pure water respectively, starting from left.

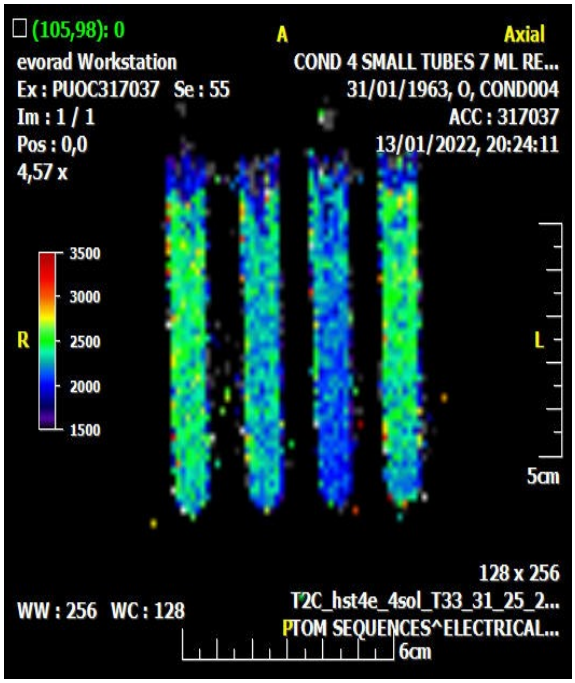

Figure 5.1.3: The $T2$ color parametric map at 33, 31, 25, 26 degrees Celsius for each solution that is resembling CsF, GM, Fat and Ultra-Pure water respectively, starting from left.

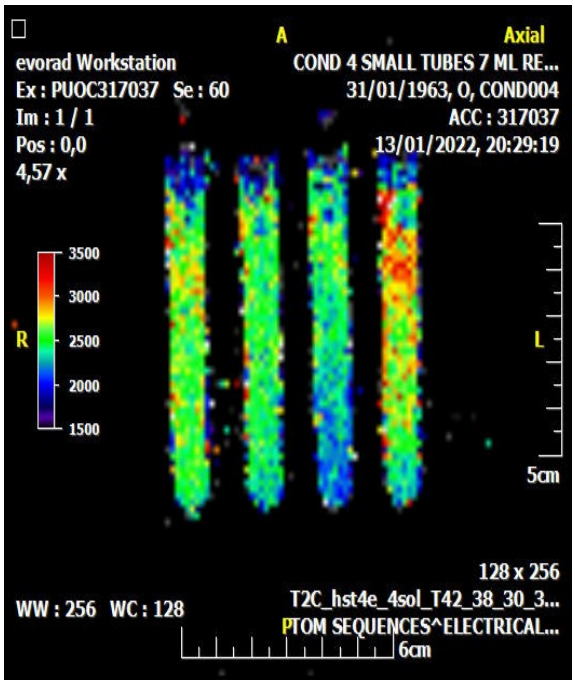

Figure 5.1.4: The $T2$ color parametric map at 42, 38, 30, 31 degrees Celsius for each solution that is resembling CsF, GM, Fat and Ultra-Pure water respectively, starting from left.

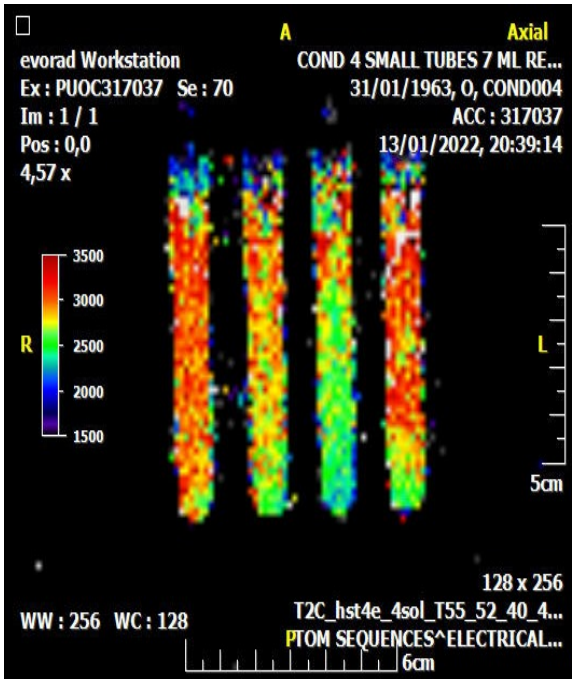

Figure 5.1.5: The $T2$ color parametric map at 55, 52, 40, 41 degrees Celsius for each solution that is resembling CsF, GM, Fat and Ultra-Pure water respectively, starting from left.

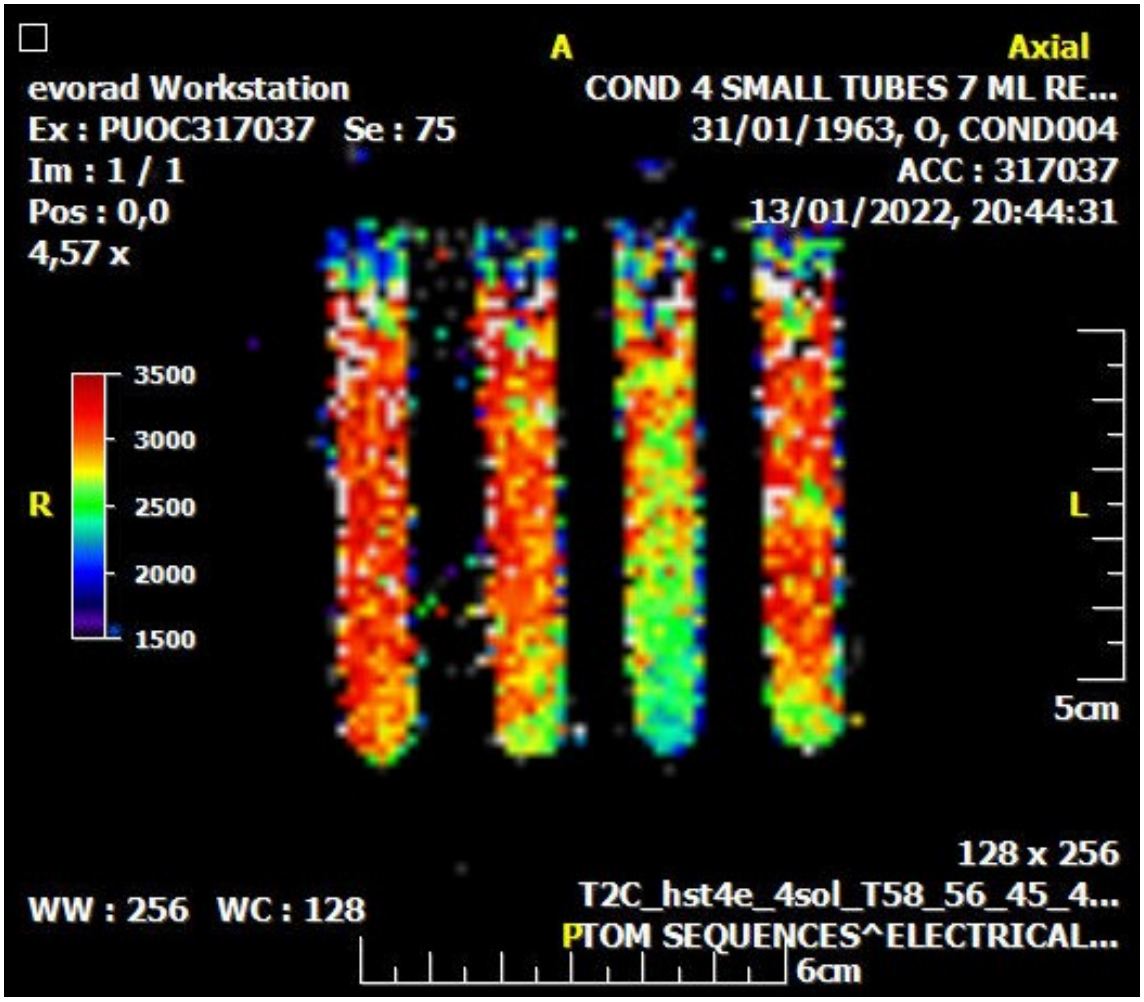

Figure 5.1.6: The $T2$ color parametric map at 58, 56, 45, 44 degrees Celsius for each solution that is resembling CsF, GM, Fat and Ultra-Pure water respectively, starting from left.

5.2 Temperature measured with TrueTemp

The "$T_i - t$", where $i = 1, 2, 3, 4$, plots of each sample were designed. The fitting curve was designed using $y(x) = ax^2 + bx + c$ function in order to approximate temperature (T) of the solutions versus time (t), when the samples were inside the MRI scanner during the heating process.

T_1 versus t and polynomial fit of $T_1 - t$:

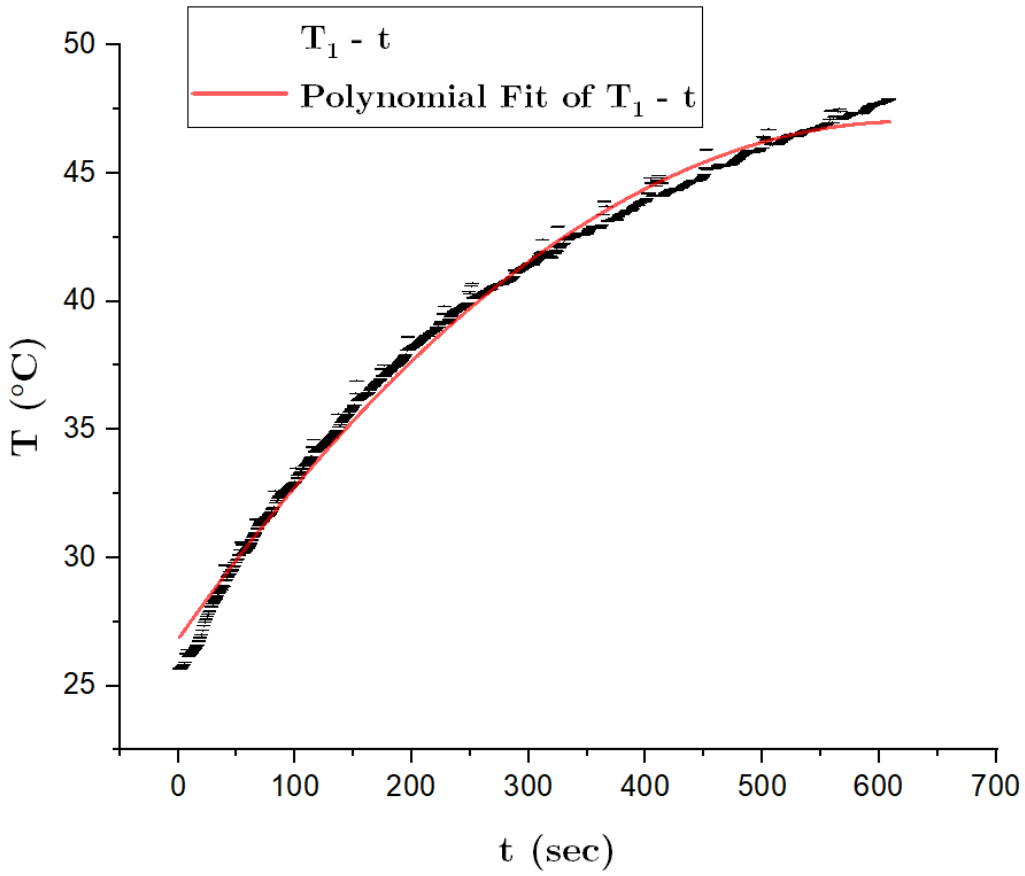

Figure 5.2.1: Polynomial Fit of $T_1 - t$.

$$T(t) = -(520 \pm 7) \cdot 10^{-7} \cdot t^2 + (65 \pm 4) \cdot 10^{-4} \cdot t + (28.820 \pm 0.056) \quad (5.2.1)$$

where T was measured in $^\circ C$ and t in sec.

T_2 versus t and polynomial fit of $T_2 - t$:

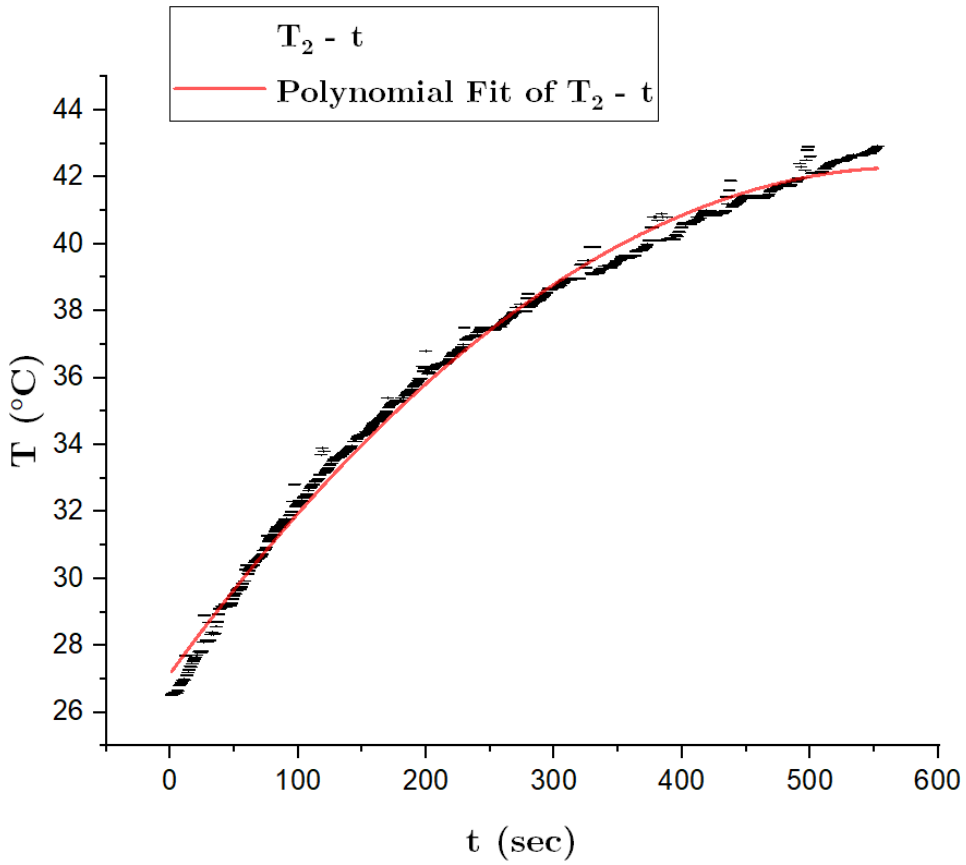

Figure 5.2.2: Polynomial Fit of $T_2 - t$.

$$T(t) = -(453 \pm 6) \cdot 10^{-7} \cdot t^2 + (52 \pm 4) \cdot 10^{-4} \cdot t + (27.171 \pm 0.044) \quad (5.2.2)$$

where T was measured in $^{\circ}C$ and t in sec.

T_3 versus t and polynomial fit of $T_3 - t$:

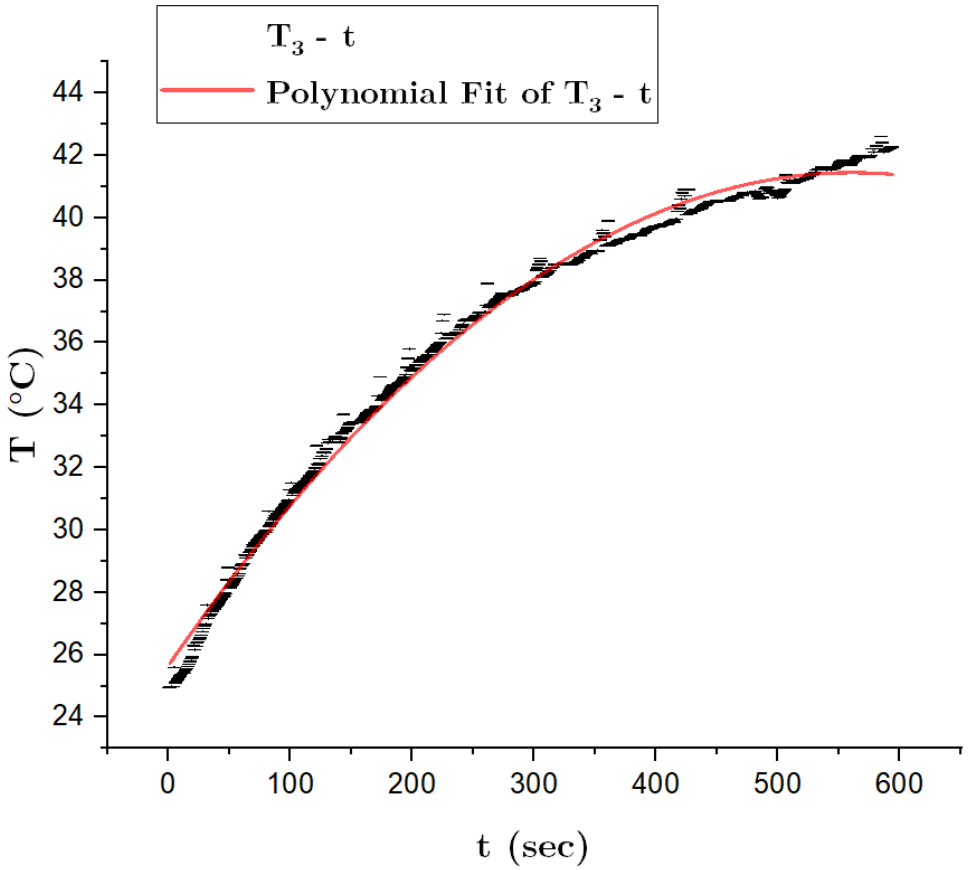

Figure 5.2.3: Polynomial Fit of $T_3 - t$.

$$T(t) = -(501 \pm 6) \cdot 10^{-7} \cdot t^2 + (56 \pm 4) \cdot 10^{-4} \cdot t + (25.662 \pm 0.047) \quad (5.2.3)$$

where T was measured in $^{\circ}C$ and t in sec.

T_4 versus t and polynomial fit of $T_4 - t$:

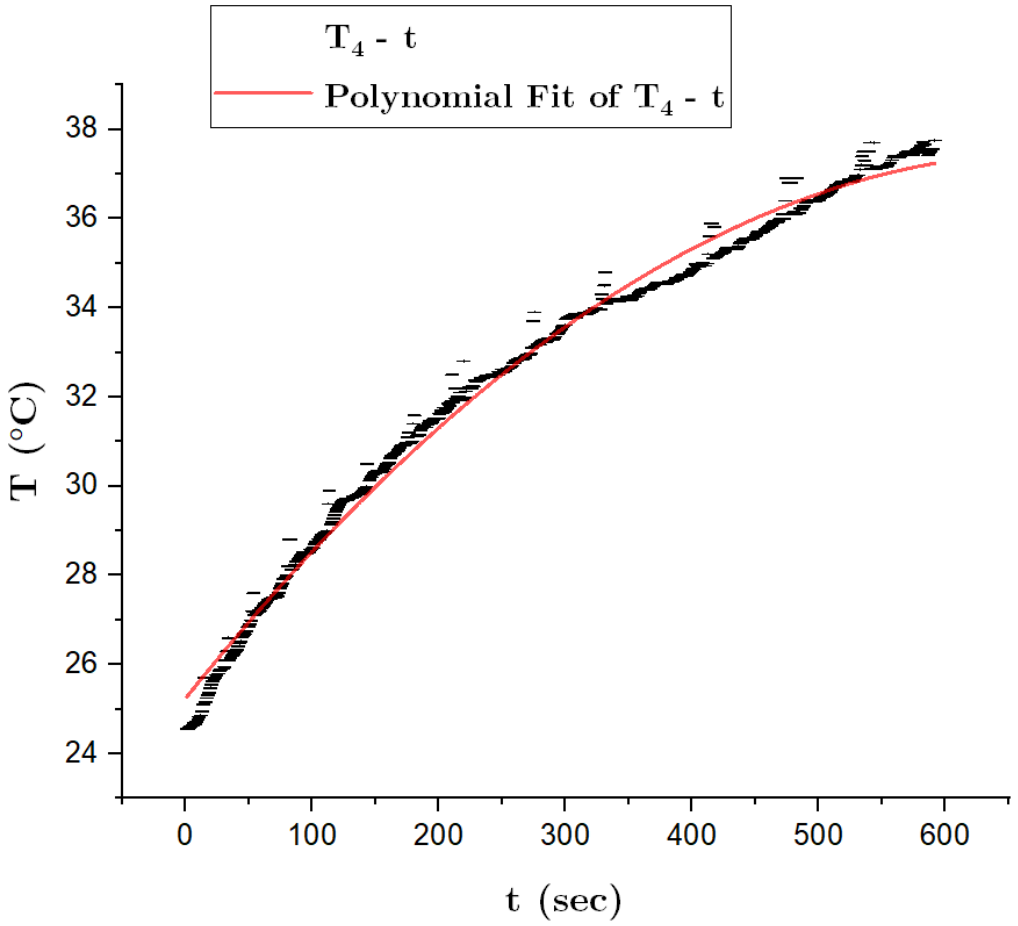

Figure 5.2.4: Polynomial Fit of $T_4 - t$.

$$T(t) = -(257 \pm 5) \cdot 10^{-7} \cdot t^2 + (35 \pm 3) \cdot 10^{-4} \cdot t + (25.24 \pm 0.041) \quad (5.2.4)$$

where T was measured in $^\circ C$ and t in sec.

5.3 MR Images of Solutions Resemble Tissues

Four ROIs were manually set for each sample as shown in the following figures. Each ROI provides a measurement of the average $T2$ relaxation time (ms) of the corresponding sample and covers an area of approximately $1.23cm^2$.

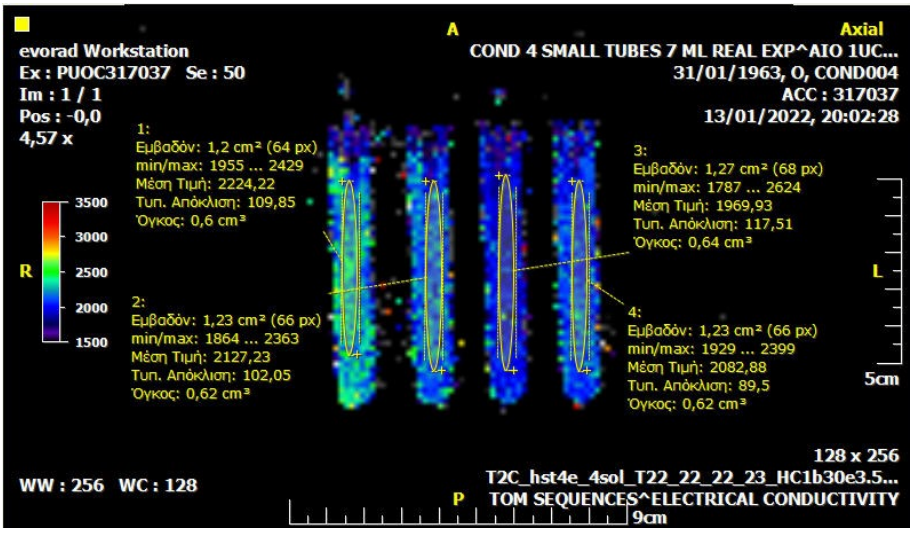

Figure 5.3.1: The $T2$ color parametric map, containing ROIs, at 22, 22, 22, 23 degrees Celsius for each solution that is resembling CsF, GM, Fat and Ultra-Pure water respectively, starting from left.

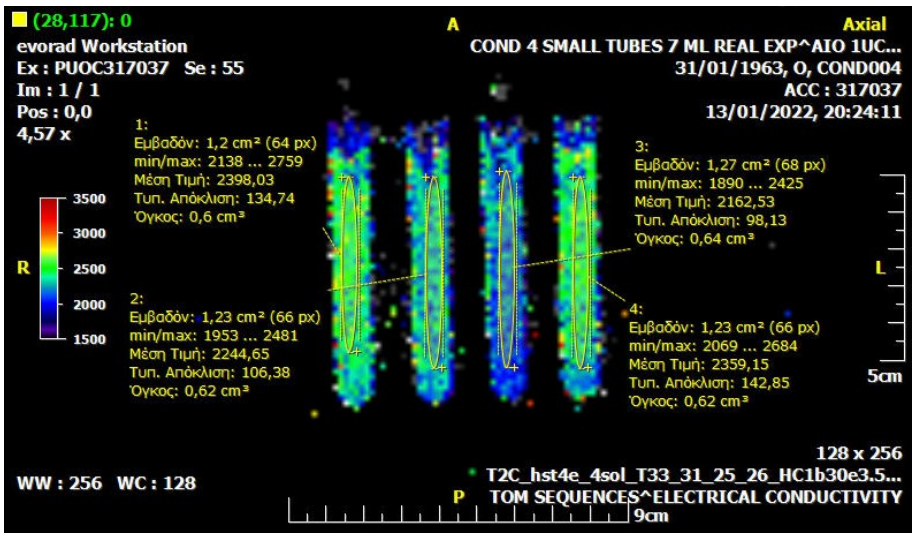

Figure 5.3.2: The $T2$ color parametric map, containing ROIs, at 33, 31, 25, 26 degrees Celsius for each solution that is resembling CsF, GM, Fat and Ultra-Pure water respectively, starting from left.

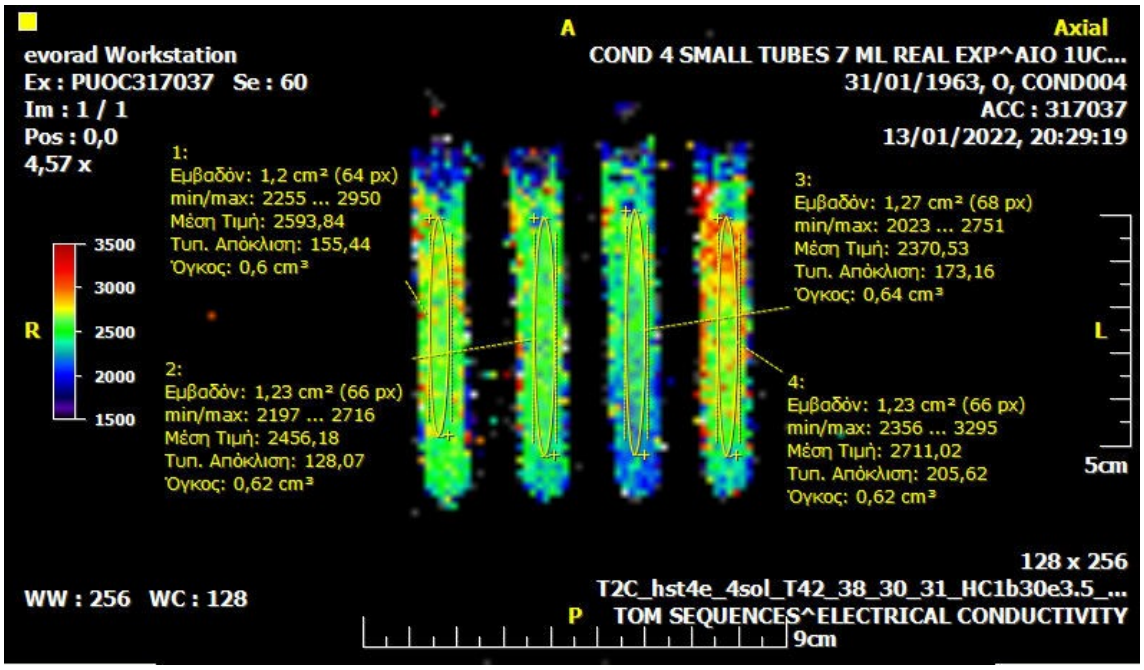

Figure 5.3.3: The $T2$ color parametric map, containing ROIs, at 42, 38, 30, 31 degrees Celsius for each solution that is resembling CsF, GM, Fat and Ultra-Pure water respectively, starting from left.

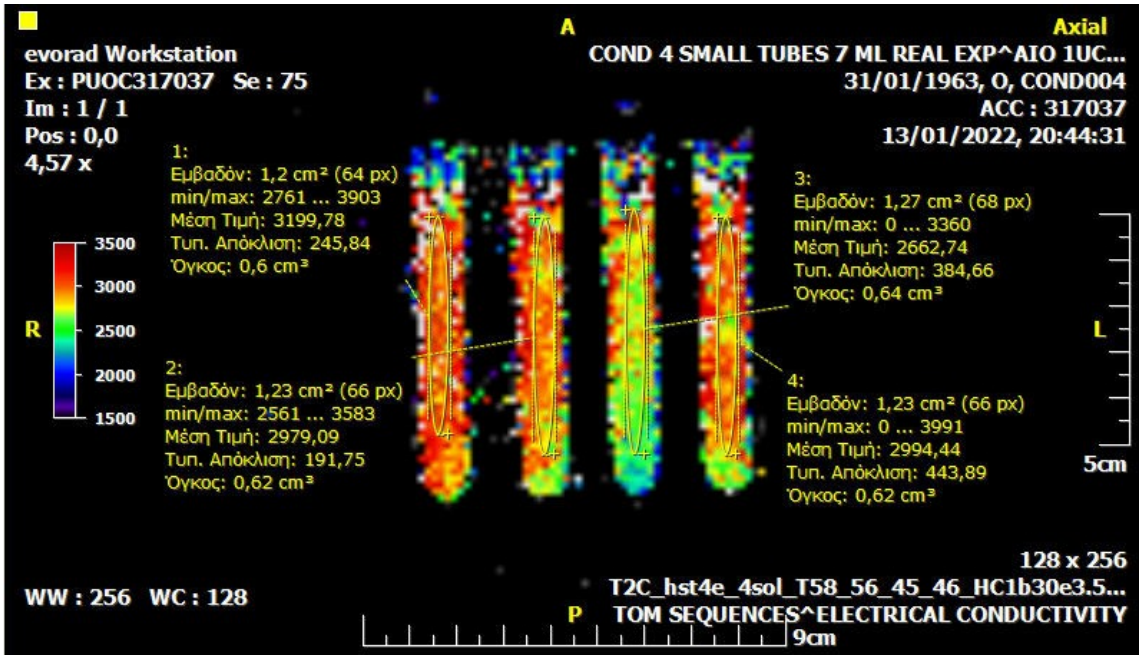

Figure 5.3.4: The $T2$ color parametric map, containing ROIs, at 58, 56, 45, 46 degrees Celsius for each solution that is resembling CsF, GM, Fat and Ultra-Pure water respectively, starting from left.

5.4 Solutions' Plots for T2 and Conductivity

The dependence of T2 on solutions was examined over a wide range of temperatures (20°C to 45°C). All of the samples' T2 values were calculated with respect of each degree of temperature. Using the HASTE sequence, separate T2 maps were constructed for each temperature.

Plotted data are presented separately for each kind of solution. Specifically, T2 values regarding different concentration of sodium chloride solution (% w/v) as a function of temperature. Each table corresponds to a different T2 mapping technique.

A linear function, $y = a \cdot x + b$, was used to approximate the $T2$ versus Temperature dependence in this study. The best fit of the data guided the choice of equation.

In the plots below, option of "Heat Map" was selected in which the background color coding indicates density of points, suggesting clusters of observations.

Furthermore, the effect of temperature on Electrical Conductivity (EC) was studied over a wide temperature range. Specifically, the EC of Sodium Chloride solutions was determined for each temperature degree. The starting temperature was $20°C$ and the maximum temperature was $45°C$.

5.4.1 Resembling Fat Solution

The $T2-T$ plot corresponds to a solution with $NaCl$ content of $16mg/mL$, which conductivity resembles Fat's at $37°C$.

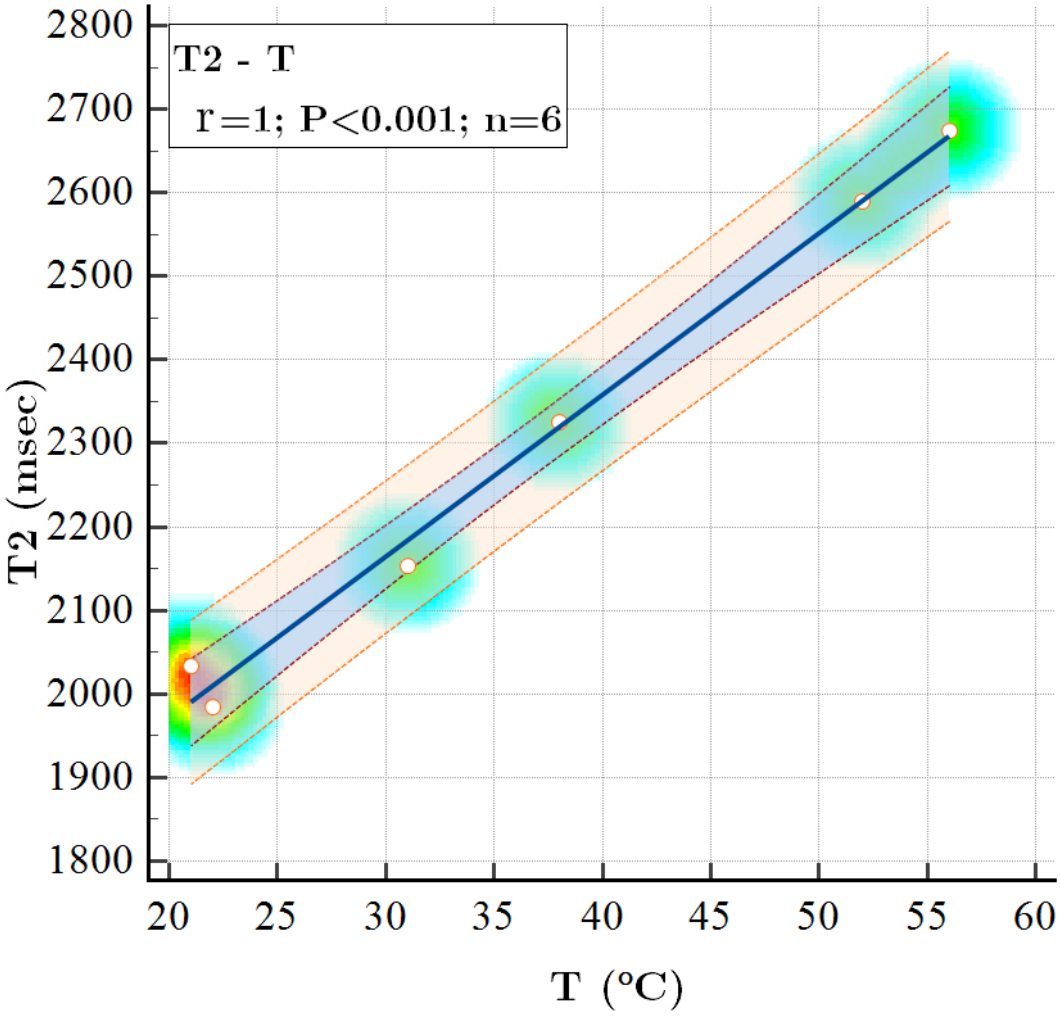

Figure 5.4.1: Linear regression for the relationship between Fat resembling solutions' $T2$ and T. The $T2$ values were obtained with HASTE sequence. The dashed brown curves represent the 95% confidence interval for the regression line. The dashed orange curves represent the 95% prediction interval for the regression curve.

$$T2(T) = (19.35 \pm 0.89) \cdot T + (1584 \pm 35) \tag{5.4.1}$$

Conductivity (C) of Fat resembling solution versus Temperature (T).

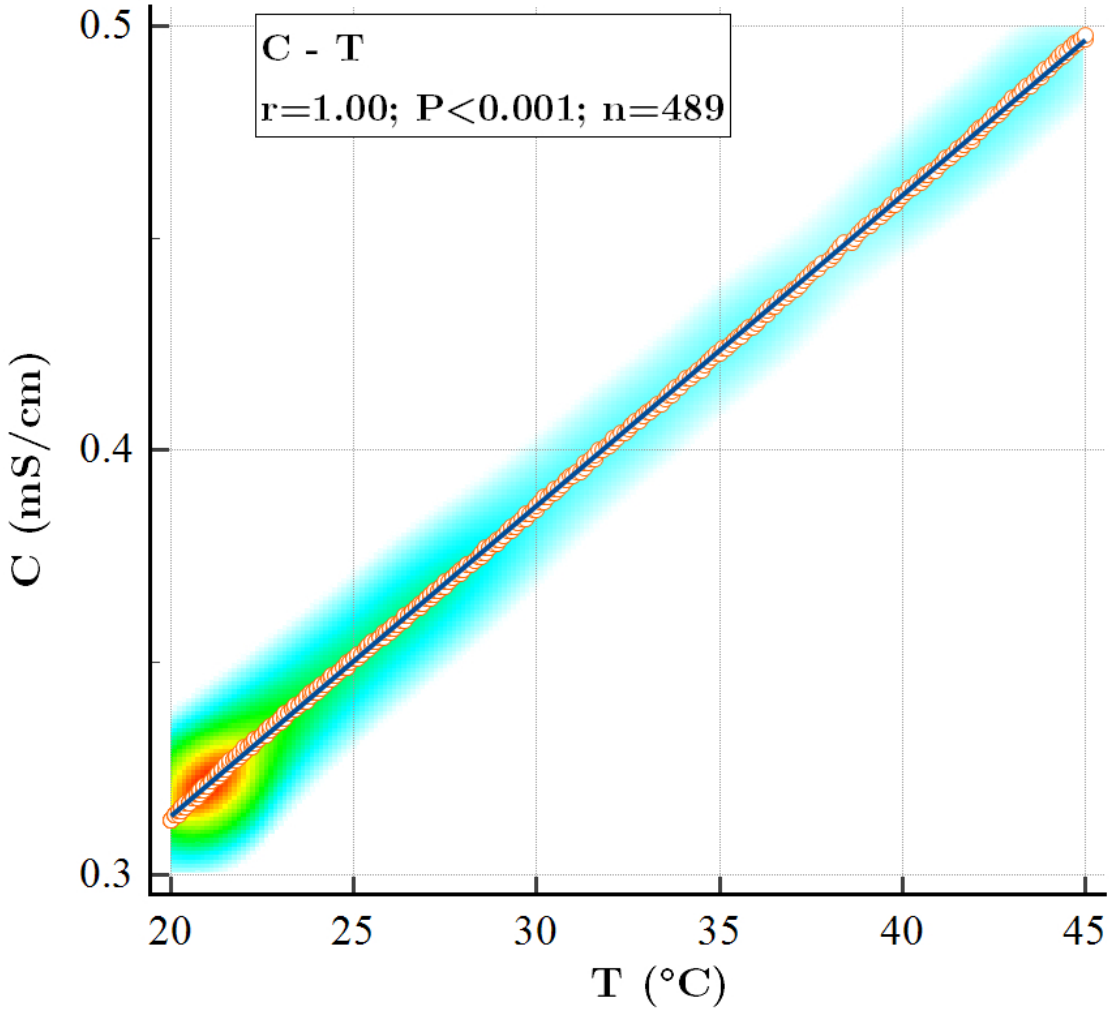

Figure 5.4.2: $C - T$ of Fat resembling solution.

$$C(T) = (0.007310 \pm 0.000004) \cdot T + (0.16761 \pm 0.00011) \qquad (5.4.2)$$

5.4.2 Resembling Grey Matter Solution

The $T2-T$ plot corresponds to a solution with $NaCl$ content of $167.6mg/mL$, which conductivity resembles Grey Matter's at $37°C$.

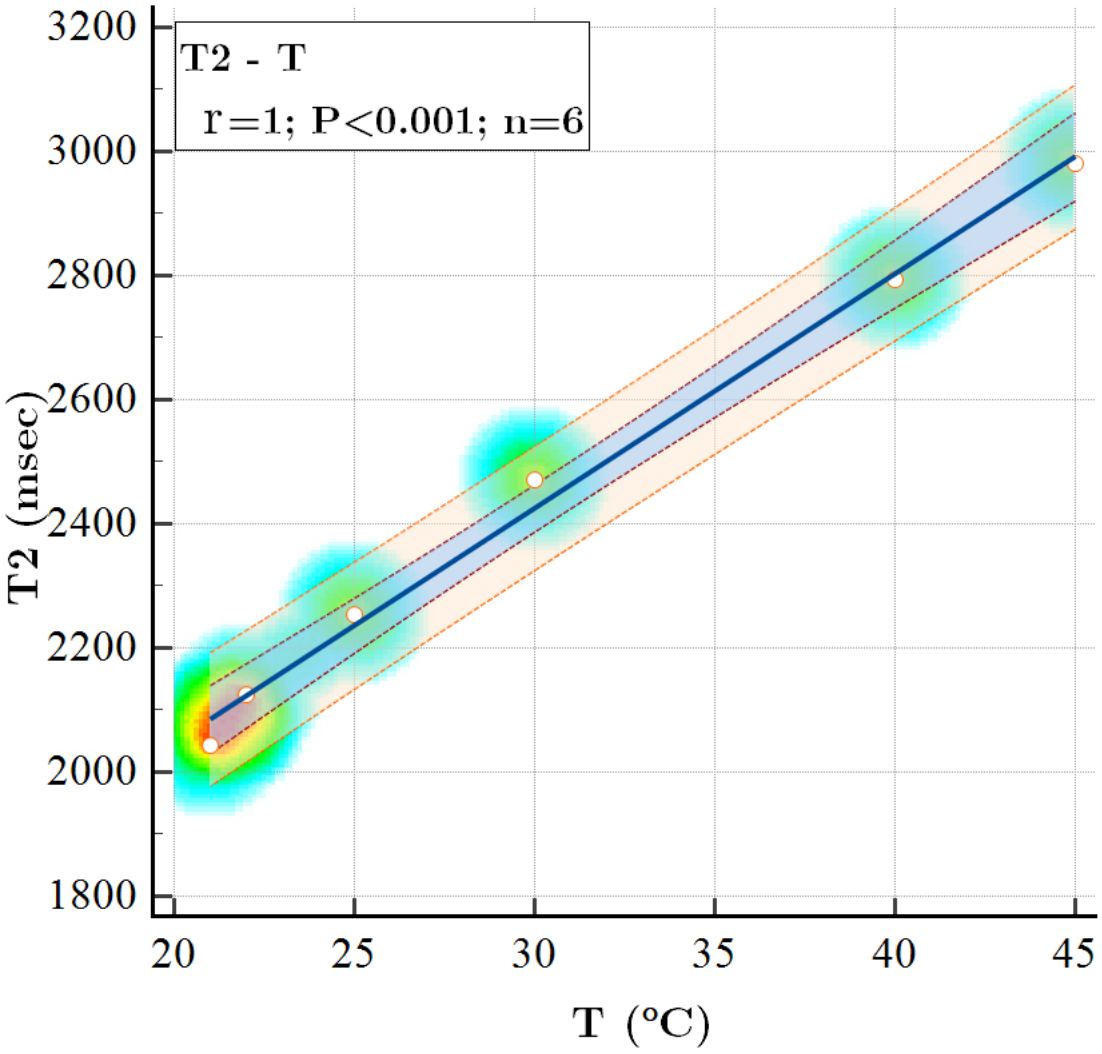

Figure 5.4.3: Linear regression for the relationship between Grey Matter resembling solutions' $T2$ and T. The $T2$ values were obtained with HASTE sequence. The dashed brown curves represent the 95% confidence interval for the regression line. The dashed orange curves represent the 95% prediction interval for the regression curve.

$$T2(T) = (37.78 \pm 1.50) \cdot T + (1292 \pm 48) \tag{5.4.3}$$

Conductivity (C) of Grey Matter resembling solution versus Temperature (T).

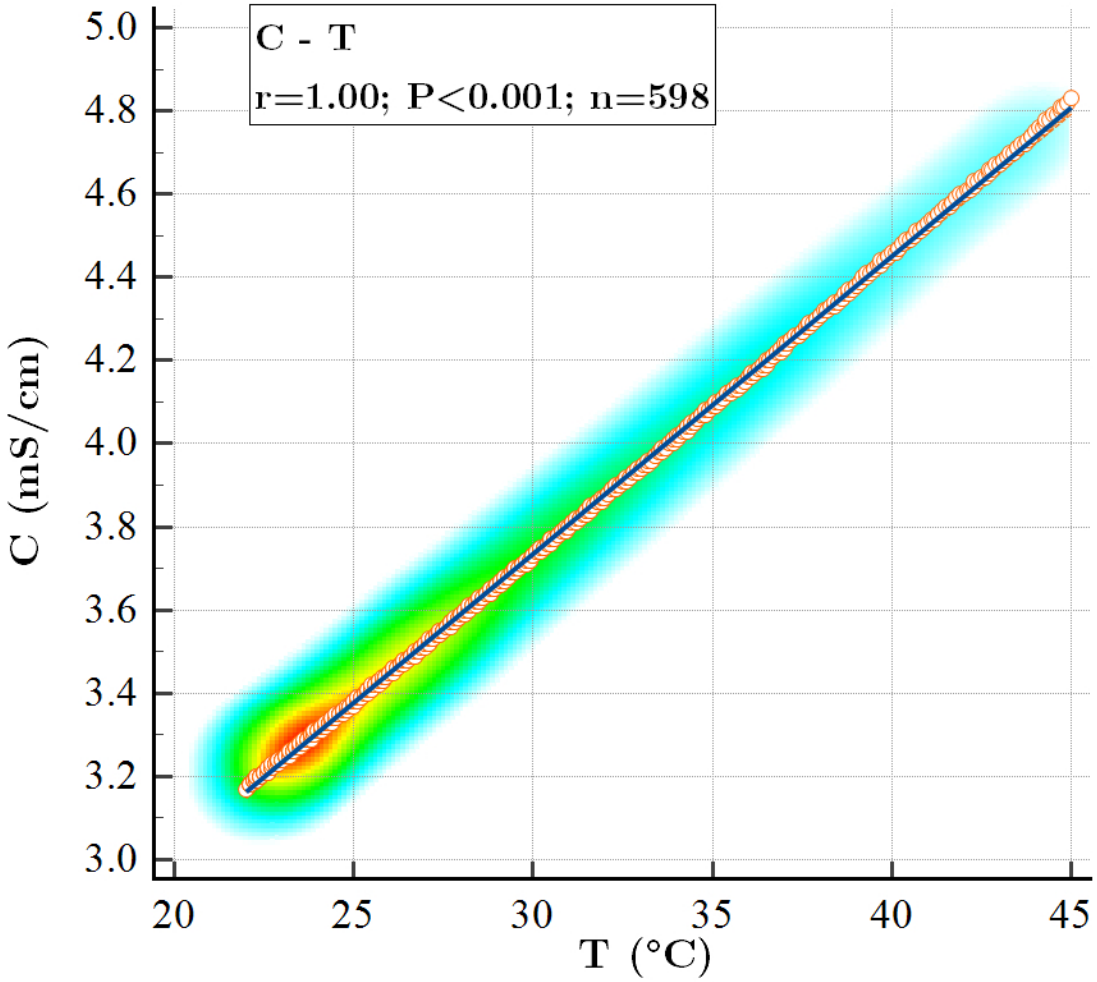

Figure 5.4.4: $C - T$ of Grey Matter resembling solution.

$$C(T) = (0.07152 \pm 0.00004) \cdot T + (1.5896 \pm 0.0014) \qquad (5.4.4)$$

5.4.3 Resembling Cerebrospinal Fluid Solution

The $T2-T$ plot corresponds to a solution with $NaCl$ content of $778.3 mg/mL$, which conductivity resembles Cerebrospinal Fluid's at $37°C$.

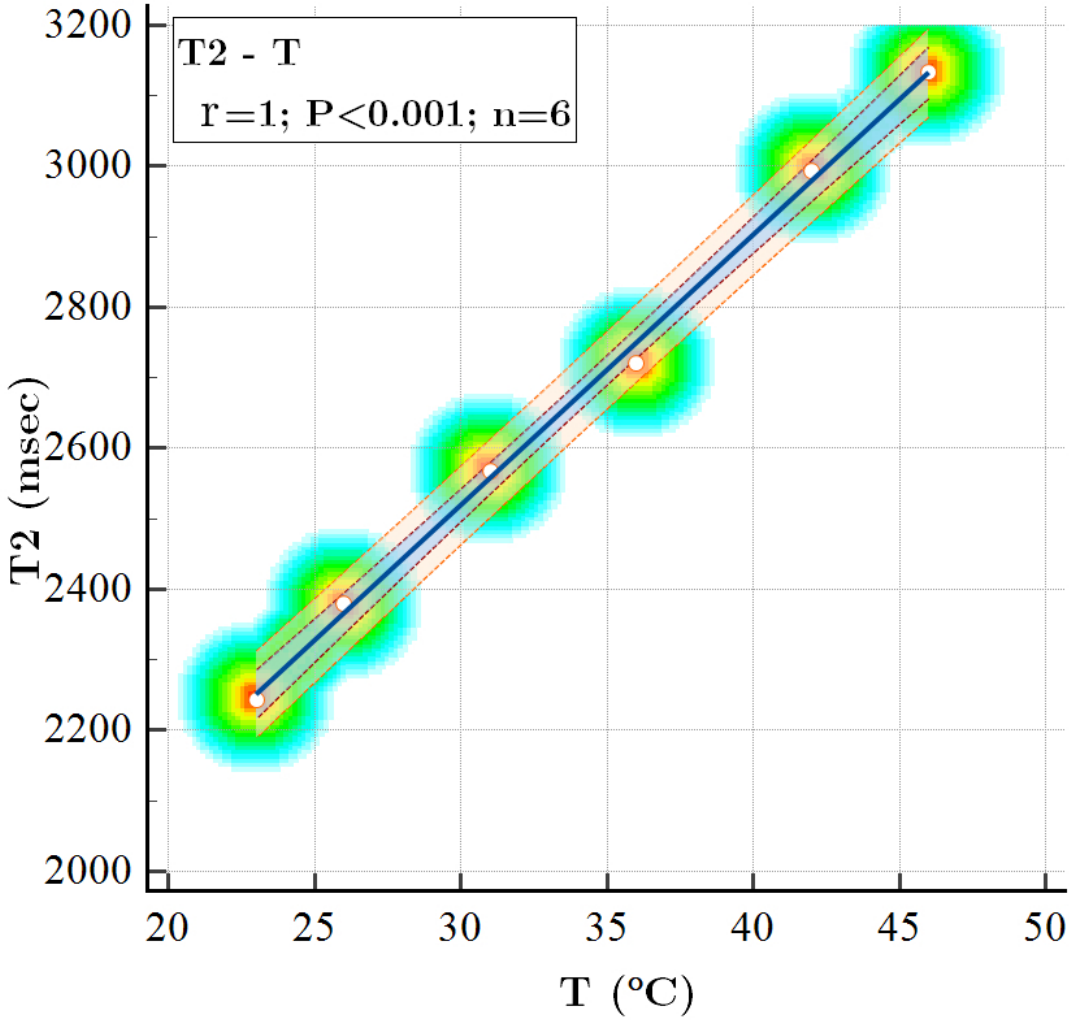

Figure 5.4.5: Linear regression for the relationship between CsF resembling solutions' $T2$ and T. The $T2$ values were obtained with HASTE sequence. The dashed brown curves represent the 95% confidence interval for the regression line. The dashed orange curves represent the 95% prediction interval for the regression curve.

$$T2(T) = (38.35 \pm 0.90) \cdot T + (1369 \pm 32) \tag{5.4.5}$$

Conductivity (C) of Cerebrospinal Fluid resembling solution versus Temperature (T).

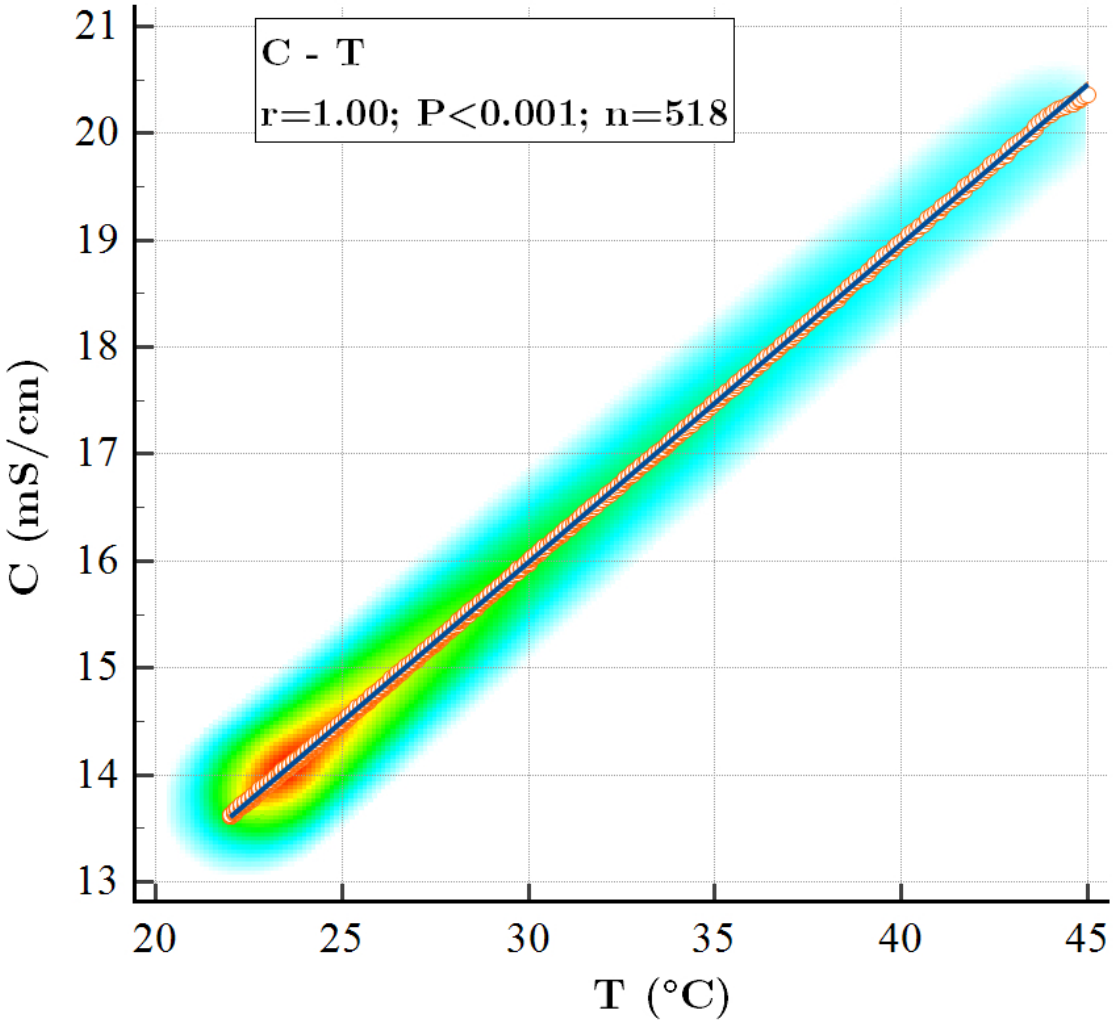

Figure 5.4.6: $C - T$ of CsF resembling solution.

$$C(T) = (0.2981 \pm 0.0001) \cdot T + (7.053 \pm 0.006) \tag{5.4.6}$$

5.5 Melanoma

5.5.1 Melanoma MR Images

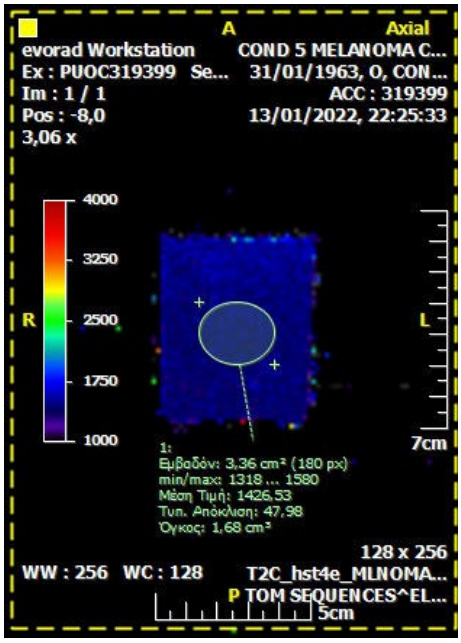

Figure 5.5.1: The $T2$ color parametric map at 20 degrees Celsius for melanoma.

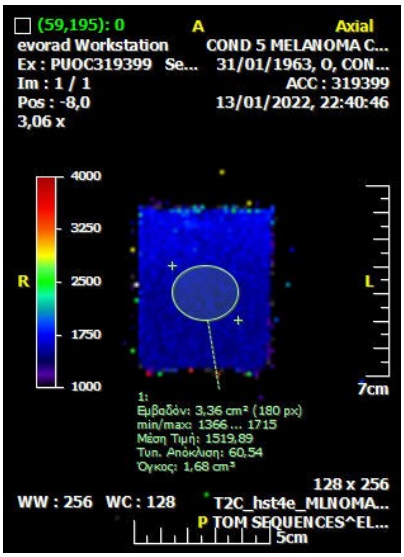

Figure 5.5.2: The $T2$ color parametric map at 26 degrees Celsius for melanoma.

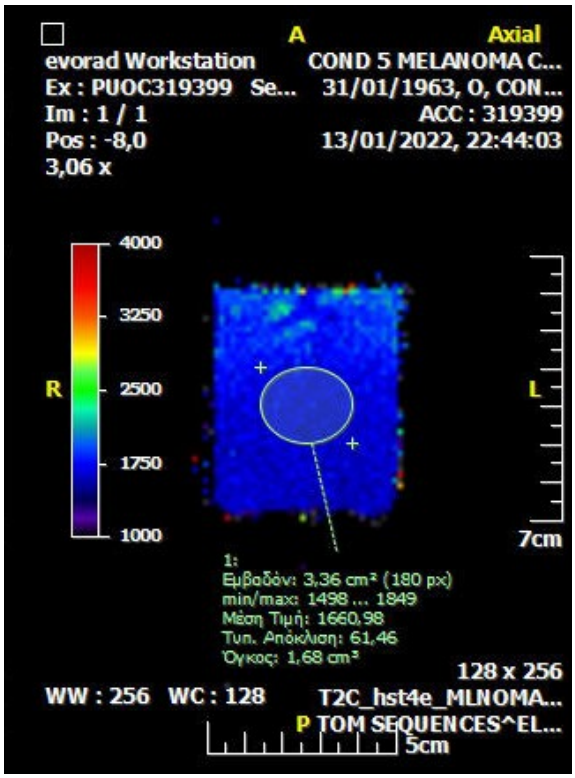

Figure 5.5.3: The $T2$ color parametric map at 32 degrees Celsius for melanoma.

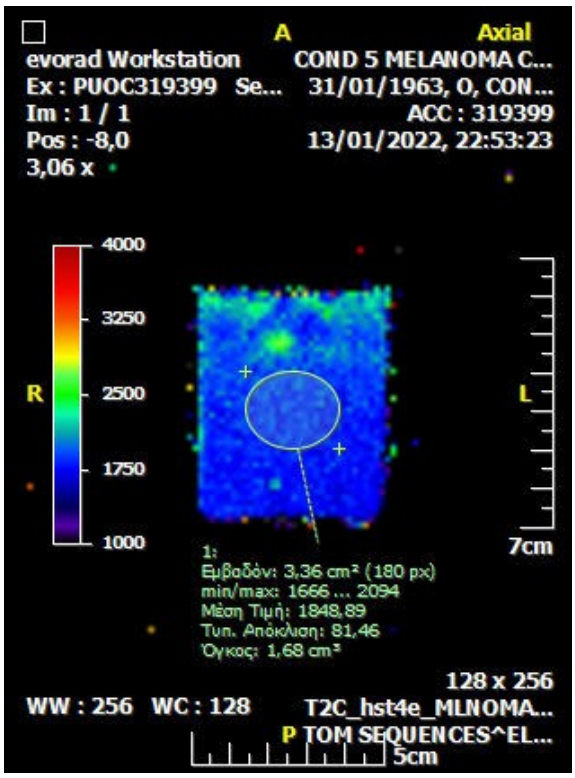

Figure 5.5.4: The $T2$ color parametric map at 38 degrees Celsius for melanoma.

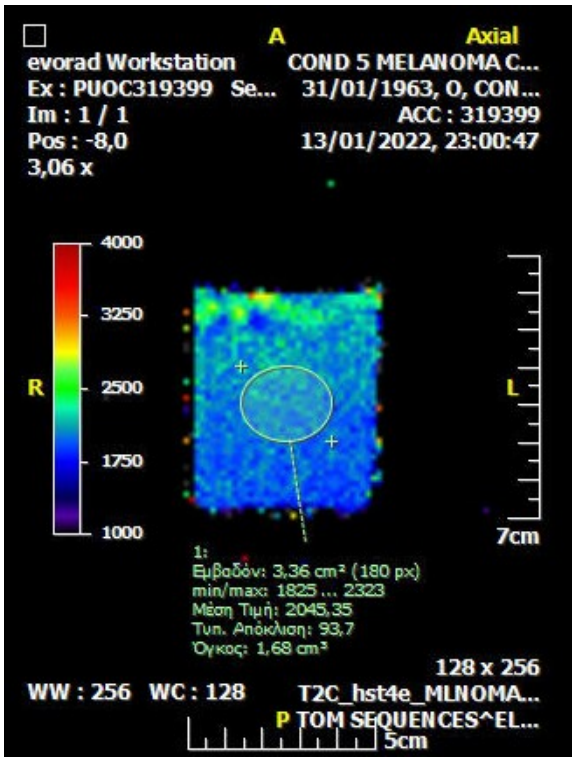

Figure 5.5.5: The $T2$ color parametric map at 43 degrees Celsius for melanoma.

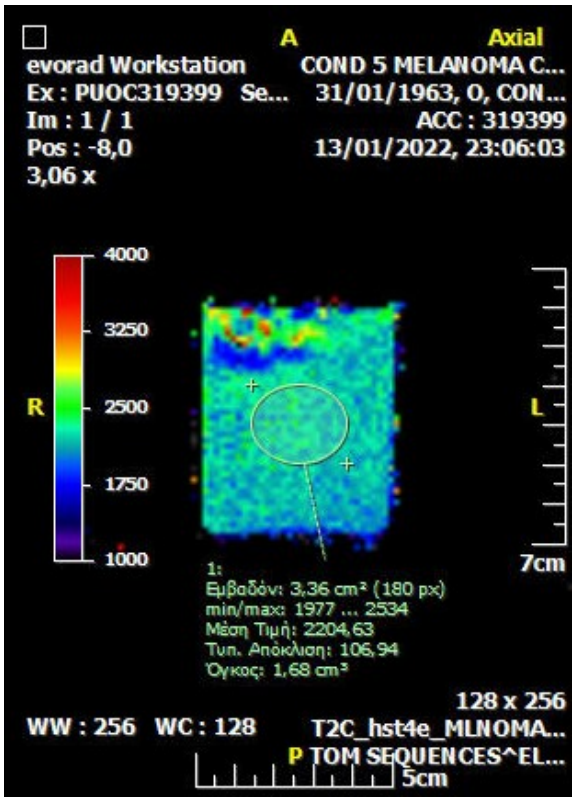

Figure 5.5.6: The $T2$ color parametric map at 48 degrees Celsius for melanoma.

5.5.2 Melanoma Plots

Melanoma $T2$ versus Temperature T plot:

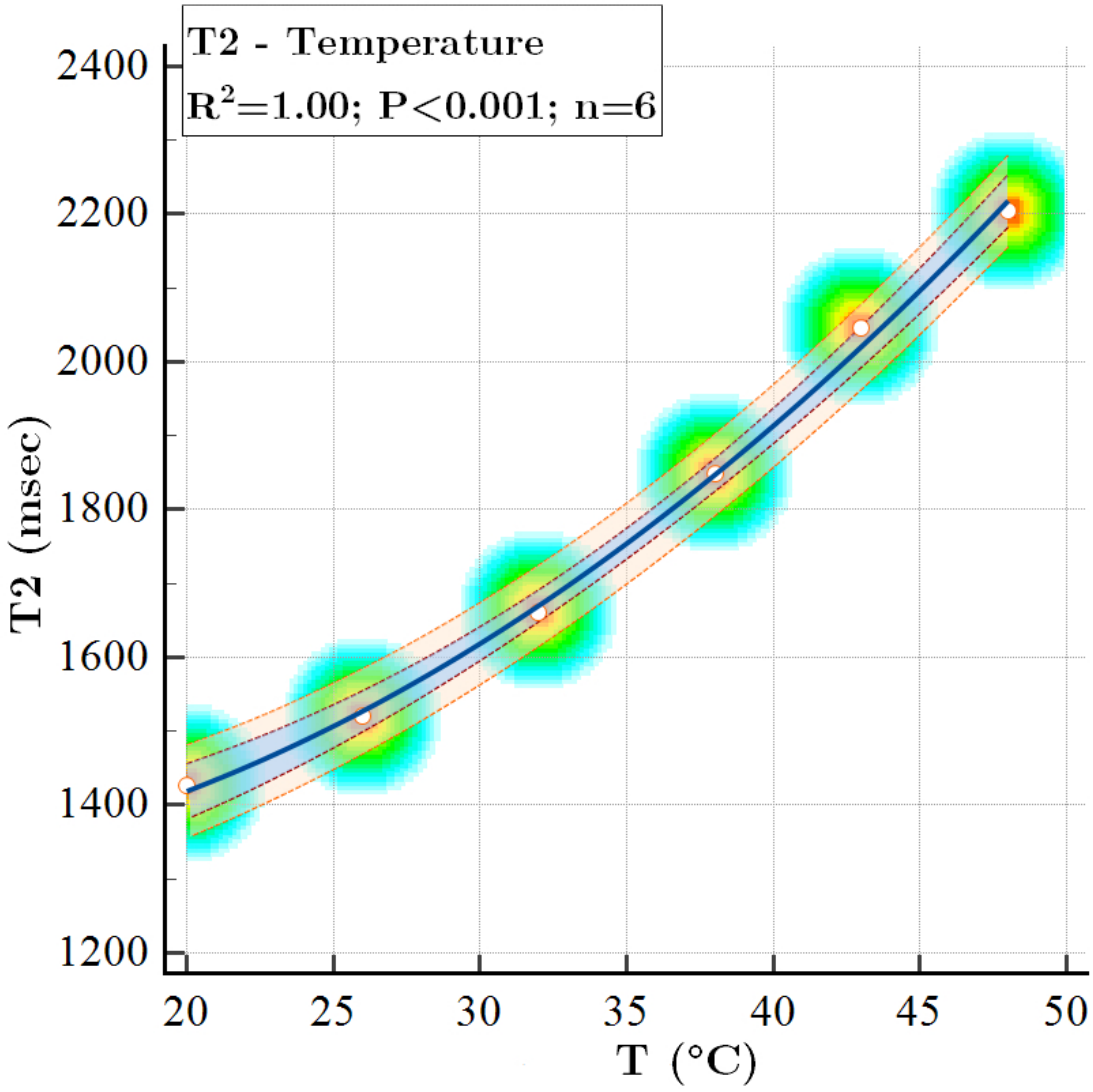

Figure 5.5.7: Polynomial regression for the relationship between melanoma's $T2$ and T. The $T2$ values were obtained with HASTE sequence. The dashed brown curves represent the 95% confidence interval for the regression line. The dashed orange curves represent the 95% prediction interval for the regression curve.

$$T2(T) = (0.48 \pm 0.09) \cdot T^2 - (3.74 \pm 6.55) \cdot T + (1304.12 \pm 105.34) \quad (5.5.1)$$

Melanoma Electrical Conductivity "C" versus Temperature "T" plot:

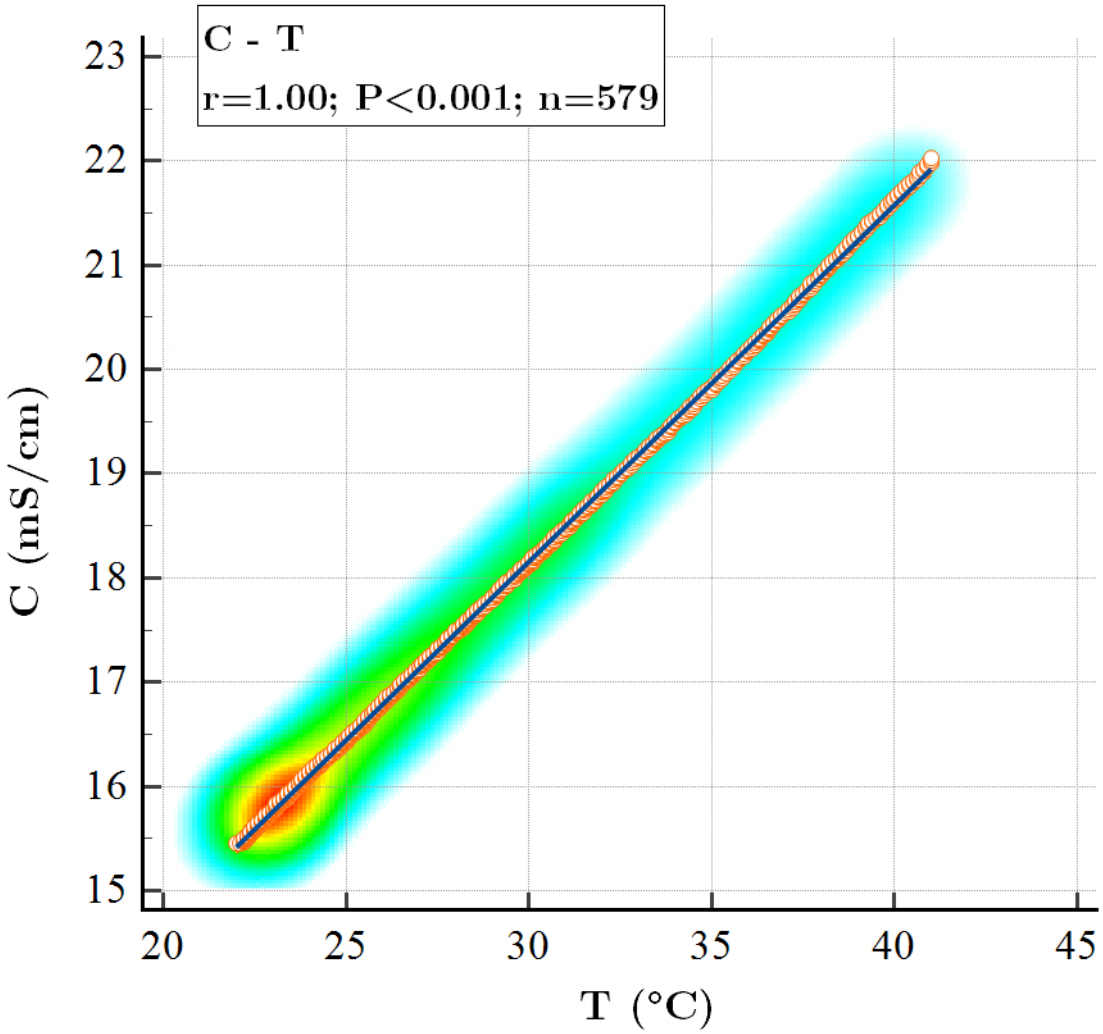

Figure 5.5.8: Linear fit for $C - T$ plot of melanoma cells.

$$C(T) = (0.3424 \pm 0.0001) \cdot T + (7.886 \pm 0.006) \tag{5.5.2}$$

6. Discussion/Conclusion

The purpose of this work was to determine the feasibility of measuring temperature non-invasively with magnetic resonance imaging during hyperthermia process.

From the colored maps we observed for each solution regardless of $NaCl$ content, that as the temperature increases the $T2$ parameter increases as well, which is also observed by the increase of the color in the scale of red in the respective maps.

6.1 T2 Parameter as Temperature Measurement Tool

From the $T2$ parameter versus Temperature (T) plots, r index had value 1, $r = 1$, throughout every analysis. This suggests that the relaxation time $T2$ can be a great indicator which can sensitively measure temperature changes during hyperthermia process. In more detail, for solution which resembled Fat, the plot of $T2$ versus T gives $r = 1$, $P < 0.001$ for six measurements $n = 6$. For the solution resembled Grey Matter, index r was equal to 1, $r = 1$, with $P < 0.001$ for six measurements as well, $n = 6$. Finally, index r for CsF had also value $r = 1$, with $P < 0.001$ and $n = 6$, in the temperature range from $20°C$ to $45°C$.

In short:

$T2 - T$ Plots			
Solution resembling	r	$P <$	n
Fat	1	0.001	6
Grey Matter	1	0.001	6
CsF	1	0.001	6

Positive r values suggest a positive correlation, in which both variables' values tend to rise in perfect sync. The number 1, $r = 1$, denotes a "perfect" positive correlation. At a constant rate, two completely correlated variables change together. As a result, they tend to have a linear relationship. All data points in a scatterplot can be linked together by a straight line.

The $p-$value is the probability of observing a non-zero correlation coefficient in our sample data when in fact the null hypothesis is true. A low $p-$value would lead you to reject the null hypothesis. A typical threshold for rejection of the null hypothesis is a $p-$value of 0.05. That is, if you have a $p-$value less than 0.05, you would reject the null hypothesis in favor of the alternative hypothesis—that the correlation coefficient is different from zero.

When the null hypothesis is true, the $p-$value is the likelihood of seeing a non-zero correlation coefficient in sample data. The null hypothesis would be rejected if the $p-$value was low. A 0.05 $p-$value is a common threshold for rejecting the null hypothesis. If the $p-$value is less than 0.05, the null hypothesis is rejected in favor of the alternative hypothesis, which states that the correlation coefficient is not zero.

6.2 Differences in Electrical Conductivity (EC) "C" between Induction and Diathermy Heating Tools

We also observed different values in slopes of the linear adjustment of the electrical conductivity plots as a function of temperature, depending on the Sodium Chloride ($NaCl$) content of each solution, in a temperature range between $20°C - 45°C$.

More specifically, the solution that resembles CsF, which had the highest concentration of Sodium Chloride, $NaCl$, ($c = 778.3gm/mL$), heated faster. It was also the solution with the highest electrical conductivity in the temperature range of hyperthermia process. Indicatively, the electrical conductivity (C) of the solution at $37°C$ had a value of $18.06mS/cm$ which was measured after the heating process through the microwave diathermy machine, while the value of the electrical conductivity at $37°C$, with the solution being inductively heated by the stirring machine, was $17.92mS/cm$.

$$\frac{|C_{th} - C_{exp}|}{C_{th}} = \frac{|17.92 - 18.06|}{17.92} \cdot 100\% = 0.78\%$$

where C_{th} is the reference value of electrical conductivity (EC) for CsF,

i.e. Cerebrospinal Fluid, according to the aforementioned conductivity values from bibliography (see S.4.1).

Solution that resembles Grey Matter was the solution with the second highest concentration in $NaCl$ ($c = 167.6gm/mL$). It heated at a slower rate than the Cerebrospinal Fluid-like solution, but faster than the Fat-like solution. The indicative value of electrical conductivity C during induction heating through the stirrer was $4.04mS/cm$ at $37°C$ while with the microwave diathermy machine, it was $4.24mS/cm$, at $37°C$ as well.

$$\frac{|C_{th} - C_{exp}|}{C_{th}} = \frac{|4.04 - 4.24|}{4.04} \cdot 100\% = 4.95\%$$

where C_{th} is the reference value of electrical conductivity (EC) for Grey Matter, according to the aforementioned conductivity values from bibliography (see S.4.1).

The solution that resembles Fat, which had the lowest concentration in $NaCl$ ($c = 16.0gm/mL$) was heated at a slower rate compared to the other solutions. At temperatures of $37°C$ and heated by the microwave diathermy machine, its electrical conductivity C was $0.438mS/cm$ while with inductive heating using stirrer, the value of electrical conductivity C at $37°C$ was $0.44mS/cm$.

$$\frac{|C_{th} - C_{exp}|}{C_{th}} = \frac{|0.440 - 0.438|}{0.440} \cdot 100\% = 0.45\%$$

where C_{th} is the reference value of electrical conductivity (EC) for Fat, according to the aforementioned conductivity values from bibliography (see S.4.1).

In brief:

$T \pm \delta T = (37.0 \pm 0.1)[°C]$			
Solution resembling	$c[mg/mL]$	$C_{th}[mS/cm]$	$C_{exp}[mS/cm]$
Fat	16.0 ± 0.1	0.440 ± 0.001	0.438 ± 0.001
Grey Matter	167.6 ± 0.1	4.04 ± 0.01	4.24 ± 0.01
CsF	778.3 ± 0.1	17.92 ± 0.01	18.06 ± 0.01

6.3 Slopes comparison among $C-T$ and $T2-T$ Plots

Results indicated a measurement overlap, which could be quantified by comparing the slopes. Slopes in plots "$T2$" parameter versus Temperature "T" ($T2-T$) and Electrical Conductivity (EC) "C" versus Temperature "T" ($C-T$) become steeper as the concentration of Sodium Chloride $NaCl$ increases. I.e. as the Sodium Chloride $NaCl$ content of the solutions increases, so do the slopes of the $C-T$ and $T2-T$ plots, respectively.

We observe that the Fat-simulating solution has the smallest slope value in both the $C-T$ and $T2-T$ diagrams. Given the decreased Sodium Chloride ($NaCl$) content level, this stands to reason.

$$T2(T) = (19.35 \pm 0.89) \cdot T + (1584 \pm 35)$$
$$C(T) = (0.007310 \pm 0.000004) \cdot T + (0.16761 \pm 0.00011)$$

For the solution that resembles Grey Matter:

$$T2(T) = (37.78 \pm 1.50) \cdot T + (1292 \pm 48)$$
$$C(T) = (0.07152 \pm 0.00004) \cdot T + (1.5896 \pm 0.0014)$$

For the Cerebrospinal Fluid-simulating solution:

$$T2(T) = (38.35 \pm 0.90) \cdot T + (1369 \pm 32)$$
$$C(T) = (0.2981 \pm 0.0001) \cdot T + (7.053 \pm 0.006)$$

In short:

Solution resembling	$T2-T$ slope $[ms/^\circ C]$	$C-T$ slope $[mS/^\circ C]$
Fat	19.35 ± 0.89	0.007310 ± 0.000004
Grey Matter	37.78 ± 1.50	0.07152 ± 0.00004
CsF	38.35 ± 0.90	0.2981 ± 0.0001

6.4 Melanoma Cells

As for melanoma cells, this solution contains cells and there are discrepancies between this cultivation and solutions containing Sodium Chloride ($NaCl$). For this reason, it is not possible to compare the measurements to those of the aforementioned solutions. It could, however, be a future study comparing Electrical Conductivity (EC), T2 parameter, and time (t) values between real tissue samples.

References

[1] F. Bloch, 'Nuclear induction', *Physical review*, vol. 70, no. 7-8, pp. 460–474, 1946.

[2] E. M. Purcell, H. C. Torrey and R. V. Pound, 'Resonance absorption by nuclear magnetic moments in a solid', *Physical review*, vol. 69, no. 1-2, p. 37, 1946.

[3] F. Bloch, 'Nuclear induction', *Physical review*, vol. 70, no. 7-8, pp. 127–129, 1946.

[4] R. Damadian, 'Tumor detection by nuclear magnetic resonance', *Science*, vol. 171, no. 3976, pp. 1151–1153, 1971.

[5] E. J. Blink, 'Mri: Physics', *Online PDF file*, pp. 0–75, 2004.

[6] D. W. McRobbie, E. A. Moore, M. J. Graves and M. R. Prince, *Mri from protons to pictures*, 2006.

[7] R. Walcarius, 'Cardiovascular magnetic resonance imaging', *Journal of Medical Imaging and Radiation Sciences*, vol. 39, no. 4, p. 216, 2008.

[8] D. Weishaupt, V. D. Köchli and B. Marincek, *How does MRI work?: an introduction to the physics and function of magnetic resonance imaging*. Springer Science & Business Media, 2008.

[9] J. Duerk, 'Relaxation and contrast in mr imaging', *Riederer SJ, Wood ML*, 1997.

[10] M. Nessaiver, *All you really need to know about mr imaging physics*, 1996.

[11] P. S. Tofts, 'Qa: Quality assurance, accuracy, precision and phantoms', in *Quantitative MRI of the brain: measuring changes caused by disease*, John Wiley & Sons Chichester, UK, 2003, pp. 144–162.

[12] M. Brown and R. Semelka, 'Pulse sequences', *MRI Basic Principles and Applications, ed*, vol. 3, pp. 67–91, 2003.

[13] A. L. Horowitz, *MRI physics for physicians*. Springer Science & Business Media, 2012.

[14] H. H. Schild, *MRI made easy (... well almost)*. Berlex Laboratories, 1992.

[15] B. A. Jung and M. Weigel, 'Spin echo magnetic resonance imaging', *Journal of Magnetic Resonance Imaging*, vol. 37, no. 4, pp. 805–817, 2013.

[16] B. M. Dale, M. A. Brown and R. C. Semelka, *MRI: basic principles and applications*. John Wiley & Sons, 2015.

[17] M. Markl and J. Leupold, 'Gradient echo imaging', *Journal of Magnetic Resonance Imaging*, vol. 35, no. 6, pp. 1274–1289, 2012.

[18] E.-W. Radue, M. Weigel, R. Wiest and H. Urbach, 'Introduction to magnetic resonance imaging for neurologists', *Continuum: Lifelong Learning in Neurology*, vol. 22, no. 5, pp. 1379–1398, 2016.

[19] T. Maris, 'Application and research in thalassemia', in *Development of software for the creation of calculated quantitative images (M.R.I) T2-MRI and their use in tissue characterization*, National and Kapodistrian University of Athens, GR, 1997.

[20] A. Elster, *Questions and answers in mri—compressed sensing*, 2018.

[21] M. L. Lipton, E. Kanal and M. Jacobs, 'Totally accessible mri: A user's guide to principles, technology, and applications', *Medical Physics*, vol. 35, no. 11, p. 5198, 2008.

[22] R. C. Semelka, N. L. Kelekis, D. Thomasson, M. A. Brown and G. A. Laub, 'Haste mr imaging: Description of technique and preliminary results in the abdomen', *Journal of Magnetic Resonance Imaging*, vol. 6, no. 4, pp. 698–699, 1996.

[23] J. Tang, 'Unlocking potentials of microwaves for food safety and quality', *Journal of food science*, vol. 80, no. 8, E1776–E1793, 2015.

[24] A. Gartshore, M. Kidd and L. T. Joshi, 'Applications of microwave energy in medicine', *Biosensors*, vol. 11, no. 4, p. 96, 2021.

[25] A. Rosen, M. A. Stuchly and A. Vander Vorst, 'Applications of rf/microwaves in medicine', *IEEE transactions on microwave theory and techniques*, vol. 50, no. 3, pp. 963–974, 2002.

[26] J. Lantis II, K. Carr, R. Grabowy, R. Connolly and S. Schwaitzberg, 'Microwave applications in clinical medicine', *Surgical endoscopy*, vol. 12, no. 2, pp. 170–176, 1998.

[27] K. H. Yeap and K. Hirasawa, 'Introductory chapter: Electromagnetism', *Electromagnetic fields and waves*, vol. 356, 2019.

[28] Z. Li, 'Physics essay: The nature of charge, principle of charge interaction and coulomb's law', *Applied Physics Research*, vol. 7, no. 6, p. 52, 2015.

[29] Y. Watanabe and S. Nitta, 'A study on characteristics of electromagnetic waves propagating through the space between overlapped metal plates', *IEEE Transactions on Electromagnetic Compatibility*, vol. 58, no. 1, pp. 54–65, 2015.

[30] M. Pieraccini, A. Bicci, D. Mecatti, G. Macaluso and C. Atzeni, 'Propagation of large bandwidth microwave signals in water', *IEEE transactions on antennas and propagation*, vol. 57, no. 11, pp. 3612–3618, 2009.

[31] Y. S. Kivshar, 'Control of electromagnetic waves in metamaterials: From microwaves to optics', in *2013 International Kharkov Symposium on Physics and Engineering of Microwaves, Millimeter and Submillimeter Waves*, IEEE, 2013, pp. 30–30.

[32] Z.-c. Tu, Y.-m. Hu, H. Wang, X.-q. Huang, S.-q. Xia and P.-p. Niu, 'Microwave heating enhances antioxidant and emulsifying activities of ovalbumin glycated with glucose in solid-state', *Journal of food science and technology*, vol. 52, no. 3, pp. 1453–1461, 2015.

[33] W. D. Kimura, 'What are electromagnetic waves', *Electromagnetic Waves and Lasers; Morgan & Claypool Publishers: San Rafael, CA, USA*, 2017.

[34] E. Grant, B. J. Halstead *et al.*, 'Dielectric parameters relevant to microwave dielectric heating', *Chemical society reviews*, vol. 27, no. 3, pp. 213–224, 1998.

[35] C. Timmel and P. Hore, 'Oscillating magnetic field effects on the yields of radical pair reactions', *Chemical Physics Letters*, vol. 257, no. 3-4, pp. 401–408, 1996.

[36] H. Hollmann, 'Das problem der behandlung biologischer körper im ultrakurzwellen-strahlungsfeld', *Ultrakurzwellen in ihren medizinisch-biologischen Anwendungen. Theim, Leipzig*, pp. 232–249, 1938.

[37] A. Hemingway and K. Stenstrom, 'Physical characteristics of short wave diathermy', *Journal of the American Medical Association*, vol. 111, no. 25, pp. 2298–2302, 1938.

[38] J. C. Lin, G. Kantor and A. Ghods, 'A class of new microwave therapeutic applicators', *Radio science*, vol. 17, no. 5S, 119S–123S, 1982.

[39] J. C. Lin and S. M. Michaelson, *Biological effects and health implications of radiofrequency radiation*. Springer Science & Business Media, 2013.

[40] A. Chicheł, J. Skowronek, M. Kubaszewska and M. Kanikowski, 'Hyperthermia–description of a method and a review of clinical applications', *Reports of Practical Oncology & Radiotherapy*, vol. 12, no. 5, pp. 267–275, 2007.

[41] C. P. Hancock, P. Burn, C. Duff *et al.*, 'A new wave in electrosurgery: A review of existing and introduction to new radio-frequency and microwave therapeutic systems', *IEEE Microwave Magazine*, vol. 16, no. 2, pp. 14–30, 2015.

[42] W. Bush, 'Uber den finfluss wetchen heftigere eryspelen zuweilen auf organlsierte neubildungen dusuben', *Verh Natruch Preuss Rhein Westphal*, vol. 23, pp. 28–30, 1886.

[43] F. Westermark, 'Uber die behandlung des ulcerirenden cervix carcinoma mittels knonstanter warme', *Zentralblatt für Gynäkologie*, vol. 22, pp. 1335–7, 1898.

[44] A. Westra and W. Dewey, 'Variation in sensitivity to heat shock during the cell-cycle of chinese hamster cells in vitro', *International Journal of Radiation Biology and Related Studies in Physics, Chemistry and Medicine*, vol. 19, no. 5, pp. 467–477, 1971.

[45] J. Overgaard and P. Bichel, 'The influence of hypoxia and acidity on the hyperthermic response of malignant cells in vitro', *Radiology*, vol. 123, no. 2, pp. 511–514, 1977.

[46] G. Crile Jr, 'Selective destruction of cancers after exposure to heat', *Annals of surgery*, vol. 156, no. 3, p. 404, 1962.

[47] E. Ben-Hur, M. Elkind and B. Bronk, 'Thermally enhanced radioresponse of cultured chinese hamster cells: Inhibition of repair of sublethal damage and enhancement of lethal damage', *Radiation research*, vol. 58, no. 1, pp. 38–51, 1974.

[48] P. E. Brown, 'Future special issues', *IEEE spectrum*, p. 71, 1978.

[49] E. Atkinson, 'Hyperthermia techniques and instrumentation', *Hyperthermia in Cancer Therapy, ed. FK Storm*, pp. 233–255, 1983.

[50] J. Dickson, 'Thermosensitivity of neoplastic tissues in vivo', *Hyperthermia in cancertherapy*, pp. 63–140, 1983.

[51] A. Guy, 'Physical aspects of localized heating by radio-waves and microwaves', *Hyperthermia in cancer therapy*, pp. 279–304, 1983.

[52] J. Hand, 'Hyperthermia: Challenging applications of physics in cancer therapy', *Physics Bulletin*, vol. 38, no. 3, p. 111, 1987.

[53] H. P. Schwan, 'Electrical properties of tissue and cell suspensions', in *Advances in biological and medical physics*, vol. 5, Elsevier, 1957, pp. 147–209.

[54] H. P. Schwan and K. R. Foster, 'Rf-field interactions with biological systems: Electrical properties and biophysical mechanisms', *Proceedings of the IEEE*, vol. 68, no. 1, pp. 104–113, 1980.

[55] R. Pethig, 'Dielectric properties of biological materials: Biophysical and medical applications', *IEEE transactions on electrical insulation*, no. 5, pp. 453–474, 1984.

[56] R. Pethig and D. B. Kell, 'The passive electrical properties of biological systems: Their significance in physiology, biophysics and biotechnology', *Physics in Medicine & Biology*, vol. 32, no. 8, p. 933, 1987.

[57] K. R. Foster, H. P. Schwan *et al.*, 'Dielectric properties of tissues', *CRC handbook of biological effects of electromagnetic fields*, pp. 27–96, 1986.

[58] M. Stuchly and S. Stuchly, 'Dielectric properties of biological substances—tabulated', *Journal of Microwave power*, vol. 15, no. 1, pp. 19–25, 1980.

[59] L. A. Geddes and L. E. Baker, 'The specific resistance of biological material—a compendium of data for the biomedical engineer and physiologist', *Medical and biological engineering*, vol. 5, no. 3, pp. 271–293, 1967.

[60] F. Duck, 'Physical properties of tissue: A comprehensive reference book (london/san diego: Academic)', 1990.

[61] S. F. Adam, *Microwave Theory and Applications: 21 Laboratory Experiments*. Prentice-Hall, 1969.

[62] O. P. Gandhi, *Microwave engineering and applications*. Pergamon, 1981.

[63] J. Kraus and K. Carver, *Electromagnetics. 464-467*, 1973.

[64] E. Jordan and K. Balmain, 'Electromagnetic waves and radiating systems, prentice hall', *Englewood Cliffs, New Jersey*, 1968.

[65] R. E. Collin, *Foundations for microwave engineering*. John Wiley & Sons, 2007.

[66] ——, *Antenna theory*, 1. McGraw-Hill, 1969.

[67] W. Ramo, 'Van duzer', *Fields and waves in communication electronics*, vol. 2, 1965.

[68] A. F. Harvey, *Microwave engineering*. Academic Press, 1963.

[69] J. C. Maxwell, *A Treatise on Electricity and Magnetism: pt. III. Magnetism. pt. IV. Electromagnetism*. Clarendon press, 1881, vol. 2.

[70] S. JA, 'Electromagnetic theory', *Mi: Grew Hill, New York*, 1941.

[71] P. Lorrain and D. Corson, 'Electromagnetic fields and waves wh freeman and co', *San Francisco*, vol. 150, 1970.

[72] R. Jayasundar, L. D. Hall and N. M. Bleehen, 'Magnetic resonance, hyperthermia and oncology', *Current Science*, pp. 794–799, 1999.

[73] E. Grant, 'Biological effects of radiowaves and microwaves', *Phys. Technol.;(United Kingdom)*, vol. 11, 1980.

[74] J. Thuery, 'Microwaves: Industrial, scientific and medical applications, artech house', *Inc. Norwood, Massachussets*, pp. 188–203, 1992.

[75] S. O. Nelson, 'Dielectric properties of agricultural products-measurements and applications', *IEEE transactions on Electrical Insulation*, vol. 26, no. 5, pp. 845–869, 1991.

[76] A. Metaxas and R. Meredith, 'industrial microwave heating", peter peregrinus ltd (iee)', *London,(UK)*, 1983.

[77] R. Höber, 'Eine methode, die elektrische leitfähigkeit im innern von zellen zu messen', *Pflüger's Archiv für die gesamte Physiologie des Menschen und der Tiere*, vol. 133, no. 4, pp. 237–253, 1910.

[78] H. Fricke and H. J. Curtis, 'The electric impedance of hemolyzed suspensions of mammalian erythrocytes', *The Journal of general physiology*, vol. 18, no. 6, pp. 821–836, 1935.

[79] P. Debye, 'Polar molecules, the chemical catalog company', *Inc., New York*, pp. 77–108, 1929.

[80] C. P. Smyth *et al.*, 'Dielectric behavior and structure', 1955.

[81] A. Von Hippel, '1954dielectric materials and applications', *Artech House*,

[82] W. D. Hurt, 'Multiterm debye dispersion relations for permittivity of muscle', *IEEE Transactions on Biomedical Engineering*, no. 1, pp. 60–64, 1985.

[83] G. Melia, 'Electromagnetic absorption by the human body from 1-15 ghz', Ph.D. dissertation, University of York, 2013.

[84] X. Li, *Body matched antennas for microwave medical applications*. KIT Scientific Publishing, 2014, vol. 72.

[85] Y. Feldman, A. Puzenko and Y. Ryabov, 'Dielectic relaxation phenomena in complex materials', *Advances in chemical physics*, vol. 133, no. A, p. 1, 2006.

[86] P. Altman and D. Dittmer, 'Biology data book. amrl-tr-64-100', *AMRL-TR. Aerospace Medical Research Laboratories (US)*, pp. 1–631, 1964.

[87] J. L. Schepps and K. R. Foster, 'The uhf and microwave dielectric properties of normal and tumour tissues: Variation in dielectric properties with tissue water content', *Physics in Medicine & Biology*, vol. 25, no. 6, p. 1149, 1980.

[88] A. C. GUYTON and G. G. ARMSTRONG, *A Laboratory Manual for Guyton's Function of the Human Body.[By] George G. Armstrong.*. WB Saunders Company, 1969.

[89] D. Eisenberg and W. Kauzmann, *The structure and properties of water*. OUP Oxford, 2005.

[90] F. FranksWater, *A comprehensive treatise, vol. 1*, 1972.

[91] J. B. Hasted *et al.*, *Aqueous dielectrics*. Chapman and Hall London, 1973, vol. 122.

[92] J. Hasted and S. El Sabeh, 'The dielectric properties of water in solutions', *Transactions of the Faraday Society*, vol. 49, pp. 1003–1011, 1953.

[93] C. R. P. Bureau, I. M. P. Institute and M. Stuchly, *Microwave Bioeffects and Radiation Safety: Short Course Transactions, Ottawa, Ontario, June 26, 1978*. International Microwave Power Institute, 1978.

[94] H. Cook, 'The dielectric behaviour of some types of human tissues at microwave frequencies', *British Journal of Applied Physics*, vol. 2, no. 10, p. 295, 1951.

[95] H. P. Schwan, 'Survey of microwave absorption characteristics of body tissues', *Techn. Rep*, vol. 25, 1958.

[96] *HI-2030 edge Hybrid Multiparameter EC Meter*, hannainstruments.co.uk/edge-bench-conductivity-meter.html.

[97] *Digital EC/Temperature Electrode - HI763100*, hannainst.com/hi763100-digital-ec-temperature-electrode.html.

[98] *HI7030/1G 12888μS/cm Conductivity Standard*, hannainst.com/hi7030-1g.html.

[99] *ARS 220-4N - KERN SOHN GmbH*, kern-sohn.com/cgi-bin/cosmoshop/.

[100] *ARE Hot Plate Stirrer*, velp.com/en-ww/are-aluminum-hot-plate-stirrer.aspx.

[101] *Siemens Magnetom Sonata 1.5T*, amberusa.com/equipment/mri/1-5t/siemens-magnetom-sonata.

[102] *m3300 Biomedical Lab Kit Fluoroptic thermometer*, asras.com/images/sub-1369197268/M3300-lab-kit.pdf.

[103] *Artisan. Find the Lumasense Technologies*, artisantg.com/info/Lumasense-Technologies-Luxtron-FOT-Manual-2015111885135.pdf.

[104] *FISIOWAVE, fisioline*, fisioline.com/medical/fisiowave.

[105] G. W. Crile, H. R. Hosmer and A. F. Rowland, 'The electrical conductivity of animal tissues under normal and pathological conditions', *American Journal of Physiology-Legacy Content*, vol. 60, no. 1, pp. 59–106, 1922.

[106] S. Radvan-Ziemnowicz, J. McWilliams and W. Kucharski, *Conductivity versus frequency in human and feline cerebrospinal fluid*. 1964, vol. 6, p. 108.

[107] S. B. Baumann, D. R. Wozny, S. K. Kelly and F. M. Meno, 'The electrical conductivity of human cerebrospinal fluid at body temperature', *IEEE transactions on biomedical engineering*, vol. 44, no. 3, pp. 220–223, 1997.

[108] W. Freygang Jr and W. M. Landau, 'Some relations between resistivity and electrical activity in the cerebral cortex of the cat', *Journal of Cellular and Comparative Physiology*, vol. 45, no. 3, pp. 377–392, 1955.

[109] J. B. Ranck Jr, 'Specific impedance of rabbit cerebral cortex', *Experimental neurology*, vol. 7, no. 2, pp. 144–152, 1963.

[110] A. v. Harreveld, T. Murphy and K. Nobel, 'Specific impedance of rabbit's cortical tissue', *American Journal of Physiology-Legacy Content*, vol. 205, no. 1, pp. 203–207, 1963.

[111] P. N. Robillard and Y. Poussart, 'Specific-impedance measurements of brain tissues', *Medical and Biological Engineering and Computing*, vol. 15, no. 4, pp. 438–445, 1977.

[112] N. K. Logothetis, C. Kayser and A. Oeltermann, 'In vivo measurement of cortical impedance spectrum in monkeys: Implications for signal propagation', *Neuron*, vol. 55, no. 5, pp. 809–823, 2007.

[113] H. P. Schwan and C. F. Kay, 'Specific resistance of body tissues', *Circulation Research*, vol. 4, no. 6, pp. 664–670, 1956.

[114] S. Rush, J. Abildskov and R. McFee, 'Resistivity of body tissues at low frequencies', *Circulation research*, vol. 12, no. 1, pp. 40–50, 1963.

[115] S. R. Smith and K. R. Foster, 'Dielectric properties of low-water-content tissues', *Physics in Medicine & Biology*, vol. 30, no. 9, p. 965, 1985.

[116] L. A. Geddes, L. E. Baker, L. Baker and L. E. Baker, *Principles of applied biomedical instrumentation*. Wiley-Interscience, 1989.

[117] B. Rigaud, L. Hamzaoui, N. Chauveau, M. Granie, J.-P. S. Di Rinaldi and J.-P. Morucci, 'Tissue characterization by impedance: A multifrequency approach', *Physiological Measurement*, vol. 15, no. 2A, A13, 1994.

[118] C. Gabriel, S. Gabriel and y. E. Corthout, 'The dielectric properties of biological tissues: I. literature survey', *Physics in medicine & biology*, vol. 41, no. 11, p. 2231, 1996.

[119] *Melpomeni Tseliou, Post Doctoral Researcher Laboratory of Clinical Virology, Medical School, University of Crete*, melina_mbg@windowslive.com.

[120] *MedCalc Statistical software*, medcalc.org.

[121] *Origin Pro from OriginLab*, originlab.com.